Alma Mater Studiorum - Università di Bologna

School of Engineering
Department of Electrical, Electronic
and Information Engineering "Guglielmo Marconi" - DEI

Master's Degree in
Telecommunications engineering

Thesis in
Antennas for Wireless Systems M

Design of a compact monopole-based large Dynamic Scattering Array at 28 GHz for future 6G networks

Candidate:
Michele Cocchi

Relator:
Prof. **Diego Masotti**

Co-relators:
Prof.ssa **Alessandra Costanzo**
Dr. **Simone Trovarello**

Academic Year 2024/2025
Session V

Abstract

This thesis focuses on the practical implementation of a 127 element Dynamic Scattering Array operating at 28 GHz, for 6G applications. Starting from an ideal reference model, the work presents the main limitations of creating a physically realizable structure.

A first design considers planar monopoles, showing that the planar layout is strongly affected by ground plane radiation and become difficult to scale. To solve this, a final architecture based on hexahedral monopoles embedded in a dielectric overlay above a circular ground plane is proposed, providing improved azimuthal omnidirectionality and a compact implementation with monopoles realized as via-holes in the dielectric.

The array is modeled as a multiport system, and tunable reactive loads are introduced to enable pattern reconfiguration. A varactor based reactive load is then designed to achieve a reactance range compatible with beam synthesis. Finally, the beamforming capability of the array is validated, confirming the feasibility of Dynamic Scattering Array working at 28 GHz.

Contents

List of Figures

Acronyms

AiP Antenna in Package. 15

CMT Characteristic Modes Theory. 26

DE-ESPAR Dielectric Embedded ESPAR. 3, 21, 22

DoA Direction of Arrival. 18

DRA Dielectric Resonator Antenna. 3, 17, 18

DSA Dynamic ascattering Array. 1, 3, 24, 26, 32, 34, 35, 37, 120, 122

ESPAR Electronically Stearable Parasitic Array Radiator. 1, 3, 12–15, 17–21, 23–28, 33, 35

FDTD Finite Difference Time Domain. 17

MEMS Micro Electro Mechanical Systems. 15

MuPAR Multiport Parasitic Array Radiator. 3, 19, 20

NMSE Normalized Mean Square Error. 14

PEC Perfect Electric Conductor. 41, 72, 77

RF Radio Frequency. 15, 18, 20, 24

SIM Stacked Intelligent Metasurface. 24

SINR Signal to Interference plus Noise Ratio. 14

SIW Substrate Integrated Waveguide. 20

SPSA Simultaneous Perturbation Stochastic Approximation. 14

SRR Split Ring Resonator. 3, 15, 17

WSN Wireless Sensor Network. 18

Introduction

The transition toward sixth generation (6G) wireless networks is characterized by an increasing demand for higher data rates, ultra low latency, and constant connectivity in a more and more crowded spectrum. To meet these requirements, the exploitation of the millimeter-wave spectrum and new studies on wireless transmission at THz band has become a research priority. However, operating at such high frequencies introduces significant challenges such as: increasing Path Loss and atmospheric attenuation, and so new models are needed to characterize these phenomena [15]. Moreover, to tackle increasingly harsh scenarios and the need for high data rates, the development of advanced MIMO beamforming techniques is necessary to ensure reliable communication links through high-gain directional radiation patterns [16].

In this scenario, traditional phased array architectures often face limitations in terms of hardware complexity, high power consumption, and heat dissipation due to the massive number of active RF chains required [17].

This thesis addresses these challenges by investigating a physically achievable Dynamic Scattering Array (from now on DSA) based on monopole elements. The proposed design is a large array of 127 monopoles: by tuning reactive loads attached to parasitic elements and selecting one or more actives, the beam is steered with high precision. Thanks to the possibility of increasing the number of active elements, this approach offers a highly efficient and agile solution, which can be integrated into base stations for future 6G infrastructures.

The thesis is structured as follows:

- **Chapter 1**: State of the Art on existing solutions.
- **Chapter 2**: Theoretical Framework.
- **Chapter 3**: Planar layout and related issues.
- **Chapter 4**: Final layout and related results.

Chapter 1

State of the art

The state of the art is first reviewed by focusing on ESPAR and related techniques, which have predominantly been investigated at sub 6 GHz (or, more generally, comparatively to this work, low-frequency) regimes. The chapter ends introducing the Dynamic Scattering Array paradigm, whose key objective is the implementation of many scatterers and a flexible architecture where the set of actively driven elements can be dynamically selected and reconfigured.

1.1 First development of ESPAR antennas

The first two ESPARs done explore two main directions: a general theoretical formulation of reactively controlled arrays and an early hardware implementation for mobile terminals. Harrington [1] models the antenna as an N-port radiating network in which only one, or a subsets, of ports is active, while the remaining ones are terminated on purely reactive loads: the farfield radiation pattern can be simply achieved by selecting proper reactive loads, enabling beam steering without the use of expansive phase shifters (more theoretical details will be presented in Chapter 2). For the numerical demonstrations, circular array with one central fed element and a ring of six parasitics (half-wave dipoles) is considered, where the parasitic elements are terminated with lumped reactances X_i while only the central element is excited by a voltage source, so that all outer currents are induced through mutual coupling. The dipoles have length $L = \lambda/2$ and diameter $D = L/100$, the inter element spacing S is a key design parameter and evaluated for values such as: $S = \lambda/2$, $S = \lambda/4$ or $S = \lambda/8$. The values of $S = \lambda/4$ is selected to be small enough to provide efficient electromagnetic coupling between elements, yet large enough to preclude extreme supergain behavior. Radiation optimization is performed numerically by iteratively tuning the load reactances, introducing an algorithm that sequentially maximizes gain. For the seven element circular configuration, directive patterns are synthesized for angles such as 0°, 10°, 20°, and 30°, with other directions obtained by symmetry rotations. Finally, this work provides the analytical basis for what later becomes known as ESPAR: the pattern synthesis through mutual coupling and reactive loading instead of usual phased excitation. The paper of Harrington is the first introducing this kind of array, proposing a general theory of ESPAR.

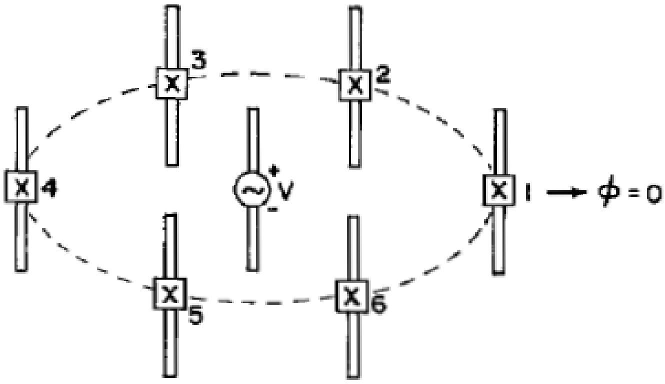

Figure 1.1: Array layout presented in [1]

Another work is presented by Milne [2], where one of the first ESPAR is realized in particular for mobile satellite communications. The structure consists of a quarter-wavelength active monopole over a ground plane of approximately 2.5λ diameter and surrounded by two concentric rings of parasitic monopoles (sixteen elements in total). Instead of continuously tunable reactances as proposed in this thesis work, each parasitic element is connected to ground through a switching device (e.g., PIN diode), so that it can be electrically enabled or disabled, in particular: When a diode is biased in the conducting state, the associated parasitic element is strongly excited by the incident field and re-radiates. With the diode in the non-conducting state, the associated parasitic element behaves as an isolated short dipole and is virtually transparent. This discrete loading produces beam steering in the azimuth plane with angular steps of approximately 22.5°. The antenna is tested at 1.5 GHz, showing impedance matching over 12% bandwidth.

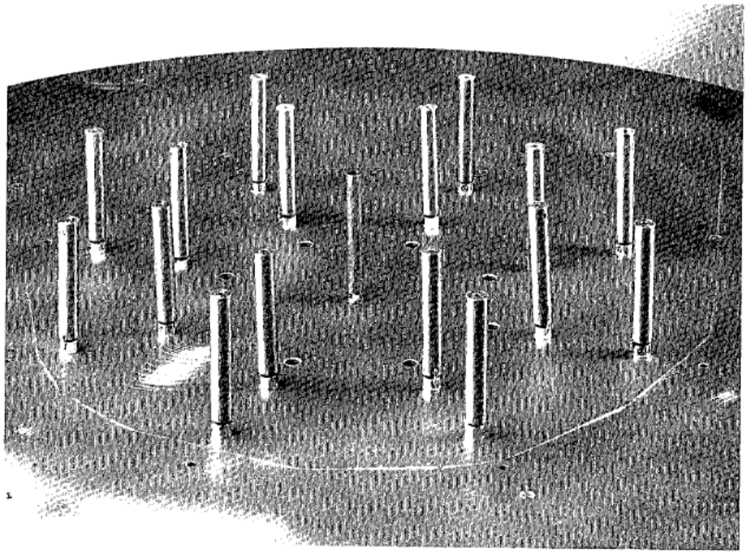

Figure 1.2: 16 elements ESPAR presented in [2]

1.2 Recent topologies and applications

The work of Sun *et al.* [3] introduces an algorithmic advancement over earlier ESPAR by introducing a faster adaptive beamforming algorithm (SPSA), instead of classical iterative adjustment of reactive loads. The antenna has one active central element (monopole) surrounded by six parasitic elements uniformly placed on a circular ground. The length of each monopole and the radius of the circular grid are one-quarter wavelength of the transmitting RF signal at 2.484 GHz. Instead of deterministic searches the beam synthesis is tractated as an optimization problem which maximizes the cross-correlation between a reference signal and the received one (similarly to set the NMSE between the received and desired signals as objective function of the optimizaion algorithm). The key aspect of this work lies in the SPSA algorithm which converges in about 50 iterations even in presence of severe interference conditions, achiveing a 10 dB output SINR. The paper presents an advancement on the algorithmic side, but the antenna layout is limited to a simple ESPAR configuration with just 6 scatterers. Moreover, the cited work does not highlight some practical issues as the finite ground plane effect, which instead is presented in this thesis.

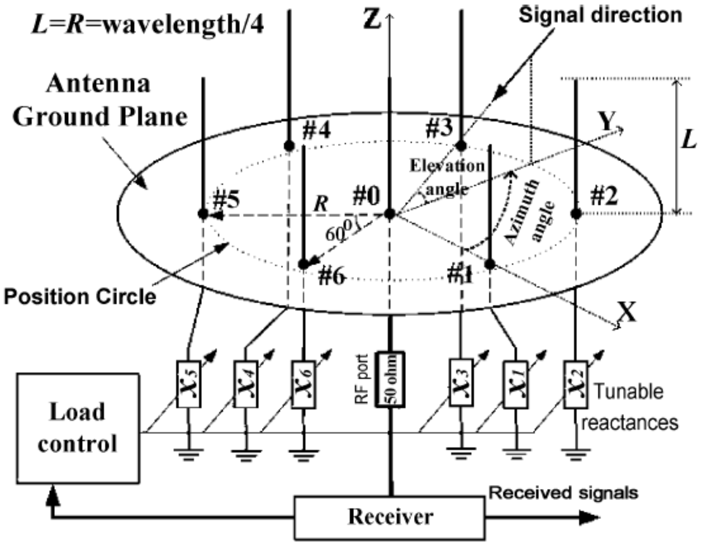

Figure 1.3: Configuration of the 7-elements ESPAR presented in [3]

In the paper of Shu *et al.* [4] an innovative way of obtaining beam-steering is presented: instead of classical varactors or RF MEMS, here the same process is obtained by exploiting the voltage-controlled anisotropic permittivity of a liquid cristal layer located under the paratic elements. The antenna is an AiP module composed of stacked Rogers 5880 substrates, a liquid-crystal cavity layer, DC bias lines, and flip-chip IC integration. The antenna works in the Ka-band at the same frequency of this thesis work: 28 GHz. Beam steering is achieved through voltage-controlled permittivity modulation, bringing to a continuous scan range of approximately $-27°$ to $+29°$ in the H-plane with a peak gain of 6 dBi in correspondence of 0° and a bandwidth of 8.3%. Although this approach demonstrates a compact layout and analog beam control at the same frequency of the thesis work, it introduces substantial fabrication and material complexity due to multilayer structure and LC injection cavities.

Another recent parasitic array is presented by Trinidade *et al.* [5]. In this paper one of the main intrinsic limitations of ESPAR antennas is presented: the uncontrolled near-field mutual coupling between passive elements. In standard ESPAR configurations, the currents induced on parasitic radiators are not independent becacuse each element interacts electromagetically with the near ones. This mutual coupling, if not controlled, perturbs the impendance matrix, bringing to a distorted radiation pattern. The antenna is a circular ESPAR with one central active monopole and six parasitic monopoles, but differently to other similar designs, each adjacent parasitic pair is separated by a metamaterial wall formed by SRRs. The resonant structures are oriented so that

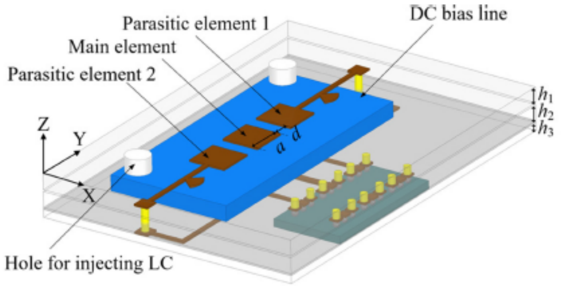

Figure 1.4: 3D view of the work presented in [4]

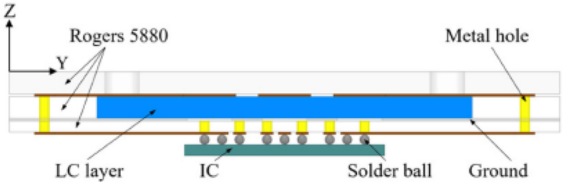

Figure 1.5: Lateral view of the work presented in [4]

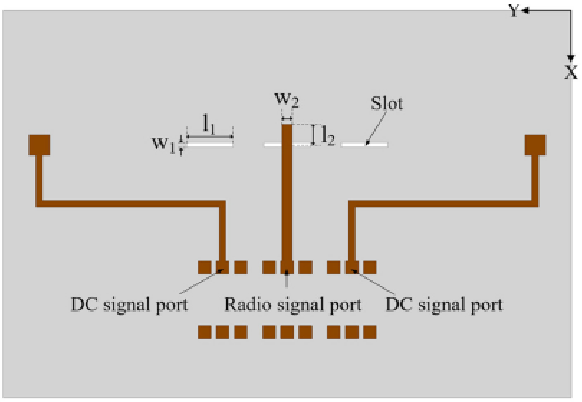

Figure 1.6: Back view of the work presented in [4]

they interact with the magnetic fields produced by neighboring parasitic monopoles. In particular: the magnetic field generated by passive elements pass through the centers of the concentric rings, which induces currents in the resonator structure. On the other hand, the magnetic field radiated by the central element (the driven one), does not interact with the resonators, and therefore it produces negligible induced currents in them. To characterize the structure, the authors extracted the full 7×7 impedance matrix through full-wave FDTD simulations and optimize geometrical parameters (ring spacing, inter element distance) via a genetic algorithm that minimizes a weighted cost function combining $|S_{ij}|$ and $|S_{ii}|$ terms. Results at approximately 1 GHz show strong reduction of coupling and restoration of impedance symmetry. The presented decoupling mechanism is innovative, but increases a lot the complexity of the array; in particular at higher frequencies where the reduced distance between the elements would not allow the insertion of resonant structures.

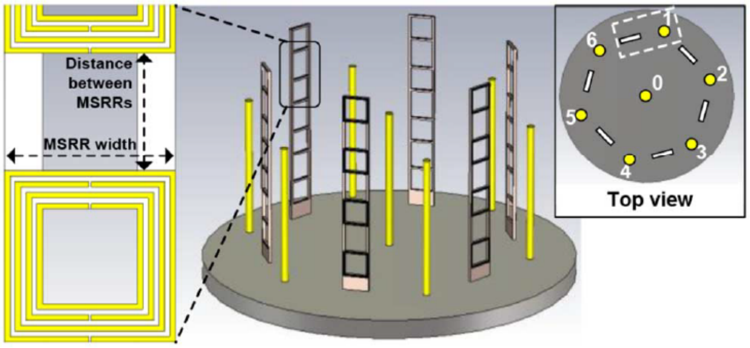

Figure 1.7: Structure of the ESPAR presented in [5] with focus on the SRR

A different structure is presented by Nikkhah *et al.* [6].In this design the main innovation is the use of DRA: instead of monopoles, the ESPAR is formed by rectangular DRA coupled with a narrow slot to the feeding line. The array is formed by one fed element and 4 reactively loaded passive elements connected to varactors. The key aspect explored in this paper is the implementation of the unitary array of 5 elements in a larger configuration with many modules, achieving gains on the order of 21 dB with aperture efficiency exceeding 90%. This makes this paper relevant for this thesis work, where a large amount of elements is involved. However, the use of DRA brings to fabrication complexity due to multilayer structures and slot feeding. Compared with this thesis, the presented article introduce the concept of use multiple active elements. However, it doesn't consider the array as an whole, but as many ESPAR modules toghether.

Finally, another application of ESPAR antennas is presented in [7]. In particular,

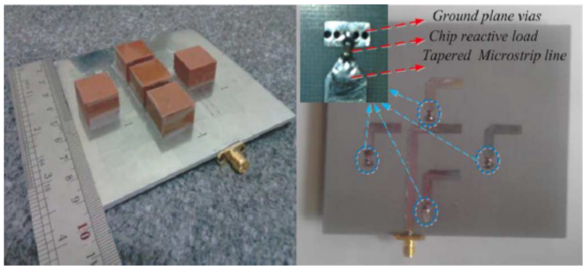

Figure 1.8: Practical realization of a single module DRA presented in [6]

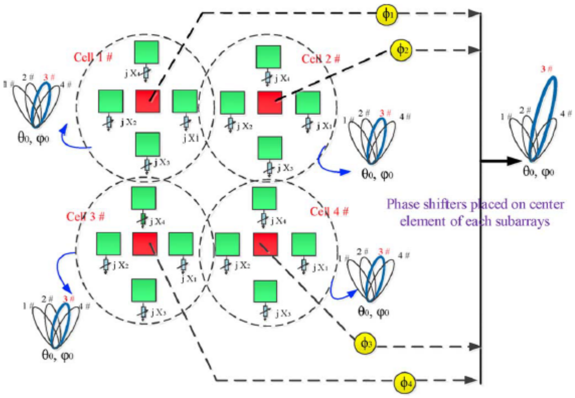

Figure 1.9: Scheme for the concept of large planar array of ESPAR DRA

the article presents an array used to estimate the DoA: the paper presents an ESPAR antenna with one central fed quarter-wavelength monopole and two rings of parasitics for a total amount of twelve passive monopoles. The passive elements are reconfigured through RF switches that set each radiator between open-circuit and short-circuit states (as seen in [2]), realizing a binary vector: $\mathbf{V} = [v_1, \ldots, v_{12}]$ with $v_s \in \{0, 1\}$, which defines whether a parasitic acts as director or reflector. This antenna enables generation of three distinct beam families characterized by different elevation maxima: $\theta_{\text{max,up}} = 46^\circ$, $\theta_{\text{max,mid}} = 52^\circ$, and $\theta_{\text{max,down}} = 56^\circ$, each containing six azimuthal beam states spaced by 60° and so the array is able to steer the field both in azimuthal and elevation planes. According to measured results, the realized gain remains approximately constant across configurations at 8 dB, input matching measurements show $|S_{11}| \leq -10\,\text{dB}$ for most configurations. The working frequency is 2.44 GHz and the antenna is meant to be used in WSN. The article is notable for its use of more elements than usual ESPAR seen in literature, but the lower frequency used and the use of switching elements instead of varactors make it far from this thesis work.

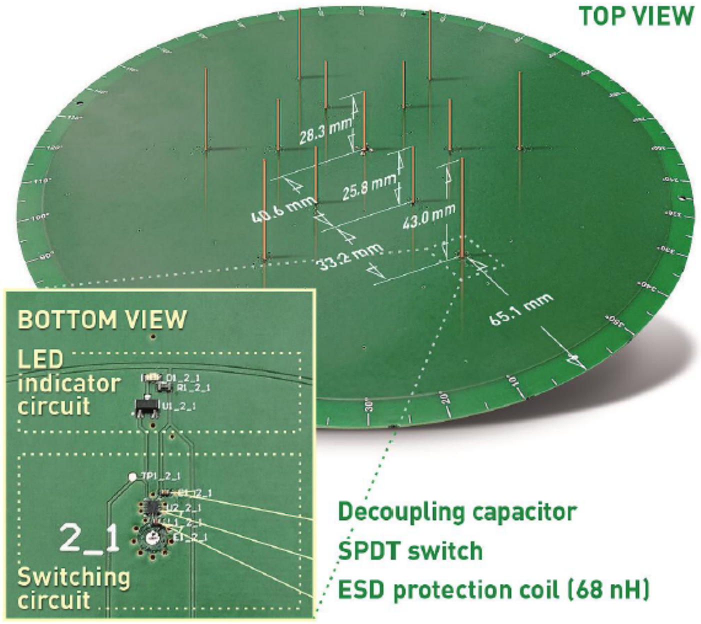

Figure 1.10: Structure of the two-rows ESPAR presented in [7] with focus on the switching element

1.3 Toward DSA

A first step beyond classical single-feed ESPAR architectures toward structures closer to the present work is represented by the multiport parasitic array radiator (MuPAR) concept developed by Ohira *et al.* [8]. In this case, the antenna is no longer a single central fed element, but consists of two inverted–F radiators and two parasitic elements loaded with variable reactances, forming a four–element array operating at 2.45 GHz. Differently from classic ESPARs, for which pattern synthesis is obtained by tuning passive loads, the MuPAR has two independent controls: excitation coefficients at the active ports and reactive loads at parasitic elements. This double control mechanism significantly increases the beamforming flexibility and degrees of freedoms, but on the other side makes the optimization more difficult. To obtain this, the authors derive a generalized analytical model thanks to which is possible to obtain an efficient determination of optimal excitations and reactances. More in detail: the elements are set symmetrically on orthogonal axes with inter-element spacings d_{12} and d_{34}, and each horizontal arm of the inverted-F radiator is folded to reduce the occupied area. A generalized model considers each radiator as two infinitesimal vertical current sources corresponding to the feed branch and shorting pin, leading to a full impedance matrix of dimension $2K \times 2K$ that shows coupling among all ports and reactive loads. The directive gain is also defined and maximized by an optimization algorithm performed to obtain excitation and reactance values. The four elements MuPAR antenna, consisting of two active and two passive elements, is able of steering the main beam over the full 360° azimuth range while maintaining a directive gain of approximately $7 \pm 1\,\text{dB}$. This work is particularly interesting for this thesis because it introduce the multiport concept that links parasitic arrays and conventional phased arrays while preserving low RF chain number.

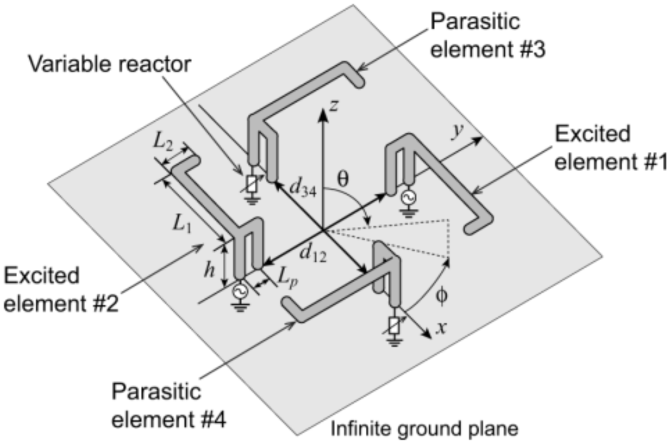

Figure 1.11: Four-element inverted-F MuPAR antenna presented in [8]

Another innovative article presentig an array working at the same frequency of this work is the 28GHz array proposed by Zhang *et al.* [9], specifically done for 5G mobile terminals. The structure consists of one active and two parasitic forming a miniaturized linear array embedded in polypropilene block. The active monopole is fed through a SIW and the beam steering is achieved not thanks to varactors but via two switches that connect each parasitic to short circuited transmission lines of different electrical lengths, obtaining in this way discrete reactive loads. The array is supported by a polypropylene dielectric block with relative permittivity $\varepsilon_r \approx 2.27$ and very low loss tangent ($\tan\delta \approx 3 \times 10^{-4}$ at 28 GHz). The impedance bandwidth covers 26.5–31 GHz for $|S_{11}| < 10\,\text{dB}$ and the radiation analysis shows that with seven switching states the antenna can scan from approximately 180° to 360° with realized gain greater then 7.5 dBi fro most of the 27.5–29.5 GHz band and exceeding 9 dBi in the 28–29 GHz range. Compared with others ESPAR realizations (typically sub 6 GHz), this design is important for this thesis since it works in mm-wave regime, but as in other previously explored articles, the number of elements is little (just 2 parasitics) with respect to this thesis work. Moreover, the use of a SIW makes the design hard to be implemented and scalable to more elements and the use of switches instead of varactors reduces the beam-steering degrees of freedom.

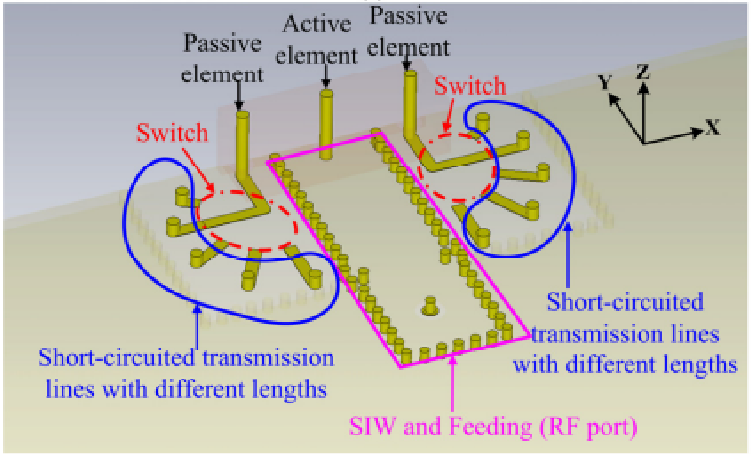

Figure 1.12: The general view of different major parts in one array with surface copper, substrate and PP dielectric block hidden presented in [9]

Finally, the dielectric-embedded ESPAR concept (DE-ESPAR) presents an array where radiating elements are directly embedded into dielectric instead of being mounted above a ground plane, similarly to the structure presented in this thesis work. Many works present this kind of antenna: The DE-ESPAR proposed by Lu *et al.* [10] presents an array immersed in a dielectric overlay with relative permittivity $\varepsilon_r \approx 4.5$. This reduces the effective wavelength to

$$\lambda_d = \frac{\lambda_0}{\sqrt{\varepsilon_r}},$$

bringing to a substantial miniaturization of both element height and array radius. The antenna has a classical seven element topology with one driven monopole and six parasitic elements mounted on a cylindrical ground plane with a conductive skirt. The skirt height is optimized to suppress vertical radiation modes and enhance azimuthal directivity (Further details on ground plane effects in monopole antennas will be adressed in Chapter 4). The design variables $\{h_e, r_a, h_d, r_d, X_n\}$ (element dimensions, array radius, dielectric dimensions, and reactive loads) are optimized toghether using a genetic algorithm coupled with simulations involving thousands of evaluations. The optimized normalized dimensions is in the interval 0.12λ–0.24λ, demonstrating an effective electrical miniaturization. Measurements show a maximum gain of approximately 5.1 dBi at 2.48 GHz with $|S_{11}| \approx -11.5\,\text{dB}$ near 2.4 GHz. Beam steering is performed by using varactors combined with miscrostrip lines in order to obtain also positive reactance's values as was done in this work.

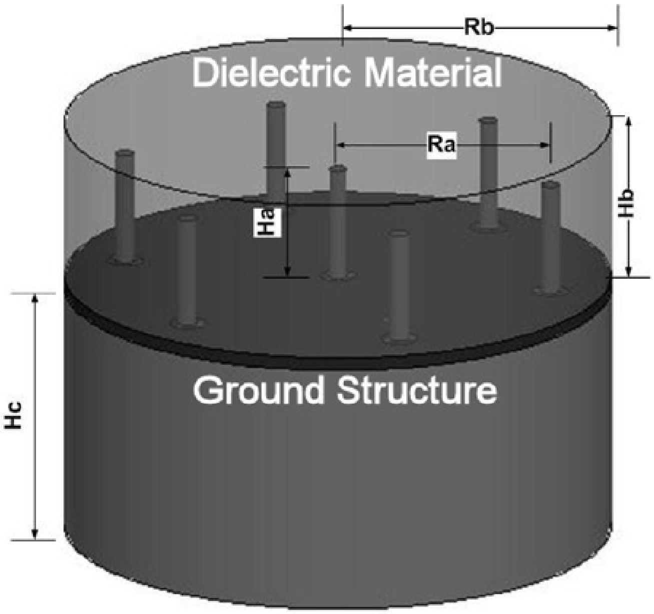

Figure 1.13: Configuration of the DE-ESPAR presented in [10]

Other two works from the same authors, based on the same antenna's structure of [10], focus on how the dielectric overlay changes the antenna's performances. In [11], the dielectric's relative permittivity is varied: $\varepsilon_r = 4$, $\varepsilon_r = 5.5$ and $\varepsilon_r = 7.5$ are the values used for a 7-elements DE-ESPAR operating around 2.45 GHz. Full-wave simulations are done for three versions of the antenna using the three different values of ε_r: by increasing its value the electrical size of the antenna is reduced and as it was expected, the main costs of increasing overlay permittivity are gain and bandwidth decrease. Approximate gain decrease is equal to 1.2 dBi per centimeter of radius reduction. The second article [12] investigates how the antenna's performances are changed by using the same overlay's material and changing its dimensions: the material utilized for that purpose is inexpensive and commonly used in 3D print technology PLA filament; since commercially available PLA filaments are not intended for precision RF applications, the dielectric permittivity is not tightly controlled by manufacturers. Moreover, the effective dielectric parameters also depend on printing resolution and fabrication settings. For this reason, the material constants adopted in the antenna design were experimentally determined from samples fabricated using the same filament spool and identical printing parameters as the final dielectric cylinder. The measured values were $\varepsilon_r = 2.74$

and $\tan\delta = 0.01$. In order to investigate the influence of overlay dimensions on antenna performance, the cylindrical superstrate height H_c and radius R_c were swept, and a set of antenna characteristics was evaluated at each point of the parameter space defined by $(R_c/\lambda_0,\ H_c/\lambda_0)$. For a free-space wavelength λ_0 corresponding to 2.45 GHz, the sweep ranges were $(0.20\ldots0.65,\ 0.14\ldots0.46)$ with a step size of $0.02\lambda_0$ (approximately 2.4 mm), while all remaining geometrical parameters were kept constant. The computed metrics included the elevation angle of maximum radiation, horizontal-plane directivity, and half-power beamwidth (HPBW). The results show that increasing R_c while maintaining H_c in the interval 0.25–0.4 leads to a simultaneous increase in elevation angle and horizontal directivity.

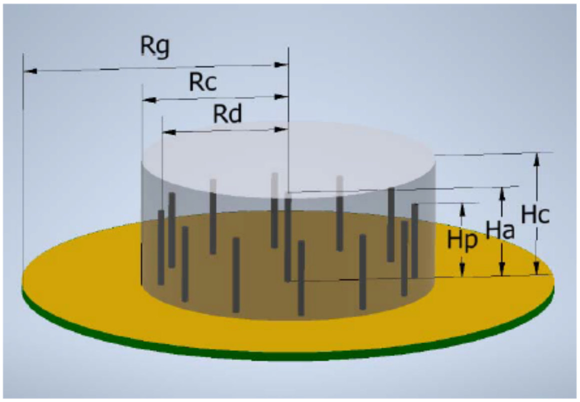

Figure 1.14: Layout of the ESPAR presented in [11]

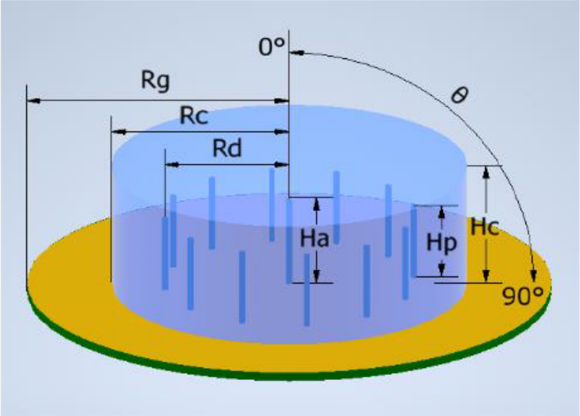

Figure 1.15: Layout of the ESPAR presented in [12]

1.4 Dynamic Scattering Array Paradigm

Finally the DSA paradigm presented in this thesis is based on the idea of Prof. Davide Dardari [13]. The proposed system consists of a limited number of active elements, each connected to an RF chain, surrounded by a cloud of reconfigurable passive scatterers whose reactive near-field coupling enables joint processing and radiation. The author derives an analytical model of the structure using a Hertzian dipole (ideal formulation), and then developes an optimization method that tunes the scatterer reactances to perform specific actions such as: beamforming, multi-user MISO transmission, and MIMO operation. Numerical results demonstrate that the strong coupling enables superdirective behavior in arbitrary directions, while in conventional arrays superdirectivity is typically restricted to end-fire radiation. Compared with SIM, where only the last layer radiates, the DSA implements simultaneous interaction among all elements, allowing higher achievable gain with significantly reduced physical size. In fact, generally the coupling is avoided, while the DSA takes advaantage of that, spacing the elements of $\lambda/4$ (Further theoretical details will be explored in Chapter 2). In this thesis work a practical implementation of this cited work is presented: monopoles are used instead of Hertzian Dipoles and layout's criticalities are presented.

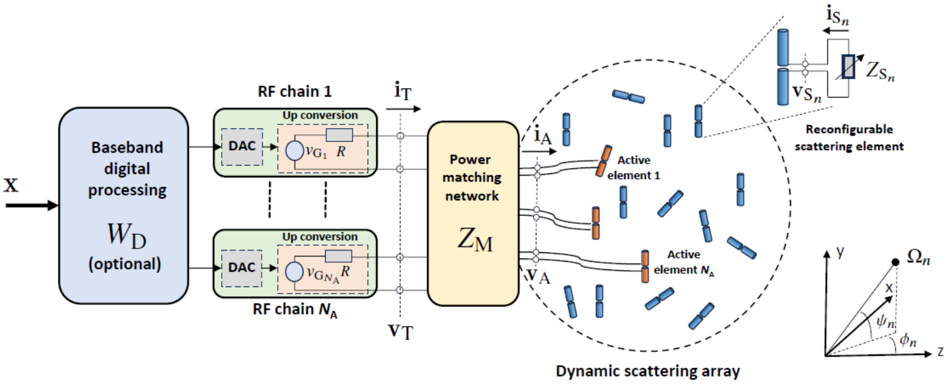

Figure 1.16: Principle scheme of a DSA presented in [13]

1.5 Innovations from this thesis

The selected articles present many different ESPAR antennas and applications. Since this thesis focuses on the array's layout, a comparison was done mainly on that aspect. In general, all the ESPAR antennas found in the literature having a similar structure to the one presented in this project, works at lower frequencies, implement few elements or focuses just on optimization algorithms [2], [3], [5], [7], [10]. On the other side, the papers presenting ESPAR antennas working at 28GHz has too complicated layouts and still use too many few elements [4] [9].

Finally, the ESPAR antenna presented in this thesis is the first working at 28GHz using a large amount of monopoles introducing the possibility of many different fed elements, the use of varactors to have continously variable loads and a compact design.

Chapter 2

Theoretical Background

The DSA presented in this thesis is a circular array of monopoles, where beam steering is enabled by continously electronically variable loads. This chapter introduces the theoretical framework used for the array design: first the ESPAR theory is presented, mainly based on Harrington's work [1]; then the DSA theory developed by Prof. Dardari [14] is addressed.

2.1 ESPAR Theory

This section presents the modeling of ESPAR antennas through the CMT [18] for an algebraic description of the array behavior. The final subsection summarizes the Univariate Search Method proposed by Harrington [1] to determine the reactive loads maximizing the gain in a given direction.

2.1.1 Problem modeling

The analysis is done in terms of N-port impedance parameters, thanks to which we have a compact description of multi-antenna systems including the mutual coupling between the elements. Fig. 2.1 shows the Thevenin equivalent of an active feed system connected to an N-port antenna system.

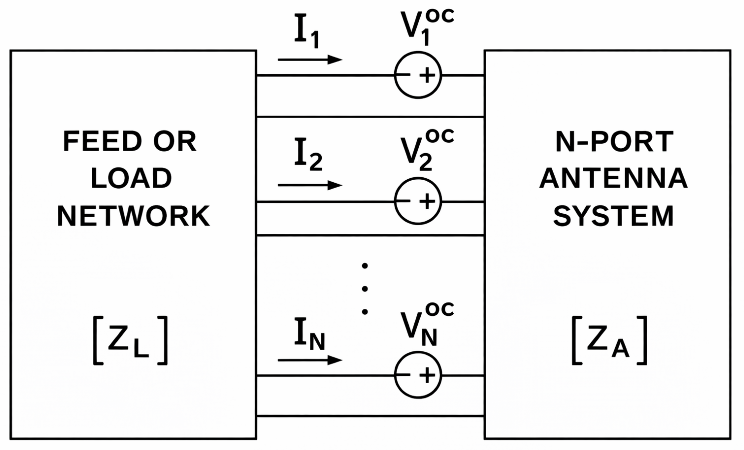

Figure 2.1: Thevenin equivalent of an N-port system.

In this specific work, the model is applied to an ESPAR antenna, where only the central element is actively fed, while the electromagnetic interaction among passive ports is described through the mutual impedances of the antenna system. The terminal equation for the feed and antenna system in Fig. 2.1 is

$$\vec{V}^{\,oc} = [Z_A + Z_L]\vec{I}, \tag{2.1}$$

where $\vec{V}^{\,oc}$ and $\vec{I}$ are the vectors collecting the Thevenin equivalent voltages and port currents, respectively. The matrices $[Z_A]$ and $[Z_L]$ are the open-circuit impedance matrices of the antenna system and the load/feed network.

The total radiated electric field E (considering a precise observation direction and polarization) is obtained by linear superposition of the fields generated by each port:

$$E = \sum_{n=1}^{N} I_n \, E_n^{oc}, \tag{2.2}$$

where E_n^{oc} is the field radiated when a unit current exists at port n and all other ports are open-circuited. In matrix form, (2.2) can be written as

$$E = \vec{E}^{\,oc}\,\vec{I}, \tag{2.3}$$

where $\vec{E}^{\,oc}$ is the vector collecting the E_n^{oc}. Solving (2.1) for $\vec{I}$ and substituting into

(2.3) gives the explicit relation between excitation voltages and radiated field:

$$E = \vec{E}^{oc}\left([Z_A + Z_L]\right)^{-1}\vec{V}^{oc}. \tag{2.4}$$

The current distribution over the antenna is also considered. It is linearly related to the excitation voltages through the same operator and so it can be written in same form:

$$\vec{J} = \vec{J}^{oc}\,[Z_A + Z_L]^{-1}\vec{V}^{oc}, \tag{2.5}$$

where $\vec{J}^{oc}$ is the vector collecting J_n^{oc}, i.e., the antenna current distribution when a unit current exists at port n and all other ports are open-circuited.

The above formulation is general, applying to any feed network connected to any antenna system. For the ESPAR case, the load matrix $[Z_L]$ is typically diagonal (independent terminations at the ports), with purely reactive elements jX_{Li}.

2.1.2 Modal description, resonance condition, and gain optimization

The following development is based on [1, 18, 19, 20]. For sake of clarity, $\tilde{(\cdot)}$ means transpose and $(\cdot)^*$ complex conjugation; hence $\tilde{(\cdot)}^*$ means Hermitian transpose.

Hermitian decomposition. Starting from the impedance matrix in (2.1), let's define

$$[Z] \triangleq [Z_A + Z_L] = [R] + j[X], \tag{2.6}$$

where $[R]$ and $[X]$ are, respectively, the resistance and reactance matrices:

$$[R] = \frac{1}{2}\big([Z] + [Z]^*\big), \tag{2.7}$$

$$[X] = \frac{1}{2j}\big([Z] - [Z]^*\big). \tag{2.8}$$

Characteristic modes. Characteristic port-current modes are introduced through a weighted eigenvalue equation [18]. Harrington starts from the generalized eigenproblem

$$[Z]\vec{I}_n = v_n\,[M]\vec{I}_n, \tag{2.9}$$

where v_n are eigenvalues, $\vec{I}_n$ are modal port-current eigenvectors, and $[M]$ is a real symmetric weighting matrix. With $[M] = [R]$ and the re-parameterization

$$v_n = 1 + j\lambda_n, \tag{2.10}$$

(2.9) becomes

$$[Z]\vec{I}_n = (1 + j\lambda_n)\,[R]\vec{I}_n. \tag{2.11}$$

Substituting (2.6) into (2.11) and cancelling the common $[R]\vec{I}_n$ terms givs the real generalized eigenvalue equation

$$[X]\vec{I}_n = \lambda_n[R]\vec{I}_n. \tag{2.12}$$

$[R]$ and $[X]$ are real symmetric; therefore $\lambda_n \in \mathbb{R}$ and the eigenvectors can be chosen real (more generally, equiphasal).

Power and normalization. The time-average power radiated and/or dissipated by a port-current vector $\vec{I}$ is

$$P = \frac{1}{2}\,\tilde{I}^*\big([Z] + [Z]^*\big)\vec{I} = \tilde{I}^*[R]\vec{I}, \tag{2.13}$$

(see [21] for further insights on the derivation).

For convenience, modal currents are normalized to unit power:

$$\tilde{I}_n^*[R]\vec{I}_n = 1. \tag{2.14}$$

With this normalization, the orthogonality relations are

$$\tilde{I}_m^*[R]\vec{I}_n = \delta_{mn}, \tag{2.15}$$

$$\tilde{I}_m^*[X]\vec{I}_n = \lambda_n\,\delta_{mn}, \tag{2.16}$$

$$\tilde{I}_m^*[Z]\vec{I}_n = (1 + j\lambda_n)\,\delta_{mn}, \tag{2.17}$$

where δ_{mn} is the Kronecker delta. Since the modes are real/equiphasal, orthogonality remains valid even without conjugating the first vector in some intermediate manipulations.

Rayleigh quotient and energetic interpretation. A useful characterization of λ_n follows from the Rayleigh quotient and is clearly explained in [20]:

$$\lambda_n = \frac{\tilde{I}_n^*[X]\vec{I}_n}{\tilde{I}_n^*[R]\vec{I}_n}. \tag{2.18}$$

The quadratic forms in (2.18) admit an energetic interpretation. In particular,

$$P_n = \frac{1}{2}\,\tilde{I}_n^*[R]\vec{I}_n, \tag{2.19}$$

is the active power radiated/dissipated by the n-th mode, while

$$Q_n = \frac{1}{2}\,\tilde{I}_n^*[X]\vec{I}_n \;\approx\; 2\omega\big(W_{m,n} - W_{e,n}\big), \tag{2.20}$$

is the reactive one where $W_{m,n}$ and $W_{e,n}$ are, respectively, the magnetic and electric stored energies associated with the n-th modal current. Hence

$$\lambda_n = \frac{Q_n}{P_n} \;\approx\; \frac{2\omega\big(W_{m,n} - W_{e,n}\big)}{P_n}, \tag{2.21}$$

which clarifies that λ_n measures the balance between stored reactive energy and radiated/dissipated power for a given current mode. Moreover, $\lambda_n > 0$ corresponds to an inductive mode ($W_{m,n} > W_{e,n}$), whereas $\lambda_n < 0$ indicates a capacitive mode ($W_{m,n} < W_{e,n}$). The resonance condition is

$$\lambda_n = 0 \quad\Longleftrightarrow\quad Q_n = 0 \quad\Longleftrightarrow\quad W_{m,n} = W_{e,n}. \tag{2.22}$$

N.B. Both λ_n and $\vec{I}_n$ vary with frequency; therefore the modal set must be evaluated at the frequency of interest.

Modal expansion of port currents and fields. Any physically realizable port-current vector can be expanded in the modal basis:

$$\vec{I} = \sum_{n=1}^{N} \alpha_n\,\vec{I}_n, \tag{2.23}$$

where α_n are coefficients determined from the excitation. Substituting (2.23) into (2.1) gives

$$\vec{V}^{\,oc} = \sum_{n=1}^{N} \alpha_n \, [Z] \vec{I}_n. \tag{2.24}$$

Left-multiplying by $\tilde{I}_m^*$ yields

$$\tilde{I}_m^* \vec{V}^{\,oc} = \sum_{n=1}^{N} \alpha_n \, \tilde{I}_m^* [Z] \vec{I}_n. \tag{2.25}$$

Using (2.17), only the term $n = m$ remains:

$$\tilde{I}_n^* \vec{V}^{\,oc} = \alpha_n (1 + j\lambda_n), \tag{2.26}$$

therefore

$$\alpha_n = \frac{\tilde{I}_n^* \vec{V}^{\,oc}}{1 + j\lambda_n}. \tag{2.27}$$

Substituting (2.27) into (2.23) brings to the explicit modal solution for the port currents:

$$\vec{I} = \sum_{n=1}^{N} \frac{\tilde{I}_n^* \vec{V}^{\,oc}}{1 + j\lambda_n} \, \vec{I}_n. \tag{2.28}$$

Similarly, any linear output depending on the currents can be written as a modal sum. Being $\mathbf{E}(\vec{I}_n)$ the far field produced by the modal port current $\vec{I}_n$, the total field is

$$\mathbf{E} = \sum_{n=1}^{N} \frac{\tilde{I}_n^* \vec{V}^{\,oc}}{1 + j\lambda_n} \, \mathbf{E}(\vec{I}_n), \tag{2.29}$$

and the total current on the scatterer admits an analogous expansion:

$$\mathbf{J} = \sum_{n=1}^{N} \frac{\tilde{I}_n^* \vec{V}^{\,oc}}{1 + j\lambda_n} \, \mathbf{J}(\vec{I}_n). \tag{2.30}$$

When a mode is resonant ($\lambda_n = 0$) while the remaining modes have relatively large $|\lambda_n|$, the dominant contribution to (2.28) and (2.29) comes from the resonant mode. In that case, the field can be approximated by the dominant (resonant) term.

Resonating a desired current through reactive loads. If one wants to enforce a specific port-current vector $\vec{I}$, it can be done by properly selecting the load network.

Let

$$[Z_A] = [R_A] + j[X_A], \qquad [Z_L] = [R_L] + j[X_L],$$

so that $[X] = [X_A] + [X_L]$ in (2.6). A selected $\vec{I}$ can be made resonant (i.e., an eigencurrent with $\lambda = 0$) by enforcing

$$[X]\vec{I} = \big([X_A] + [X_L]\big)\vec{I} = 0, \tag{2.31}$$

equivalently

$$[X_L]\vec{I} = -[X_A]\vec{I}. \tag{2.32}$$

Independent reactive terminations at each port correspond to a diagonal matrix

$$[X_L] = \begin{bmatrix} X_{L1} & 0 & \cdots & 0 \\ 0 & X_{L2} & \cdots & 0 \\ \vdots & \vdots & \ddots & \vdots \\ 0 & 0 & \cdots & X_{LN} \end{bmatrix}. \tag{2.33}$$

In this case, the i-th diagonal element required to resonate $\vec{I}$ is obtained component-wise from (2.32):

$$X_{Li} = -\frac{1}{I_i}\big([X_A]\vec{I}\big)_i, \tag{2.34}$$

Practically, (2.34) highlights that the required reactive loads depend not only on the desired current vector, but also on the mutual coupling expressed in $[X_A]$.

If a single resonant mode r dominates, (2.29) reduces to the dominant-mode approximation

$$\mathbf{E} \approx \frac{\tilde{I}_r^{*}\vec{V}^{\,oc}}{1 + j\lambda_r}\,\mathbf{E}(\vec{I}_r) \;\approx\; \big(\tilde{I}_r^{*}\vec{V}^{\,oc}\big)\,\mathbf{E}(\vec{I}_r), \qquad (\lambda_r = 0), \tag{2.35}$$

which motivates selecting and resonating a current vector associated with a desired pattern or maximum gain.

2.1.3 Summary of the Univariate Search Method

In this subsection the Univariate Search Method proposed by Harrington [1] is summarized. Differently from the approach adopted for the DSA (where loads are selected based on simulation-driven optimization), the univariate method gives an analytical method.

The directive gain of an N-port antenna excited by a port-current vector $\vec{I}$ is

$$G = \frac{k^2\eta \left|\tilde{I}\vec{V}^{\,0}\right|^2}{4\pi\, \tilde{I}^{\,*}[R]\vec{I}}, \tag{2.36}$$

where k is the wavenumber, η is the intrinsic impedance of free space, and $\vec{V}^{\,0}$ is the open-circuit port-voltage vector induced when the antenna is illuminated by a plane wave arriving from the direction in which the gain is evaluated (see [21] for a complete derivation).

From (2.1), the port currents are

$$\vec{I} = \big([Z_A] + [Z_L]\big)^{-1}\vec{V}^{\,oc}. \tag{2.37}$$

Substituting (2.37) into (2.36) yields a form where the dependence on the loads is explicit:

$$G = \frac{k^2\eta}{4\pi} \frac{\left|\tilde{V}^{\,0}\big([Z_A] + [Z_L]\big)^{-1}\vec{V}^{\,oc}\right|^2}{\tilde{I}^{\,*}[R]\vec{I}}. \tag{2.38}$$

In the ESPAR case, the loads are assumed to be purely reactive,

$$[Z_L] = j[X_L], \tag{2.39}$$

with $[X_L]$ diagonal as in (2.33). Maximizing (2.38) then becomes the optimization of G with respect to the real variables $\{X_{Li}\}$. Since $G(\{X_{Li}\})$ is generally nonlinear and non-convex, Harrington proposes varying one reactance at a time while holding all others fixed (so called univariate optimization).

When varying only the i-th reactance, separate it from the remaining loads:

$$[Z_A + jX_L] = [Z^{\,i}] + j[X_L^{i}], \tag{2.40}$$

where $[Z^{\,i}]$ denotes $[Z_A + jX_L]$ with $X_{Li} = 0$, and $[X_L^{i}]$ contains only the single nonzero element X_{Li} on the i-th diagonal entry. Introducing

$$[U^{\,i}] \triangleq \mathrm{diag}(0, \ldots, 0, \underbrace{1}_{i\text{-th}}, 0, \ldots, 0),$$

one has $[X_L^i] = X_{Li}[U^i]$. The inverse of (2.40) admits the closed-form update

$$[Z_A + jX_L]^{-1} = [Z^i]^{-1} - \frac{jX_{Li}}{1 + jX_{Li}\left([Z^i]^{-1}\right)_{ii}} [Z^i]^{-1}[U^i][Z^i]^{-1}, \tag{2.41}$$

where $\left([Z^i]^{-1}\right)_{ii}$ is the i-th diagonal element of $[Z^i]^{-1}$. Substituting (2.41) into (2.38) yields a scalar expression in which only the i-th load is variable:

$$G = \frac{k^2\eta}{4\pi\,\tilde{I}^*[R]\vec{I}} \left| \tilde{V}^0 [Z^i]^{-1}\vec{V}^{oc} - \frac{\tilde{V}^0 [Z^i]^{-1}[U^i] [Z^i]^{-1}\vec{V}^{oc}}{jB_{Li} + \left([Z^i]^{-1}\right)_{ii}} \right|^2, \tag{2.42}$$

after re-parameterizing the variable as

$$B_{Li} \triangleq -\frac{1}{X_{Li}}. \tag{2.43}$$

Hence $B_{Li} > 0$ corresponds to a capacitive termination ($X_{Li} < 0$) and $B_{Li} < 0$ to an inductive termination ($X_{Li} > 0$). The maximization of G with respect to B_{Li} is performed one load at a time, while holding $\{B_{Lm}\}_{m \neq i}$ fixed. After optimizing successively $B_{L1}, B_{L2}, \ldots, B_{LN}$, the cycle is repeated until the gain increment becomes negligible. The resulting gain sequence is non-decreasing, but it has to be saids that the method does not guarantee convergence to the global optimum because the problem is generally non-convex.

2.2 DSA Theory

The following paragraph introduces the DSA theory taken from [14].

2.2.1 Problem modeling

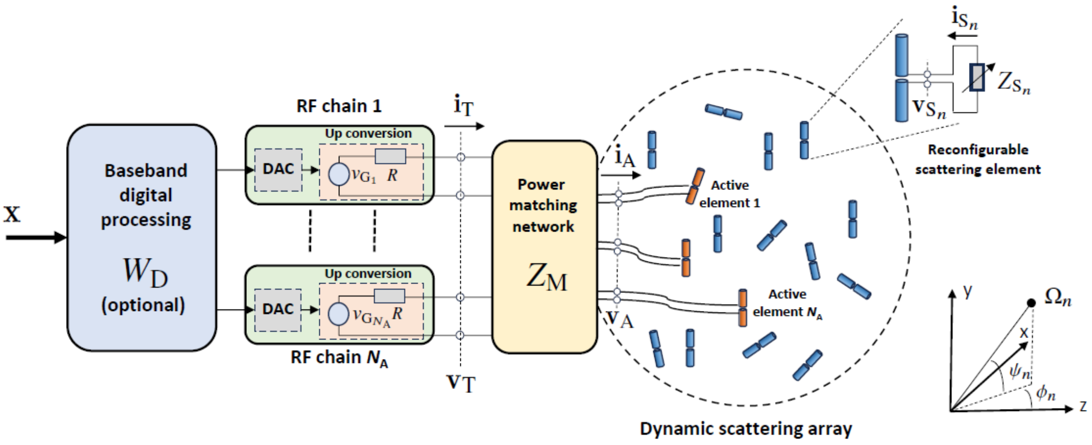

Figure 2.2: Principle scheme of a DSA presented in [14]

Let's consider a DSA with N_A active antenna elements surrounded by N_S reconfigurable passive scatterers, for a total amount of $N = N_A + N_S$ ports. Each passive element is an antenna terminated by a reconfigurable impedance load. As in Harrington theory for ESPAR, to avoid power dissipation at the passive ports, the loads are taken purely reactive:

$$Z_{Sn}(\theta_n) = j\theta_n, \qquad \theta_n \in \mathbb{R}, \qquad n = 1, \ldots, N_S. \tag{2.44}$$

Where θ_n is the reactance. Now collect the reactances in a vector $\vec{\theta} = [\theta_1, \ldots, \theta_{N_S}]^T$ and the corresponding diagonal load matrix (this means that each load is independent).

$$Z_S(\vec{\theta}) \triangleq \mathrm{diag}\big(Z_{S1}(\theta_1), \ldots, Z_{SN_S}(\theta_{N_S})\big). \tag{2.45}$$

Considering the system as an N-port network, the real-value bandpass voltage at a generic port is written as:

$$v^{(\mathrm{RF})}(t) = \sqrt{2}\,\Re\Big\{v(t)e^{j2\pi f_0 t}\Big\}\,, \tag{2.46}$$

where $v(t)$ is the complex voltage envelope and f_0 is the carrier frequency. Similarly, the bandpass current is $i^{(\mathrm{RF})}(t) = \sqrt{2}\Re\{i(t)e^{j2\pi f_0 t}\}$, where $i(t)$ is the complex current envelope. Consider a small bandwidth B around f_0, the network properties are constant in band and so the system is analyzed directly at f_0.

The average active power delivered to the port is:

$$P = \mathbb{E}\big\{\Re\big\{v^{RF}(t) i^{RF}(t)\big\}\big\} = \mathbb{E}\big\{\Re\big\{v^{*}(t) i(t)\big\}\big\}\,, \tag{2.47}$$

where $\mathbb{E}\{\cdot\}$ is the statistical expectation.

Let $\vec{v}_A, \vec{i}_A \in \mathbb{C}^{N_A \times 1}$ be the complex voltages and currents at the active ports, and $\vec{v}_S, \vec{i}_S \in \mathbb{C}^{N_S \times 1}$ those at the scatterer ports. All these quantities can be collected in vectors as:

$$\vec{i} = \begin{bmatrix} \vec{i}_A \\ \vec{i}_S \end{bmatrix}, \qquad \vec{v} = \begin{bmatrix} \vec{v}_A \\ \vec{v}_S \end{bmatrix}. \tag{2.48}$$

All mutual interactions among the elements are expressed by the impedance matrix $[Z] \in \mathbb{C}^{N \times N}$ (which does not depend on the loads), relating voltages and currents as

$$\vec{v} = [Z]\vec{i}. \tag{2.49}$$

Partitioning $[Z]$ according to active/scatterer ports brings to

$$\begin{bmatrix} \vec{v}_A \\ \vec{v}_S \end{bmatrix} = \begin{bmatrix} [Z_{AA}] & [Z_{AS}] \\ [Z_{SA}] & [Z_{SS}] \end{bmatrix} \begin{bmatrix} \vec{i}_A \\ \vec{i}_S \end{bmatrix}. \tag{2.50}$$

At the scatterer ports, it is:

$$\vec{v}_S = -[Z_S(\vec{\theta})]\vec{i}_S. \tag{2.51}$$

Substituting (2.51) into (2.50) gives:

$$-[Z_S(\vec{\theta})]\vec{i}_S = [Z_{SA}]\vec{i}_A + [Z_{SS}]\vec{i}_S \quad \Longrightarrow \quad \big([Z_{SS}] + [Z_S(\vec{\theta})]\big)\vec{i}_S = -[Z_{SA}]\vec{i}_A,$$

so it becomes:

$$\vec{i}_S = -\big([Z_{SS}] + [Z_S(\vec{\theta})]\big)^{-1}[Z_{SA}]\,\vec{i}_A. \tag{2.52}$$

Replacing (2.52) into (2.50) gives an input realation at the active ports:

$$[Z_A(\vec{\theta})] = [Z_{AA}] - [Z_{AS}]\big([Z_{SS}] + [Z_S(\vec{\theta})]\big)^{-1}[Z_{SA}]. \tag{2.53}$$

where

$$\vec{v}_A = [Z_A(\vec{\theta})]\vec{i}_A, \tag{2.54}$$

is the input relation at ports.

From (2.54) it is possible to see how the input impedance depends on the scatter's loads: $[Z_S(\vec{\theta})]$.

The N_A active ports are connected to N_A RF chains through a $2N_A$-port matching network to maximize the power transfer. $\vec{v}_T, \vec{i}_T$ are voltages and currents at the RF-chain ports, and assume each chain has output resistance R. The matching network can be descibed as:

$$\begin{bmatrix} \vec{v}_T \\ \vec{v}_A \end{bmatrix} = [Z_M(\vec{\theta})] \begin{bmatrix} \vec{i}_T \\ -\vec{i}_A \end{bmatrix}, \tag{2.55}$$

with

$$[Z_M(\vec{\theta})] = \begin{bmatrix} 0 & -j\sqrt{R}\,\Re\{[Z_A(\vec{\theta})]\}^{\frac{1}{2}} \\ -j\sqrt{R}\,\Re\{[Z_A(\vec{\theta})]\}^{\frac{1}{2}} & -j\,\Im\{[Z_A(\vec{\theta})]\} \end{bmatrix}. \tag{2.56}$$

From this relation (derived by [22]) it is possible to see how the matching network depends on the DSA input impdeance, which depends itself on variable loads. So the matching network should be able to adapt to the variable loads. (Adaptive matching network should be used).

Assuming lossless antenna elements, the transmitted power equals the radiated power:

$$P_T = P_{\text{rad}} = \mathbb{E}\left\{\tilde{i}_A^* \Re\{[Z_A(\vec{\theta})]\}\vec{i}_A\right\} = \mathbb{E}\left\{\frac{\tilde{v}_T^* \vec{v}_T}{R}\right\}, \tag{2.57}$$

The reactive power is

$$P_{\text{react}} = \mathbb{E}\left\{\tilde{i}_A^* \Im\{[Z_A(\vec{\theta})]\}\vec{i}_A\right\}, \tag{2.58}$$

and the Q-factor is defined as

$$Q \triangleq \frac{P_{\text{react}}}{P_{\text{rad}}}. \tag{2.59}$$

For $Q \gg 1$, Q^{-1} can be used as indicator of the achievable bandwidth.

An optional digital precoder $[W_D] \in \mathbb{C}^{N_A \times N_A}$ maps the information vector $\vec{x} \in \mathbb{C}^{N_A \times 1}$ into the RF-chain voltages:

$$\vec{v}_T = [W_D]\vec{x}, \qquad \|[W_D]\|_F = \sqrt{RN_A}. \tag{2.60}$$

Where the normalization ensures that $P_T = \mathbb{E}\{\tilde{x}^* \vec{x}\}$.

Combining (2.55) and (2.56) abd substituting (2.62) it is:

$$\vec{i}_A = [M(\vec{\theta})][W_D]\vec{x}. \tag{2.61}$$

The total current flowing in the whole DSA (active + scatterers) follows from (2.52):

$$\vec{i} = \begin{bmatrix} [I_{N_A}] \\ -\big([Z_{SS}] + [Z_S(\vec{\theta})]\big)^{-1}[Z_{SA}] \end{bmatrix} \vec{i}_A \ \triangleq \ [C(\vec{\theta})]\vec{i}_A. \tag{2.62}$$

Finally, substituting (2.61) into (2.62) gives a direct relation from $\vec{x}$ to the DSA total current vector:

$$\vec{i} = [C(\vec{\theta})][M(\vec{\theta})][W_D]\vec{x} \ \triangleq \ [W_{\mathrm{EM}}(\vec{\theta})][W_D]\vec{x}, \tag{2.63}$$

where $[W_{\mathrm{EM}}(\vec{\theta})]$ denotes the EM-level signal processing performed by mutual coupling and reconfigurable loads. It's expression is:

$$[W_{\mathrm{EM}}(\vec{\theta})] = \frac{1}{j\sqrt{R}} \begin{bmatrix} \Re\{[Z_A(\vec{\theta})]\}^{-\frac{1}{2}} \\ -\big([Z_{SS}] + [Z_S(\boldsymbol{\theta})]\big)^{-1}[Z_{SA}]\,\Re\{[Z_A(\vec{\theta})]\}^{-\frac{1}{2}} \end{bmatrix}. \tag{2.64}$$

Now if consider K test points at positions $\vec{t}_k$ in the far-field region. Let $[H_c] \in \mathbb{C}^{K\times N}$ be the transimpedance matrix of the radio channel accounting for the propagation effeects and $[H(\vec{\theta}, [W_D])]$ is the baseband equivalent channel matrix as commonly definded in signal processing, then:

$$\vec{y} = [H_c]\vec{i} = [H_c][W_{\mathrm{EM}}(\vec{\theta})][W_D]\vec{x} \ \triangleq \ [H(\vec{\theta}, [W_D])]\vec{x}. \tag{2.65}$$

So finally it is possible to observe how the useful received signal depends both on the digital signal processing ($[W_D]$) and on the reactive loads ($\vec{\theta}$).

2.2.2 DSA with Hertzian Dipoles

To obtain an analytical model, each DSA element (active or scatterer) is approximated as a very short dipole of length l_n and radius r_n with $l_n, r_n \ll \lambda$, oriented as

$$\boldsymbol{\Omega}_n = \big[\sin(\phi_n)\cos(\psi_n),\ \sin(\phi_n)\sin(\psi_n),\ \cos(\phi_n)\big]^T. \tag{2.66}$$

The n-th entry of $\vec{i}$ is the current flowing into the port of the n-th dipole.

The total current density distribution is

$$\mathbf{J}(\mathbf{p}) = \sum_{n=1}^{N} \boldsymbol{\Omega}_n \, l_n \, i_n \, \delta(\mathbf{p} - \mathbf{p}_n). \tag{2.67}$$

The electric field at a generic point $\mathbf{p}$ is obtained thanks to the Green's dyadic $G_{EJ}(\cdot)$:

$$\mathbf{E}(\mathbf{p}) = \int_{\mathcal{V}} G_{EJ}(\mathbf{p} - \mathbf{s}) \, \mathbf{J}(\mathbf{s}) \, d\mathbf{s}. \tag{2.68}$$

the Green dyadic used is:

$$G_{EJ}(\mathbf{r}) = -j \, \frac{\eta \, e^{-j\kappa_0 \|\mathbf{r}\|}}{2\lambda \|\mathbf{r}\|} \left[\left(I - \hat{\mathbf{r}}\hat{\mathbf{r}}^T \right) + j \frac{\lambda}{2\pi \|\mathbf{r}\|} \left(I - 3\hat{\mathbf{r}}\hat{\mathbf{r}}^T \right) - \frac{\lambda^2}{(2\pi \|\mathbf{r}\|)^2} \left(I - 3\hat{\mathbf{r}}\hat{\mathbf{r}}^T \right) \right], \tag{2.69}$$

where $\kappa_0 = 2\pi/\lambda$, $\hat{\mathbf{r}} = \mathbf{r}/\|\mathbf{r}\|$is the wavenumber, and for the three grouped terms the multiplying factors are $1/\|\mathbf{r}\|$, $1/\|\mathbf{r}\|^2$, and $1/\|\mathbf{r}\|^3$. Substituting (2.67) into (2.68) brigs to:

$$\mathbf{E}(\mathbf{p}) = \sum_{n=1}^{N} l_n \, i_n \, G_{EJ}(\mathbf{p} - \mathbf{p}_n) \, \boldsymbol{\Omega}_n. \tag{2.70}$$

The open-circuit voltage at the m-th dipole due to the current i_n at the n-th dipole (all other currents zero) is

$$V_m^{(oc)} = l_m l_n \, i_n \, \boldsymbol{\Omega}_m^T G_{EJ}(\mathbf{p}_m - \mathbf{p}_n) \boldsymbol{\Omega}_n. \tag{2.71}$$

Therefore, for $m \neq n$ the mutual impedance coefficient is

$$Z_{m,n} = \frac{V_m^{(oc)}}{i_n} = l_m l_n \, \boldsymbol{\Omega}_m^T G_{EJ}(\mathbf{p}_m - \mathbf{p}_n) \boldsymbol{\Omega}_n, \qquad (m \neq n). \tag{2.72}$$

For $m = n$, the self-impedance of the Hertzian dipole is

$$Z_{n,n} = \frac{2}{3} \pi \eta \left(\frac{l_n}{\lambda} \right)^2 + \frac{\ln\left(\frac{l_n}{r_n} \right)}{j f_0 \pi^2 \epsilon \, l_n}. \tag{2.73}$$

Equations (2.72) and (2.73) pgive an analytical way to express the impedance matrix $[Z]$ (so the submatrices in (2.50)) starting from the DSA geometry.

Now let the k-th receiving test antenna be located at $\mathbf{t}_k$ and have polarization direction $\mathbf{\Theta}_k$. The received field components are:

$$e_k = \mathbf{\Theta}_k^T \mathbf{E}(\mathbf{t}_k) = \sum_{n=1}^{N} l_n \, \mathbf{\Theta}_k^T G_{EJ}(\mathbf{t}_k - \mathbf{p}_n) \mathbf{\Omega}_n \, i_n. \tag{2.74}$$

Assuming matched load (with receive gain G_R), the received signal is

$$y_k = e_k \sqrt{\frac{\lambda^2 G_R}{4\pi\eta}}. \tag{2.75}$$

The (k,n)-th entry of the transimpedance matrix is

$$[H_c]_{k,n} = \sqrt{\frac{\lambda^2 G_R}{4\pi\eta}} \, l_n \, \mathbf{\Theta}_k^T G_{EJ}(\mathbf{t}_k - \mathbf{p}_n) \mathbf{\Omega}_n. \tag{2.76}$$

If $\|\mathbf{t}_k - \mathbf{p}_n\| \gg \lambda$, the reactive terms in (2.69) can be neglected, giving the far-field approximation

$$G_{EJ}(\mathbf{r}) \simeq -j \, \frac{\eta \kappa_0}{4\pi \|\mathbf{r}\|} \, e^{-j\kappa_0 \|\mathbf{r}\|} \left(I - \hat{\mathbf{r}} \hat{\mathbf{r}}^T \right), \tag{2.77}$$

which directly gives a simplified expression for $[H_c]_{k,n}$ by substituting (2.77) into (2.76).

Chapter 3

Planar Layout

The main objective of this thesis is the practical realization of a $N = 127$ element array operating at 28 GHz, for future 6G architectures. In the ideal case introduced in the previous chapters, each radiator is modeled as a PEC dipole in vacuum. This chapter presents the first planar layout done to pass from the ideal array into a physically realizable structure. The adopted design choices are discussed together with the main criticalities that emerged during the simulations, with particular emphasis on finite ground effects and mutual coupling.

3.1 Design objective

Starting from the ideal scenario, the practical realization at 28GHz has many problems: even small modifications of the geometry can produce measurable variations in antenna behavior (e.g., parasitic currents flowing on the ground and edge effects). This sensitivity is largely due to the millimetric wavelength at 28GHz, for which any small change in the structure brings to possible spurious effects.

The first implementation was done in planar technology, because thanks to that there is the possibility of integrating radiating elements and their feeding network within a compact and low profile platform. The development started from the design and verification of a single printed monopole, and so proceeded to a first array prototype consisting of a central element surrounded by a ring of six elements.

3.2 Printed monopole

As a first practical step, a printed monopole was investigated at $f_0 = 28$ GHz. From the reference theory, the arm length is expected to be close to $\lambda_0/4$ and the target input impedance was set as

$$Z_{\text{in,ref}} = 73 + j\,42\ \Omega \qquad \text{at 28 GHz,} \tag{3.1}$$

consistently with [13] and with[23].

3.2.1 Layout

Substrate and metallization choice

The monopole was implemented on a single substrate layer with metallization on both faces. The selected substrate is Rogers RO3003, characterized by relative permittivity $\varepsilon_r = 3$, relative permeability $\mu_r = 1$, loss tangent $\tan\delta = 0.001$, and thermal conductivity $k_{\text{th}} \approx 0.5$ W/(K m). An interesting practical property is the substrate flexibility, which makes it possible to bend the antena in order to form ring configurations.

The stack-up consists of a dielectric layer of thickness

$$h_{\text{sub}} = 0.256 \text{ mm}, \tag{3.2}$$

and top and bottom copper layers of thickness

$$h_{\text{met}} = 0.035 \text{ mm}. \tag{3.3}$$

The top metallization hosts the feed line and radiating arm, while the bottom metallization implements a finite ground plane.

Geometry

The substrate is rectangular, with dimensions

$$L_{\text{sub}} = 4.5 \text{ mm}, \qquad W_{\text{sub}} = 4.0 \text{ mm}. \tag{3.4}$$

On the top metallization, the radiator is a narrow strip connected to a microstrip feed line. The geometrical parameters are

$$L_{\text{arm}} = 2.27 \text{ mm}, \qquad W_{\text{arm}} = 0.67 \text{ mm}, \tag{3.5}$$

for the radiating arm, and:

$$L_{\text{feed}} = 1.00 \text{ mm}, \qquad W_{\text{feed}} = 0.28 \text{ mm}, \tag{3.6}$$

for the microstrip feed section.

On the bottom side, a truncated ground plane of length

$$L_{\text{gnd}} = 1.00 \text{ mm} \tag{3.7}$$

and width equal to W_{sub} is employed.

The excitation is applied through a waveguide port defined following CST port guidelines, with dimensions chosen to excite the quasi-TEM mode of the microstrip line.

Sizing and tuning

The sizing of the printed monopole started from the freespace quarter wavelength:

$$L_{\text{arm},0} = \frac{\lambda_0}{4}, \qquad \lambda_0 = \frac{c_0}{f_0}. \tag{3.8}$$

At 28 GHz, $\lambda_0 \approx 10.7$ mm, so $\lambda_0/4 \approx 2.67$ mm. Ideally, the dielectric presence should have limited impact because the dominant field should be in the air; however, in practice part of the fringing field penetrates into the substrate and this leads to the tuned value $L_{\text{arm}} = 2.27$ mm in (3.5), selected to satisfy the impedance target (3.1).

Besides the arm length, the finite ground plane plays a relevant role in both resonance and impedance, because the truncated ground has same lenght of the feeeding line on the other side. For this reason, the tuning process is not limited to scaling L_{arm}, but also requires iterative adjustment of the ground geometry. Moreover, at 28 GHz small changes in strip dimensions (tens of micrometers) correspond to non negligible electrical variations; therefore, fine parametric sweeps were required to meet (3.1).

Finally, the feed line width was chosen so that the microstrip characteristic impedance is close to the desired reference level from the theory; with $W_{\text{feed}} = 0.28$ mm the line impedance is approximately

$$Z_0 \approx 73.45\ \Omega. \tag{3.9}$$

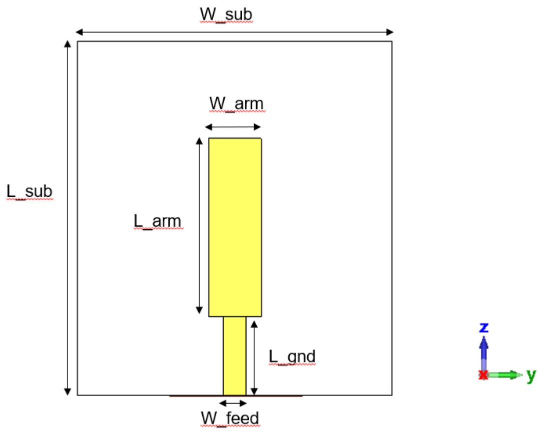

Figure 3.1: Single printed monopole: front view (top metallization).

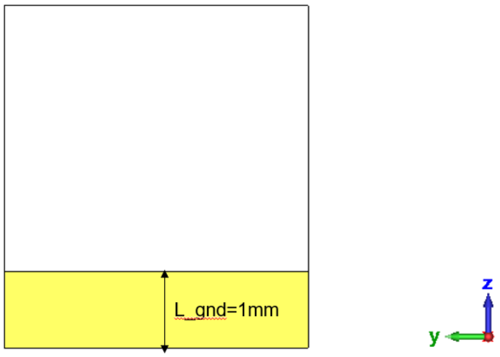

Figure 3.2: Single printed monopole: back view (bottom ground).

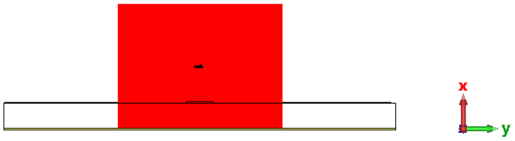

Figure 3.3: Single printed monopole: lateral view and port definition.

3.2.2 Results

S_{11}

The simulated reflection coefficient amplitude is below -10 dB, showing good result even though the required input impedance value is not purely real. In particular,

$$S_{11}(28\ \text{GHz}) \approx -11.65\ \text{dB}. \tag{3.10}$$

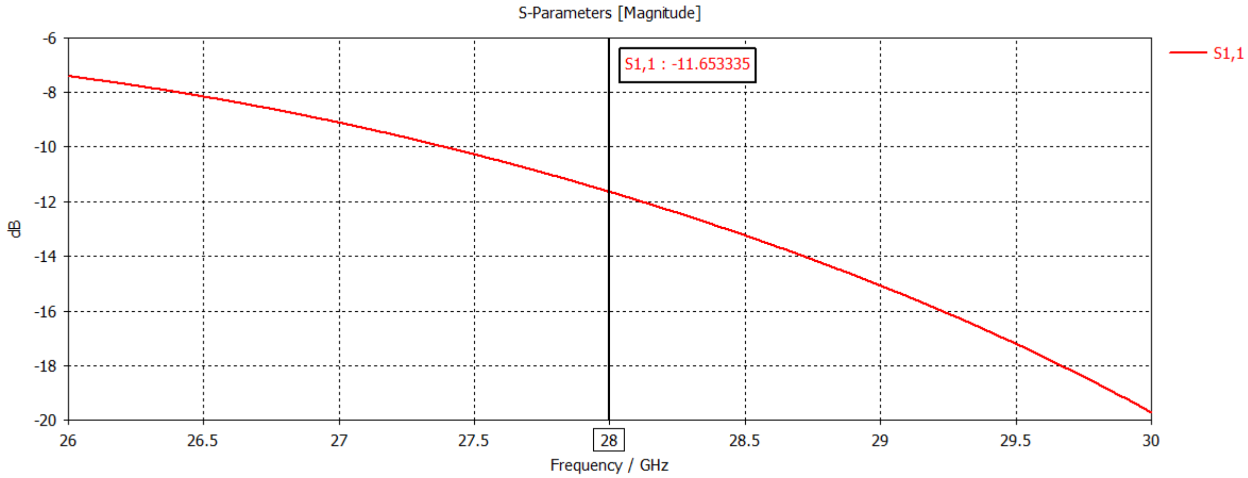

Figure 3.4: Single printed monopole: S_{11}.

Z_{in}

The input impedance extracted at the feed is

$$Z_{\text{in}} \approx 73 + j\,40\ \Omega, \tag{3.11}$$

which is close to the reference target (3.1).

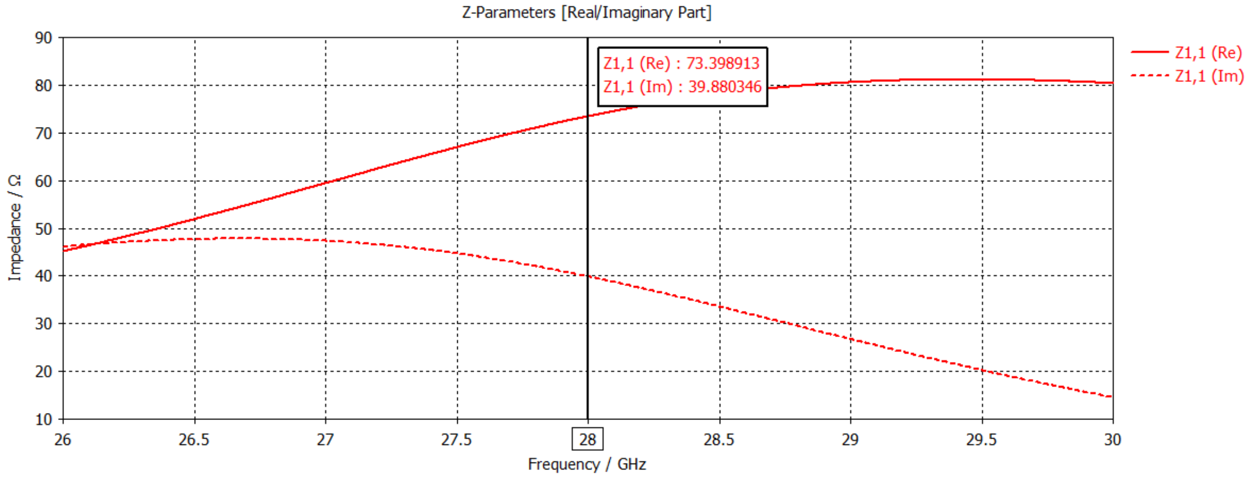

Figure 3.5: Single printed monopole: input impedance Z_{in}.

Radiation pattern and efficiency

The far field results show a realized gain on the order of 2 dBi, with radiation efficiency and total efficiency approximately equal to

$$\eta_{\mathrm{rad}} \approx 0.9916, \qquad \eta_{\mathrm{tot}} \approx 0.9240. \tag{3.12}$$

The far-field cuts validate the expected monopole behavior: being approximately omnidirectional in the azimuthal plane (H-plane) and directive in elevation (E-plane).

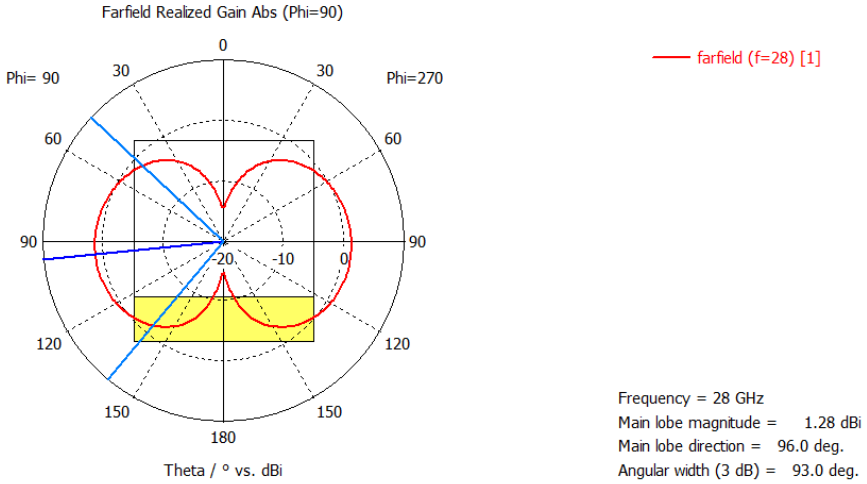

Figure 3.6: Single printed monopole: E-plane cut.

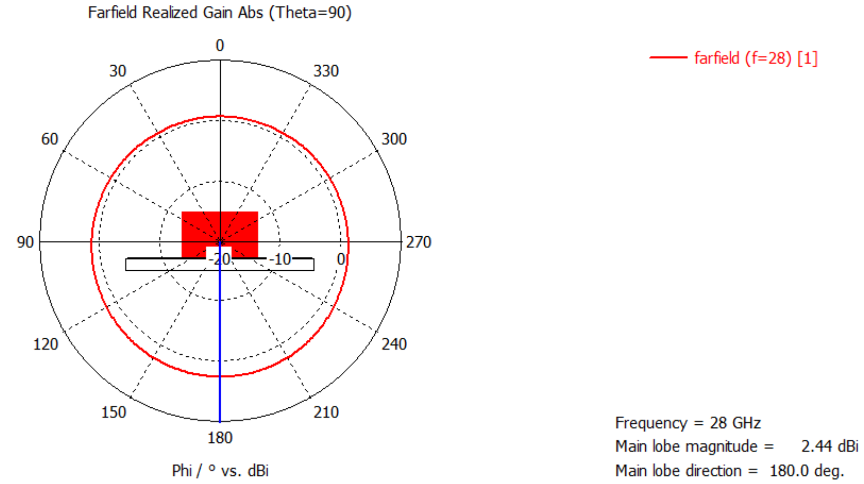

Figure 3.7: Single printed monopole: H-plane cut.

3.3 Cylindrical array

Starting from the single element previously defined, a 7-element array was done. The central element is the planar monopole of Section3.2, while the six surrounding elements were done by replicating the same planar element, placing the elements with spacing $\lambda_0/4$ (taking the center of monopoles as reference point) and finally bending the structure to obtain a ring of printed monopoles, as shown in Fig. 3.10.

3.3.1 Cylindrical layout

Substrate and metallization choice

Since the array was designed starting from the single element, the same materials and stack-up are used.

Geometry

The central element substrate dimensions are the same as in (3.4). The ring is obtained by bending the substrate after element replication and spacing as said before. Arms and feeds are identical for both the central and the ring elements:

$$L_{\text{arm}} = 2.27 \text{ mm}, \qquad W_{\text{arm}} = 0.67 \text{ mm}, \tag{3.13}$$

$$L_{\text{feed}} = 1.00 \text{ mm}, \qquad W_{\text{feed}} = 0.28 \text{ mm}. \tag{3.14}$$

A waveguide port was used for the central element, while discrete ports were adopted for the first ring, because in CST it was not possible to define a curved waveguide port on the bent ring of parasititcs.

3.3.2 Cylindrical layout results

S_{11}

The reflection coefficient at the central port degrades compared to the isolated element, consistently with the expected impact of mutual coupling and common ground currents in a dense configuration:

$$S_{11}(28 \text{ GHz}) \approx -6.14 \text{ dB}. \tag{3.15}$$

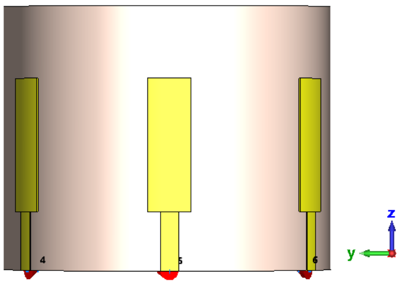

Figure 3.8: Cylindrical array: lateral view.

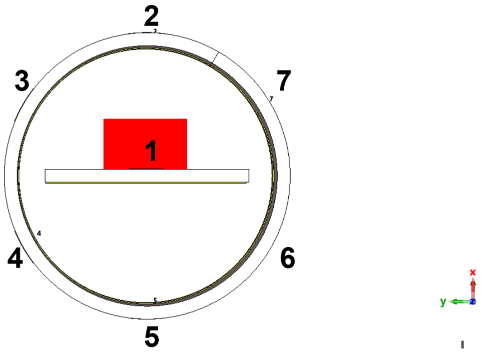

Figure 3.9: Cylindrical array: top view.

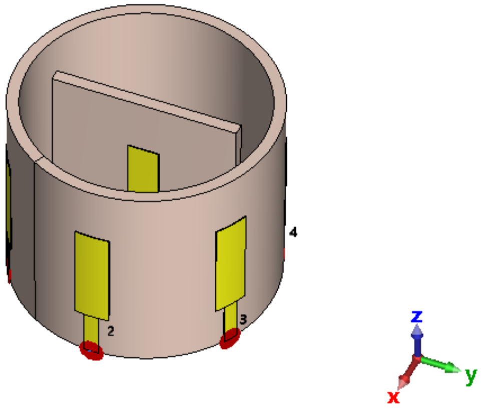

Figure 3.10: Cylindrical array: perspective view.

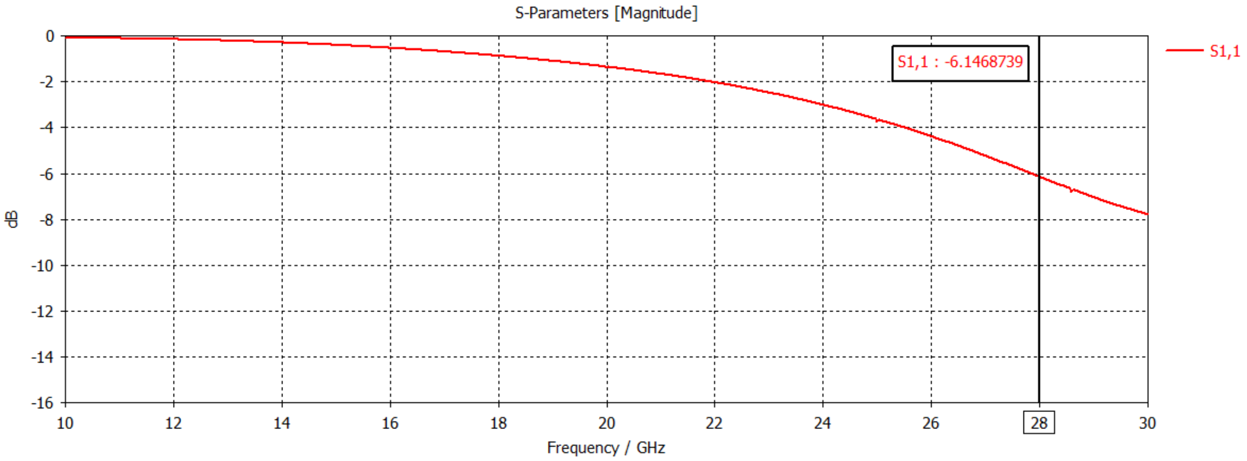

Figure 3.11: Cylindrical array: S_{11} at the central port.

S_{ij}

The transmission coefficients quantify the coupling between ports and gives a n indicator of the electromagnetic interaction among elements.

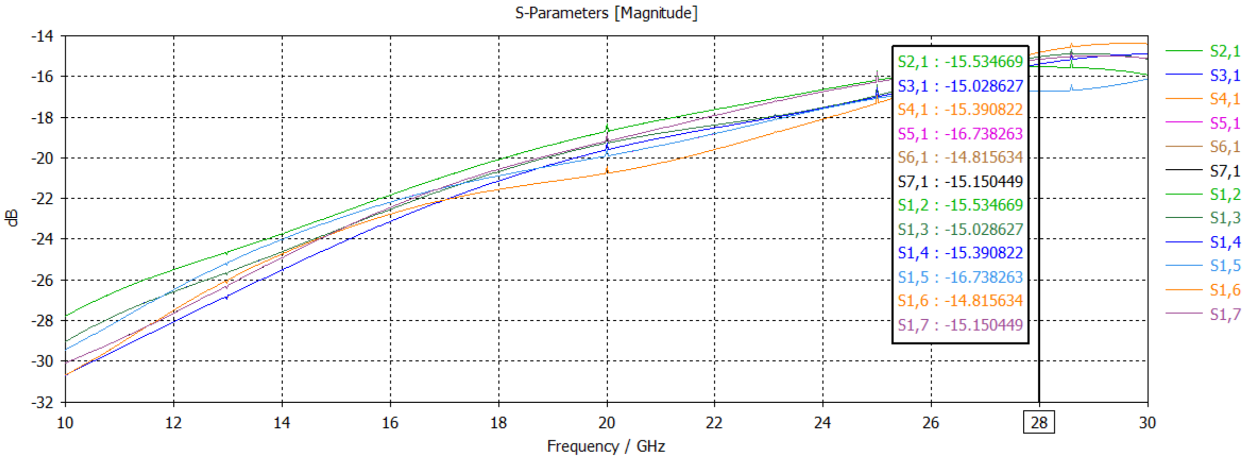

Figure 3.12: Cylindrical array: S_{ij}.

Radiation pattern and efficiency

For this configuration, the realized gain is 1.5dBi, with radiation efficiency and total efficiency approximately equal to

$$\eta_{\text{rad}} \approx 0.97, \qquad \eta_{\text{tot}} \approx 0.57. \tag{3.16}$$

Far-field cuts for each excitations are reported below. In particular, for the central element the H-plane is no longer omnidirectional. This is consistent with the behavior already observed for the single element in Fig. 3.7 and is accentuated by the presence of the surrounding elements.

1. **Central element fed**:

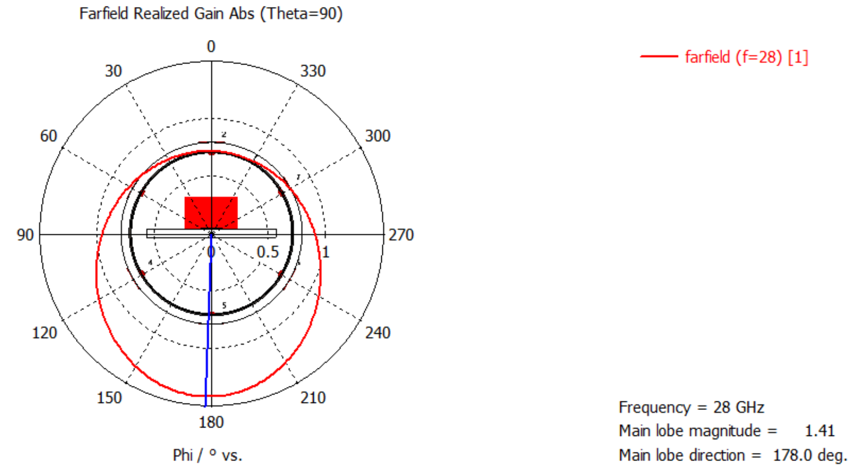

Figure 3.13: Cylindrical array: central element, H-plane cut.

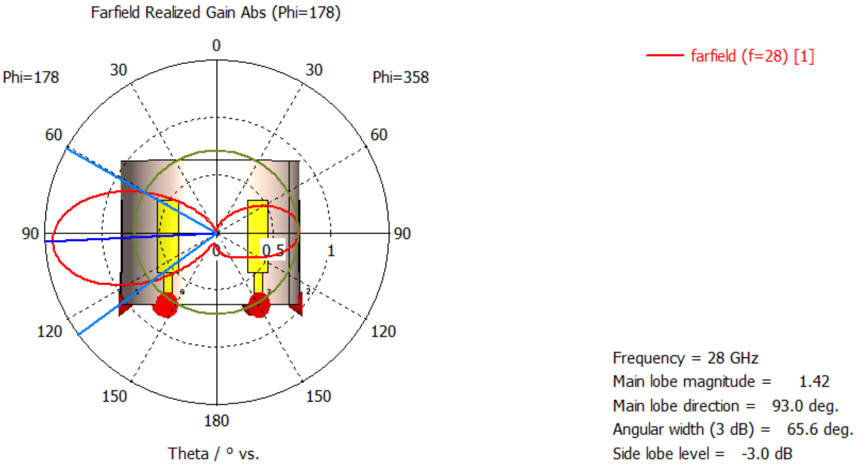

Figure 3.14: Cylindrical array: central element, E-plane cut.

2. **Second element fed**:

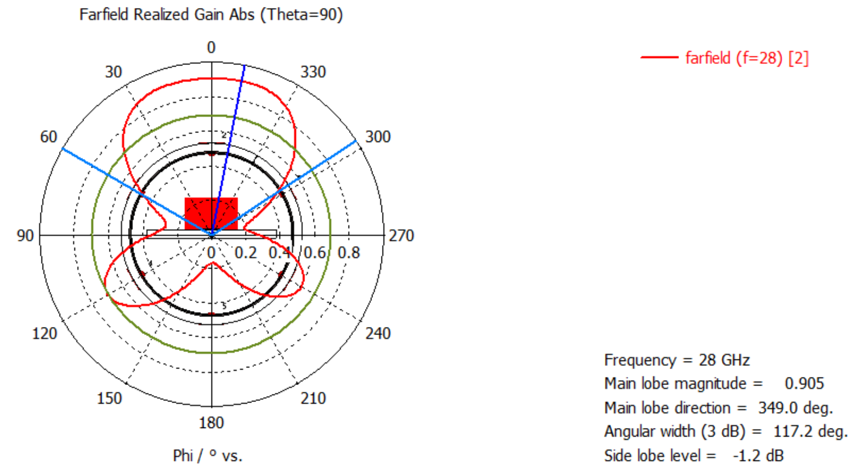

Figure 3.15: Cylindrical array: second element, H-plane cut.

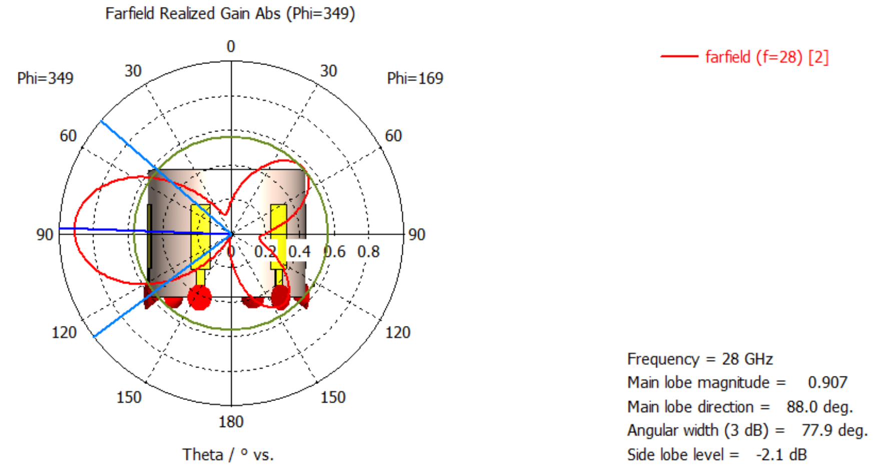

Figure 3.16: Cylindrical array: second element, E-plane cut.

3. **Third element fed**:

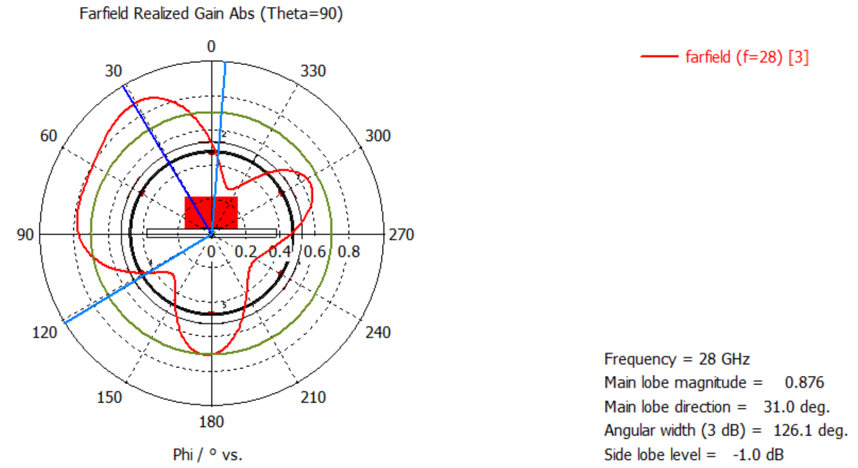

Figure 3.17: Cylindrical array: third element, H-plane cut.

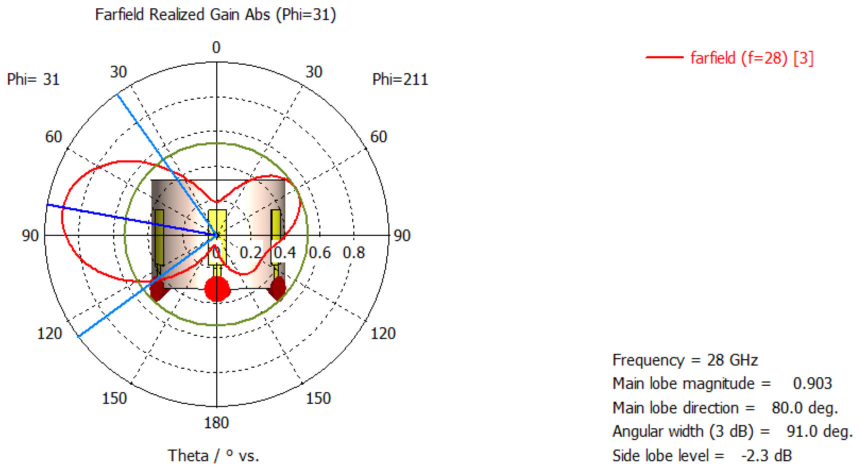

Figure 3.18: Cylindrical array: third element, E-plane cut.

4. **Fourth element fed**:

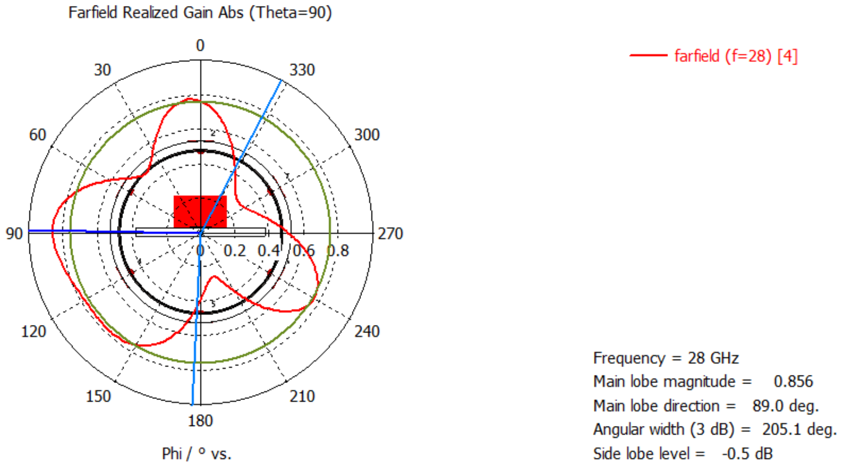

Figure 3.19: Cylindrical array: fourth element, H-plane cut.

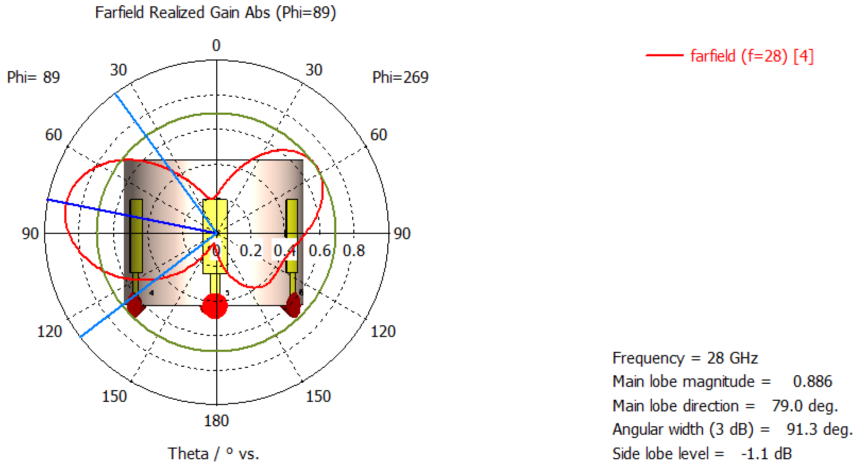

Figure 3.20: Cylindrical array: fourth element, E-plane cut.

5. **Fifth element fed**:

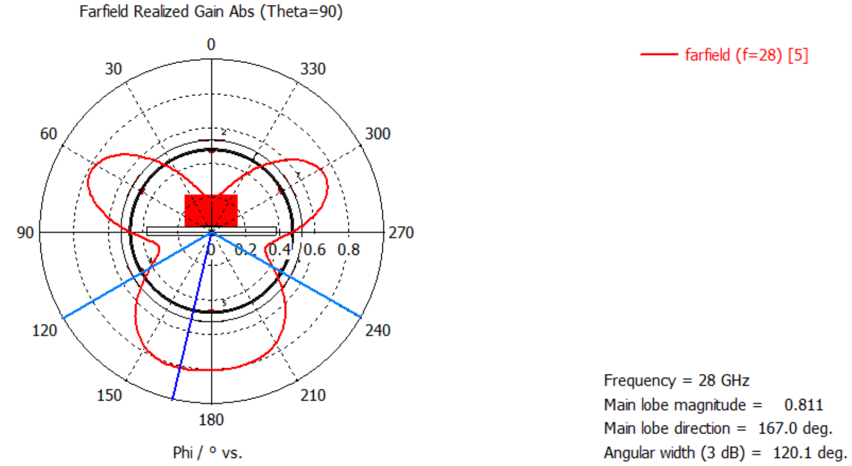

Figure 3.21: Cylindrical array: fifth element, H-plane cut.

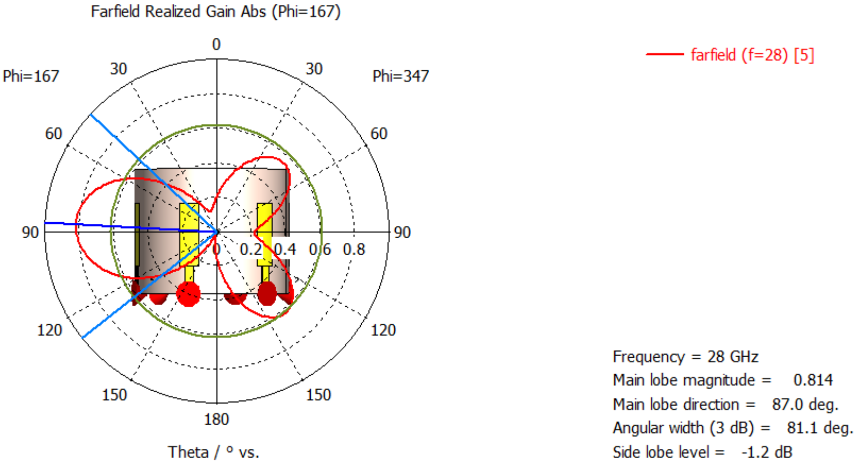

Figure 3.22: Cylindrical array: fifth element, E-plane cut.

6. **Sixth element fed**:

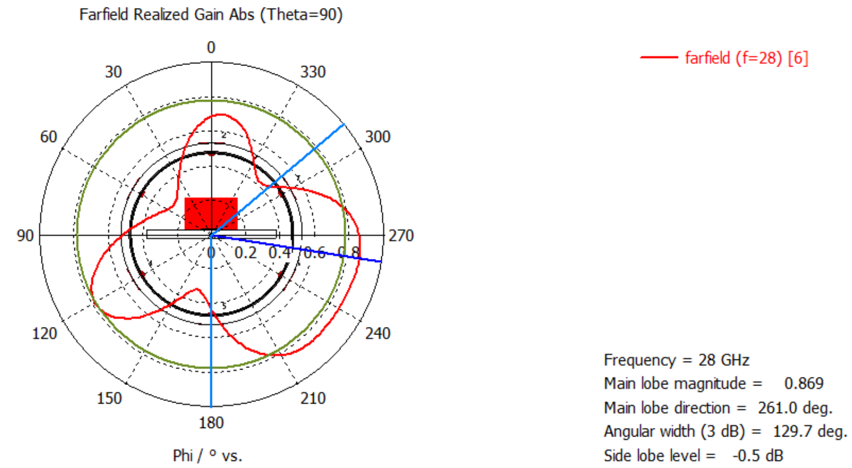

Figure 3.23: Cylindrical array: sixth element, H-plane cut.

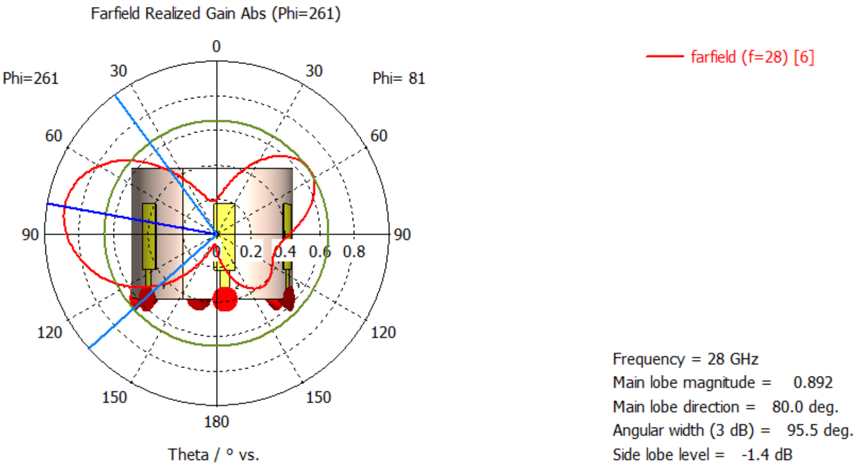

Figure 3.24: Cylindrical array: sixth element, E-plane cut.

7. **Seventh element fed**:

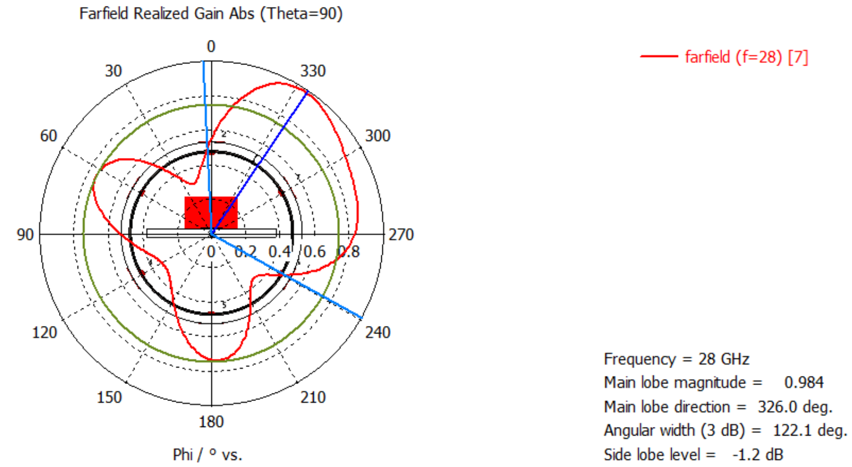

Figure 3.25: Cylindrical array: seventh element, H-plane cut.

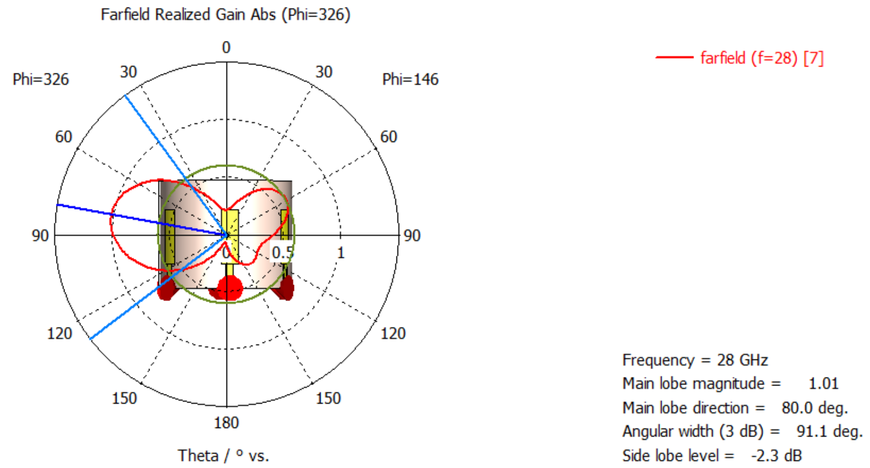

Figure 3.26: Cylindrical array: seventh element, E-plane cut.

From these results, the field has a maximum in correspondence of the excited port (see Fig. 3.9); however, sidelobes are still too high (with an average of $-1dB$). Moreover, as said before, different port types were used for the central and ring elements. To have a more reliable simulation, a new structure with uniform waveguide ports was investigated.

3.4 Hexagonal array

Starting from the central element, the first ring was done as a planar hexagon, because the planar nature of the hexagon faces allows to define waveguide ports also for the parasitic elements of the DSA in the full-wave simulator

3.4.1 Hexagonal layout

Geometry

The geometry differs not only in the shape of the first ring, but also in the single element dimensions becauser an optimization was performed to improve the central port impedance and reflection coefficient. All elements are still at a distance $\lambda_0/4$. The substrate dimensions for the central element are:

$$L_{\text{sub}} = 4.0 \text{ mm}, \qquad W_{\text{sub}} = 2.77 \text{ mm}. \tag{3.17}$$

For the arm, feed line, and ground, the values obtained for all monopoles are

$$L_{\text{arm}} = 2.78 \text{ mm}, \qquad W_{\text{arm}} = 1.30 \text{ mm}, \tag{3.18}$$

$$L_{\text{feed}} = L_{\text{gnd}} = 0.34 \text{ mm}, \qquad W_{\text{feed}} = 0.28 \text{ mm}. \tag{3.19}$$

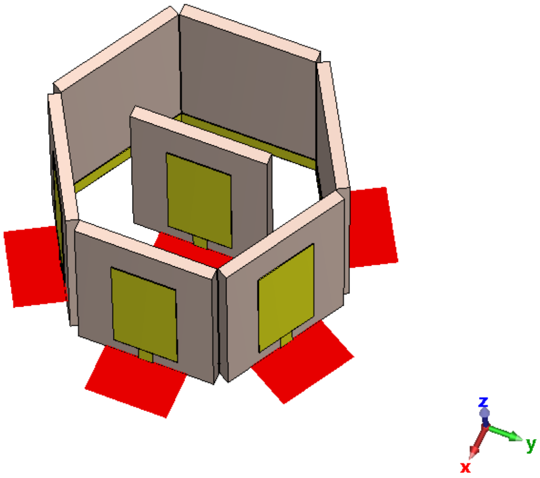

Figure 3.27: Hexagonal array: perspective view.

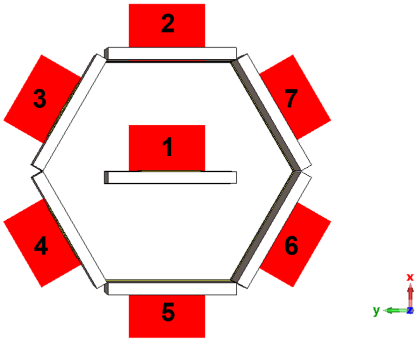

Figure 3.28: Hexagonal array: top view.

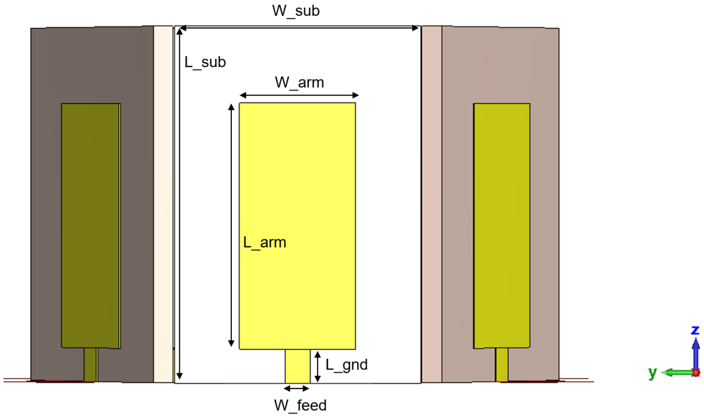

Figure 3.29: Hexagonal array: lateral view.

3.4.2 Hexagonal layout results

S_{11}

The reflection coefficient improves with respect to the cylindrical structure, but it remains above -10 dB:

$$S_{11}(28\text{ GHz}) \approx -8.9\text{ dB}. \tag{3.20}$$

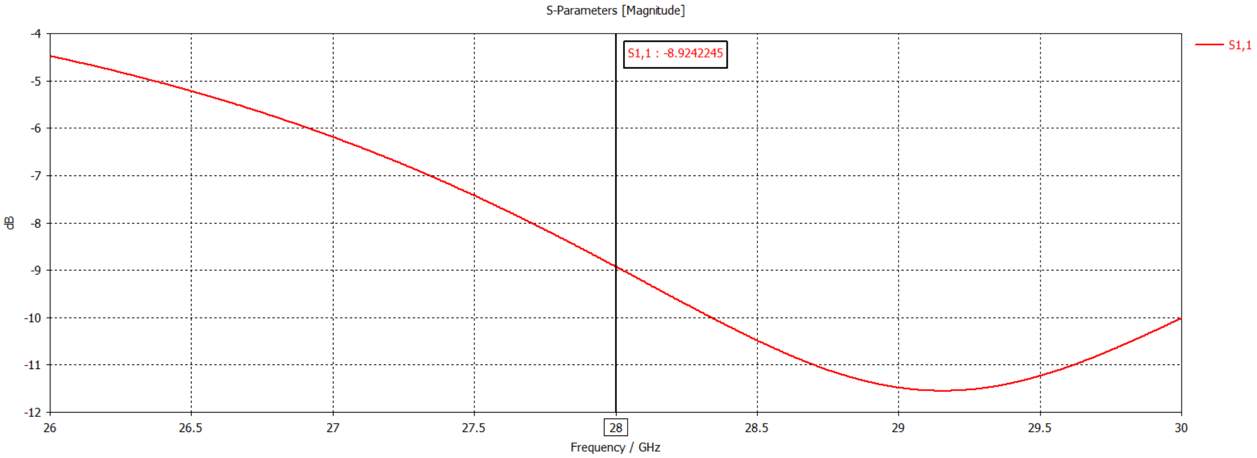

Figure 3.30: Hexagonal array: S_{11} at the central port.

S_{ij}

The S_{ij} show an improved coupling with respect to the previous case, having an average value of $-12dB$

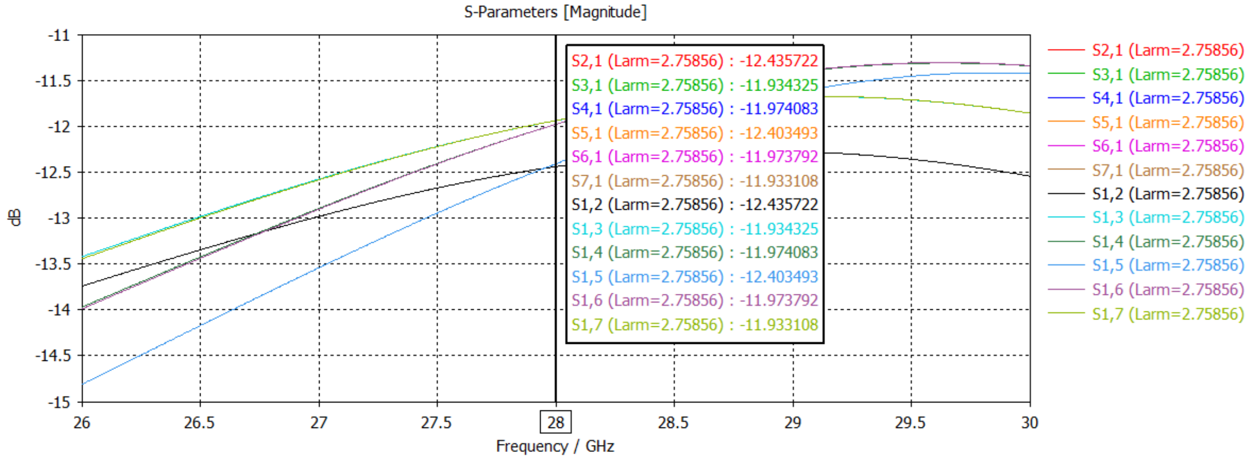

Figure 3.31: Hexagonal array: S_{ij}.

Radiation pattern and efficiency

In this case, the realized gain is 1.6 dBi, with radiation efficiency and total efficiency approximately equal to

$$\eta_{\text{rad}} \approx 0.98, \qquad \eta_{\text{tot}} \approx 0.49. \tag{3.21}$$

The far-field cuts for the same set of excitations as in the cylindrical structure are reported. The central element still presents a non omnidirectionale azimuthal radiation pattern.

1. **Central element fed**:

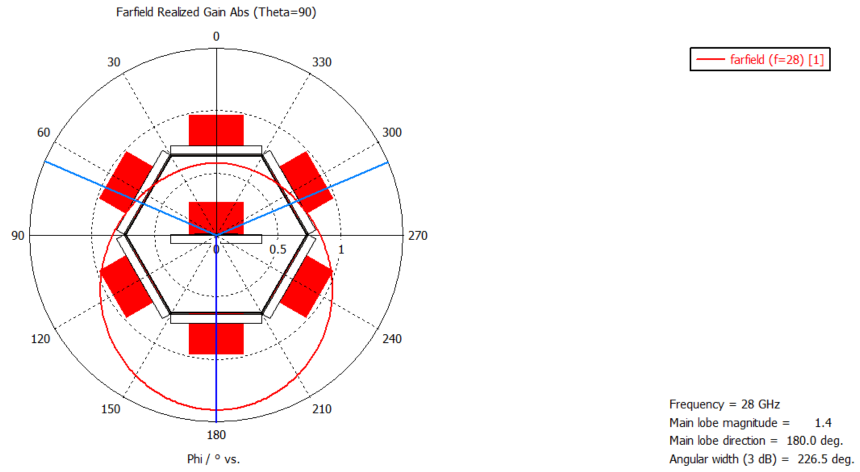

Figure 3.32: Hexagonal array: central element, H-plane cut.

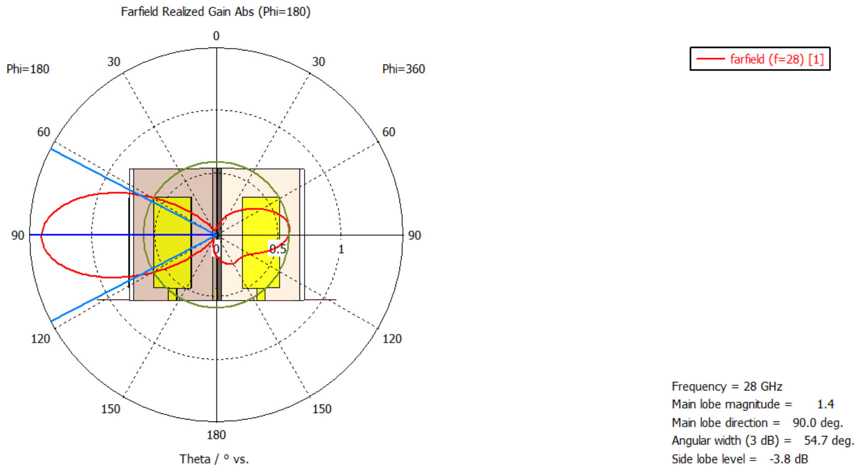

Figure 3.33: Hexagonal array: central element, E-plane cut.

2. **Second element fed**:

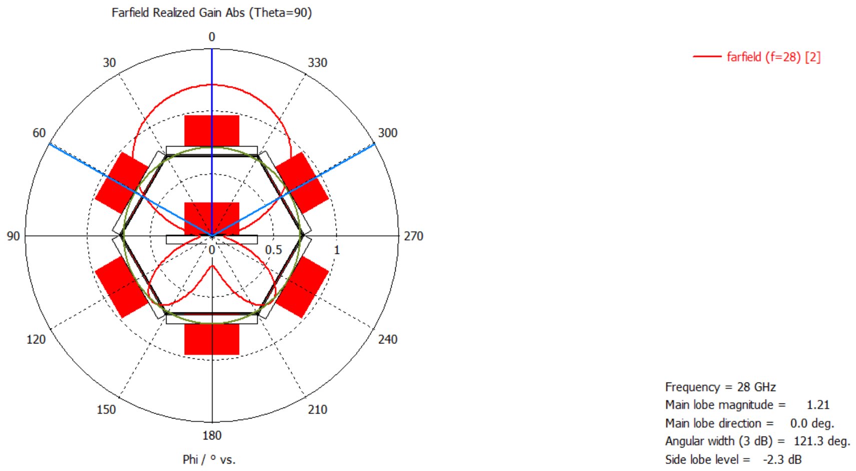

Figure 3.34: Hexagonal array: second element, H-plane cut.

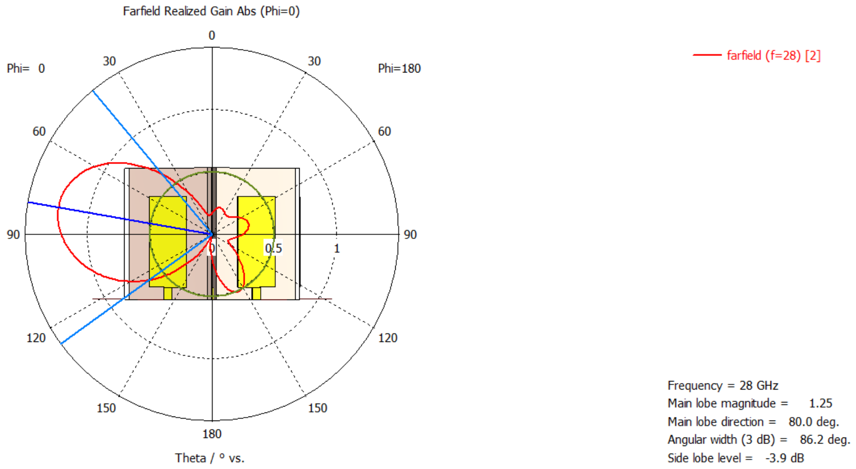

Figure 3.35: Hexagonal array: second element, E-plane cut.

3. **Third element fed**:

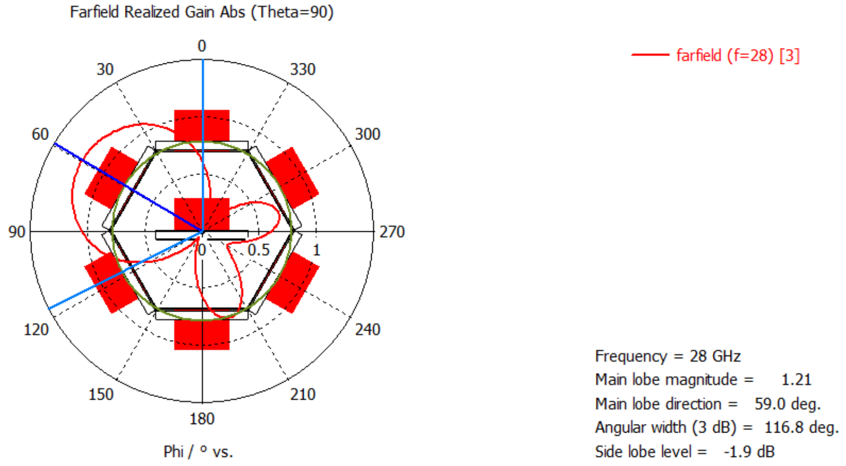

Figure 3.36: Hexagonal array: third element, H-plane cut.

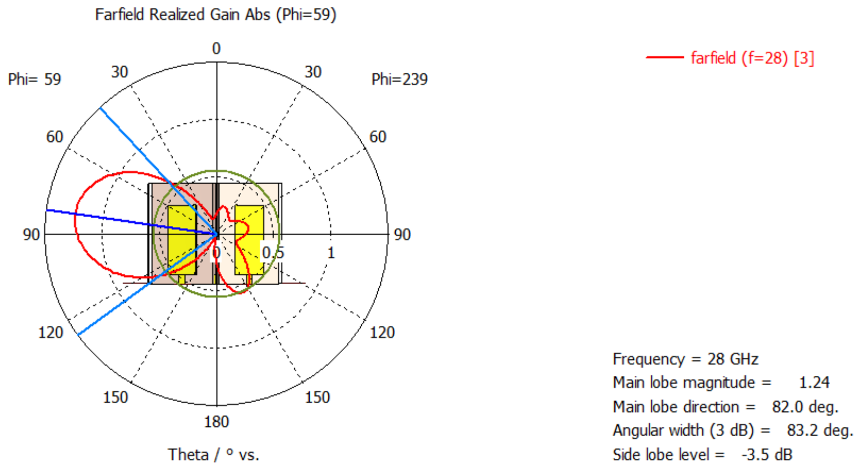

Figure 3.37: Hexagonal array: third element, E-plane cut.

4. **Fourth element fed**:

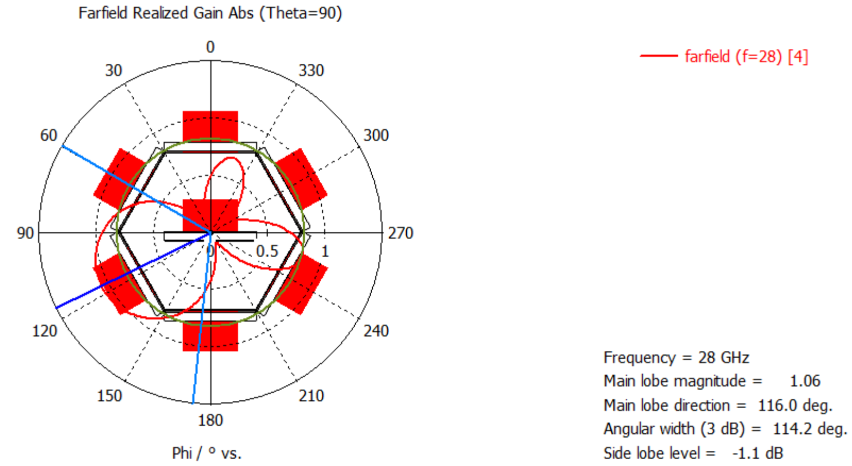

Figure 3.38: Hexagonal array: fourth element, H-plane cut.

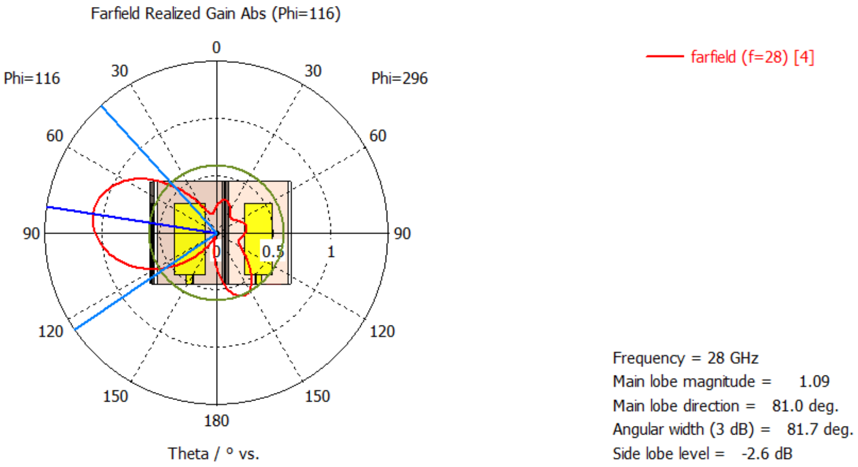

Figure 3.39: Hexagonal array: fourth element, E-plane cut.

5. **Fifth element fed**:

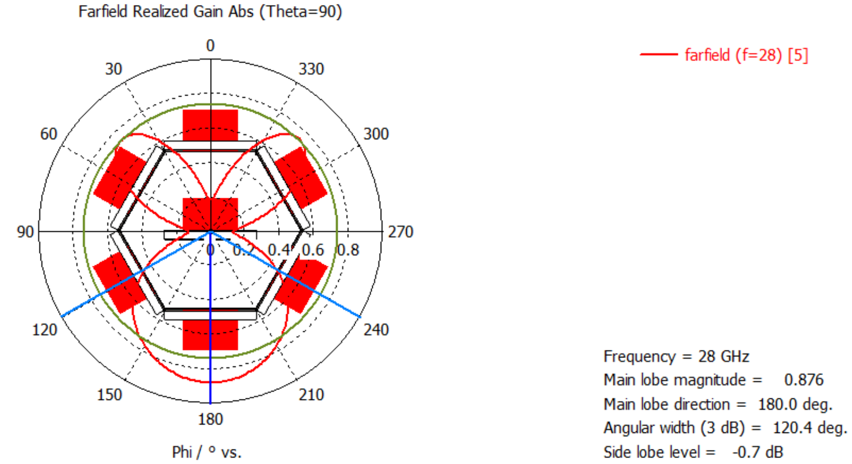

Figure 3.40: Hexagonal array: fifth element, H-plane cut.

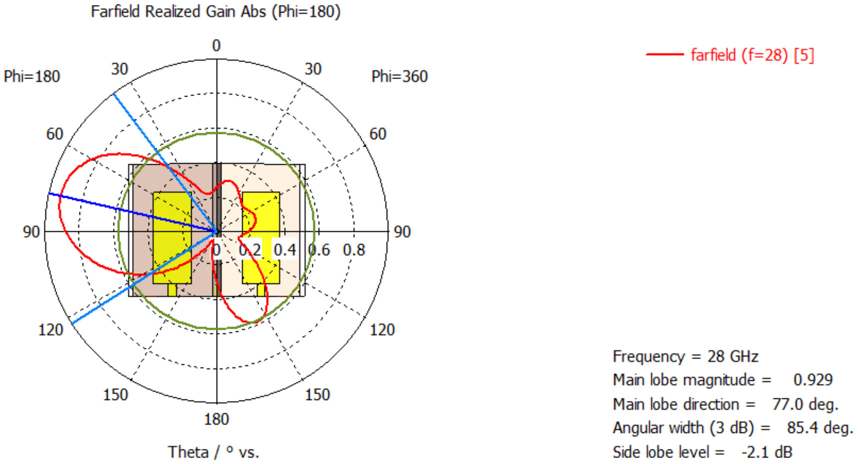

Figure 3.41: Hexagonal array: fifth element, E-plane cut.

6. **Sixth element fed**:

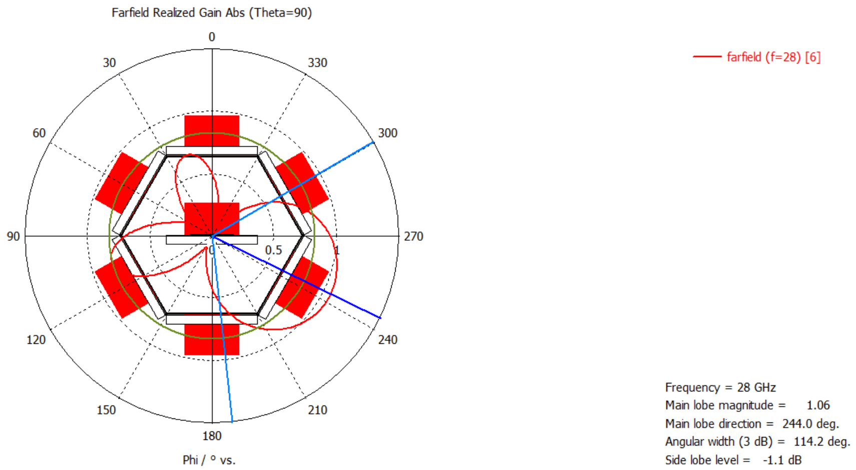

Frequency = 28 GHz
Main lobe magnitude = 1.06
Main lobe direction = 244.0 deg.
Angular width (3 dB) = 114.2 deg.
Side lobe level = -1.1 dB

Figure 3.42: Hexagonal array: sixth element, H-plane cut.

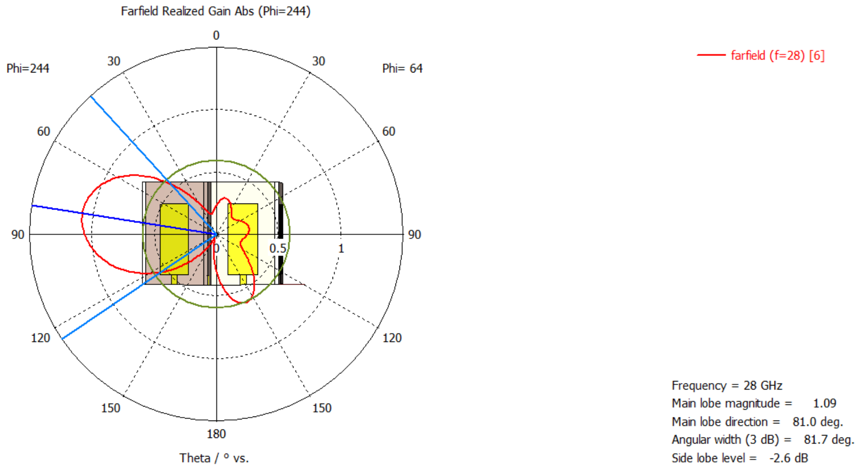

Frequency = 28 GHz
Main lobe magnitude = 1.09
Main lobe direction = 81.0 deg.
Angular width (3 dB) = 81.7 deg.
Side lobe level = -2.6 dB

Figure 3.43: Hexagonal array: sixth element, E-plane cut.

7. **Seventh element fed**:

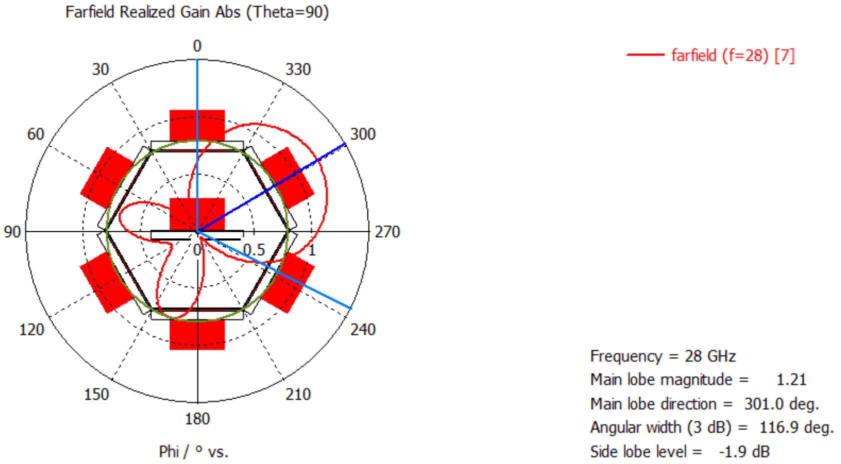

Frequency = 28 GHz
Main lobe magnitude = 1.21
Main lobe direction = 301.0 deg.
Angular width (3 dB) = 116.9 deg.
Side lobe level = -1.9 dB

Figure 3.44: Hexagonal array: seventh element, H-plane cut.

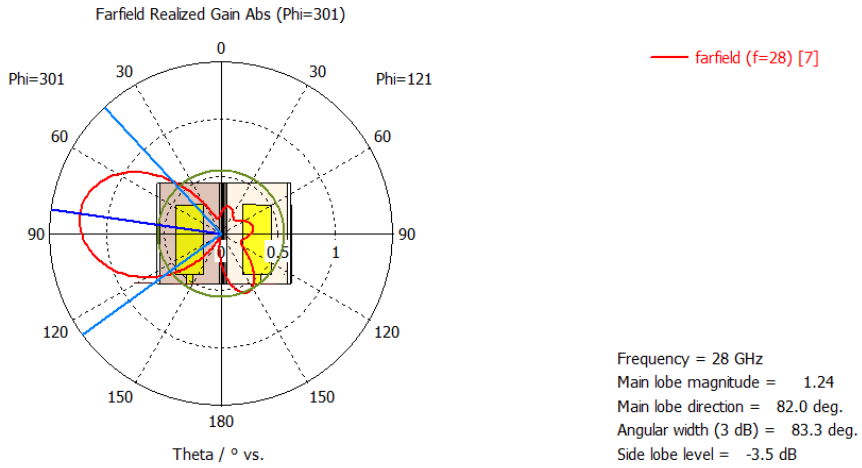

Figure 3.45: Hexagonal array: seventh element, E-plane cut.

Radiation patterns comparison

An overall improvement with respect to the cylindrical structure is observed, mainly due to the optimization and to the use of the same port type for each element. The effect of the ground plane is reduced since its dimension was more than halved with respect to the cylindrical case. However, such a small ground plane is not practical for a physical implementation where SMA connectors and varactorsr must be integrated. Moreover, the microstrip form factor becomes critical since the required width to obtain $Z_{\text{line}} \approx 73\ \Omega$ is $W_{\text{feed}} = 0.28$ mm, while the required length is $L_{\text{feed}} = 0.34$ mm. Another aspect to observe is that the SSL has not improved sufficiently as can be observed for example in 3.40.

3.5 Decoupling

In order to better understand the interaction between planar monopoles, a decoupling network was done to separate the ground plane for each element and reduce coupling between adjacent elements.

3.5.1 Two monopoles without decoupling network

Two planar monopoles were placed side by side with distance $\lambda_0/4$ between them. The overall structure dimensions were optimized to obtain $S_{11} < -10$ dB and $Z_{\text{in}} = 73 + j42\ \Omega$.

Geometry

The optimized substrate dimensions are

$$L_{\text{sub}} = 4.5 \text{ mm}, \qquad W_{\text{sub}} = 6.0 \text{ mm}. \tag{3.22}$$

The arm, feed line and ground are

$$L_{\text{arm}} = 2.1 \text{ mm}, \qquad W_{\text{arm}} = 0.34 \text{ mm}, \tag{3.23}$$

$$L_{\text{feed}} = L_{\text{gnd}} = 1.38 \text{ mm}, \qquad W_{\text{feed}} = 0.28 \text{ mm}. \tag{3.24}$$

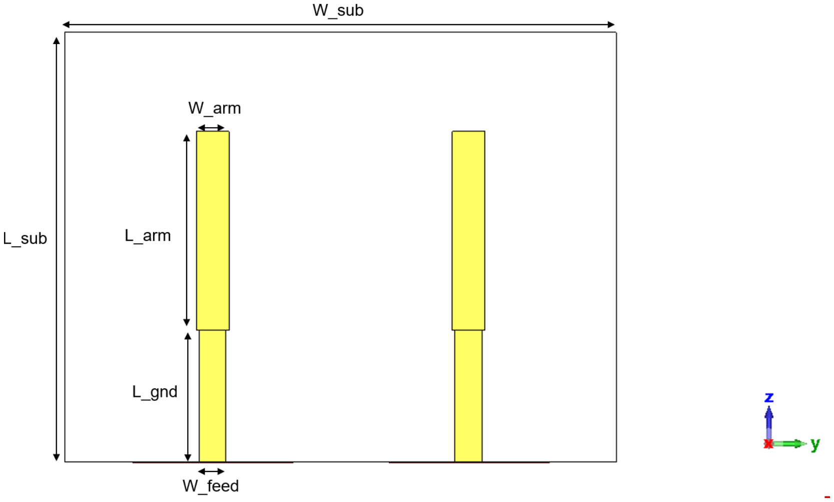

Figure 3.46: Two monopoles without decoupling: front view.

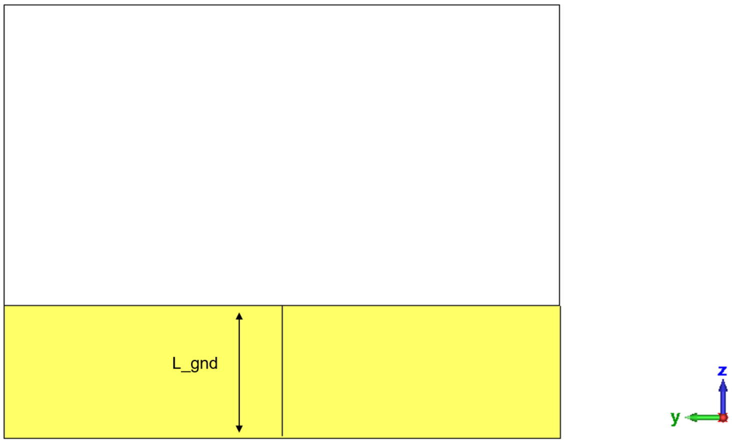

Figure 3.47: Two monopoles without decoupling: back view.

Results

- S_{ii}:

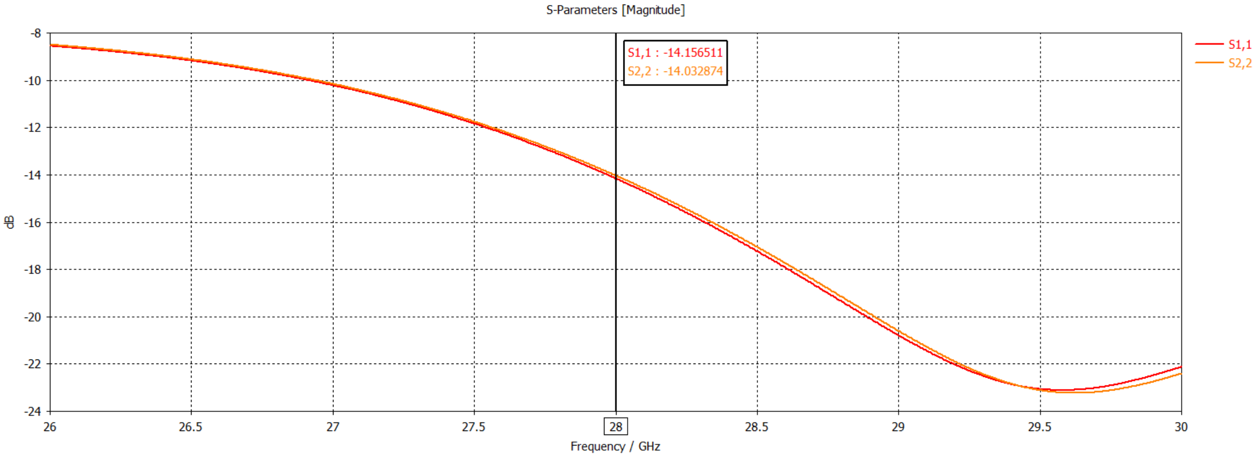

Figure 3.48: Two monopoles without decoupling: S_{ii}.

The reflection coefficient at both ports is ok with the desired target.

- S_{ij}:

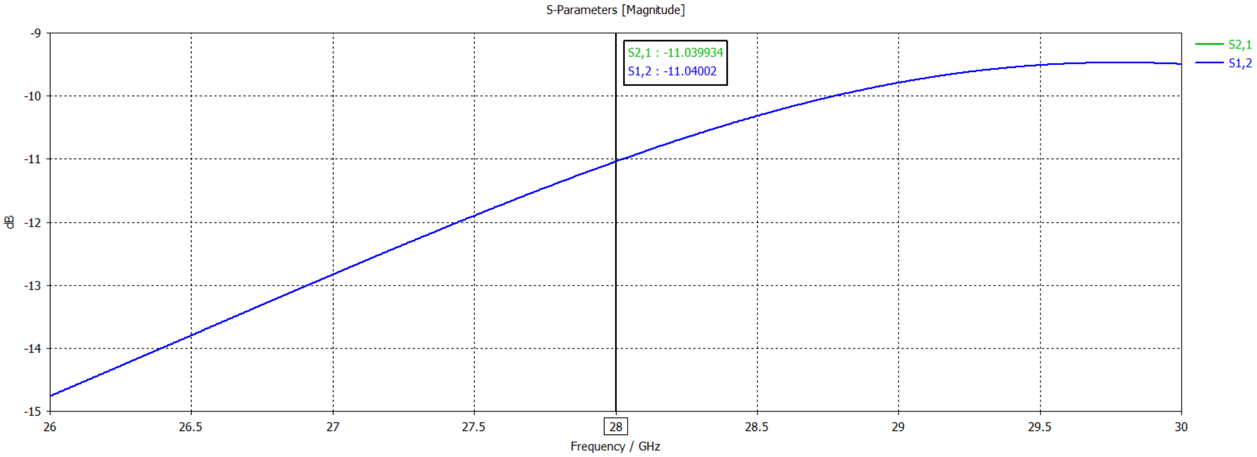

Figure 3.49: Two monopoles without decoupling: S_{ij}.

The value $S_{ij}(28 \text{ GHz}) \approx -11$ dB indicates coupling. This is also visible by watching the surface currents in Fig. 3.51.

- Z_{ii}:

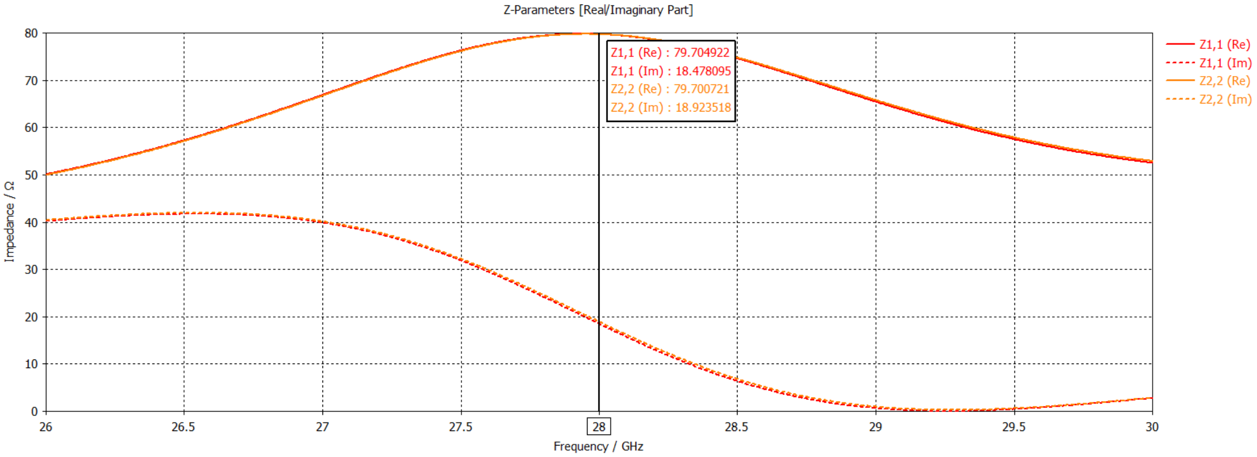

Figure 3.50: Two monopoles without decoupling: Z_{ii}.

The obtained $Z_{ii}(28\text{ GHz}) \approx 80 + j20\ \Omega$ is close to the desired value.

- **Surface currents:**

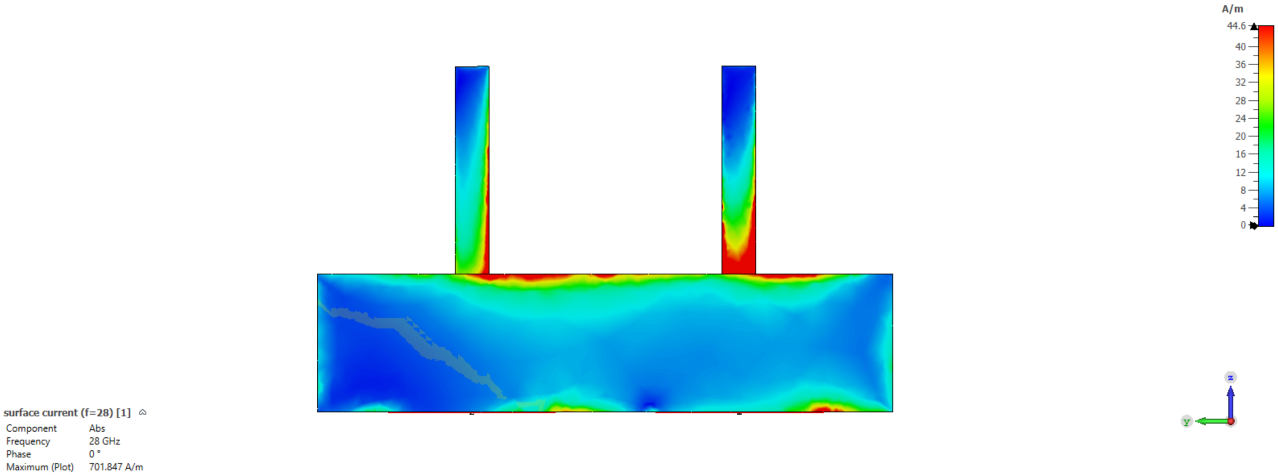

Figure 3.51: Two monopoles without decoupling: surface currents (port 1 excited).

When monopole 1 (right) is excited, part of the current leaks to the other monopole and onto the ground plane.

- **Radiation diagrams:**

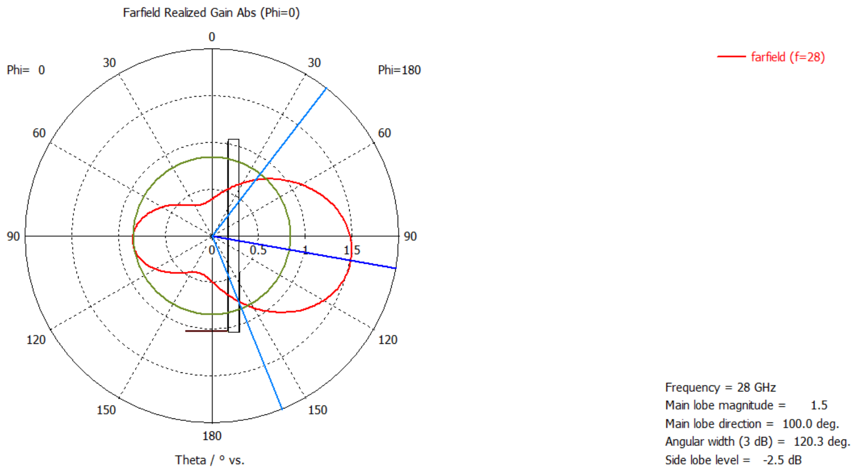

Frequency = 28 GHz
Main lobe magnitude = 1.5
Main lobe direction = 100.0 deg.
Angular width (3 dB) = 120.3 deg.
Side lobe level = -2.5 dB

Figure 3.52: Two monopoles without decoupling: E-plane cut (port 1 excited).

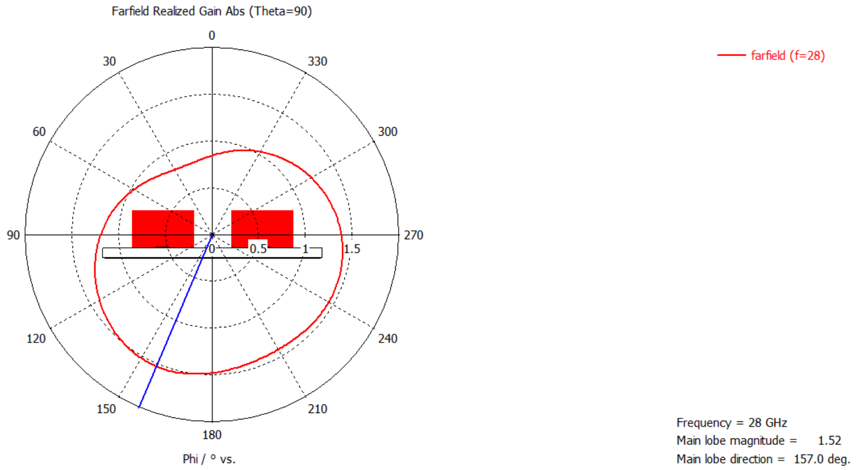

Frequency = 28 GHz
Main lobe magnitude = 1.52
Main lobe direction = 157.0 deg.

Figure 3.53: Two monopoles without decoupling: H-plane cut (port 1 excited).

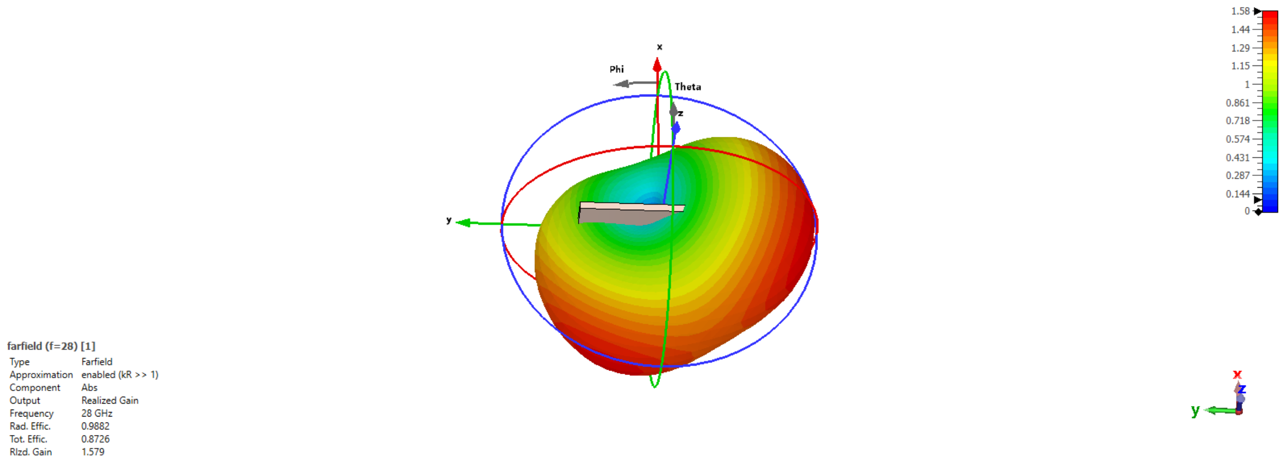

farfield (f=28) [1]

Type	Farfield
Approximation	enabled (kR >> 1)
Component	Abs
Output	Realized Gain
Frequency	28 GHz
Rad. Effic.	0.9882
Tot. Effic.	0.8726
Rlzd. Gain	1.579

Figure 3.54: Two monopoles without decoupling: 3D pattern (port 1 excited).

Both in the E-plane and H-plane a back maximum is observed. Only the case with port 1 excited is reported, since the case with port 2 excited is specular.

3.5.2 Two monopoles with decoupling network

The two monopoles are the same as in Section 3.5.1, but a decoupling network is introduced by doing five slots in the ground plane.

Geometry

The front view is the same ad before, while the back view includes the decoupling network obtained by five slots in the ground plane:

$$L_{\text{gnd}} = 1.38 \text{ mm}, \qquad W_{\text{slot}} = 0.1 \text{ mm}. \tag{3.25}$$

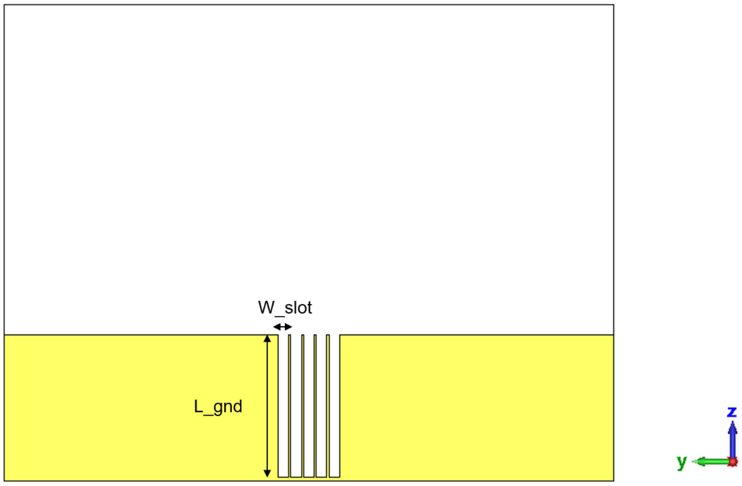

Figure 3.55: Two monopoles with decoupling: back view (slotting).

Results

- S_{ii}:

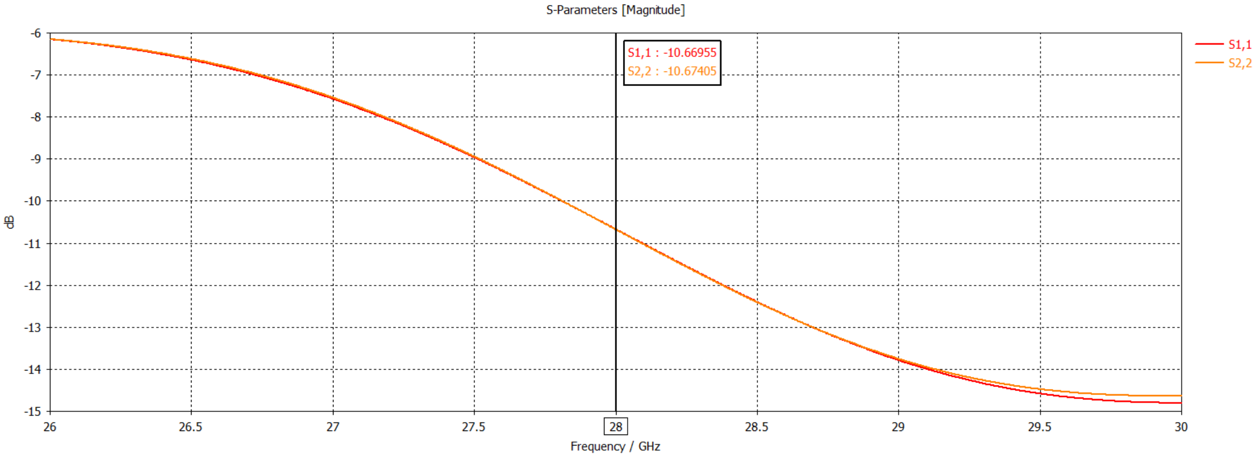

Figure 3.56: Two monopoles with decoupling: S_{ii}.

The reflection coefficient at both ports meets the desired target.

- S_{ij}:

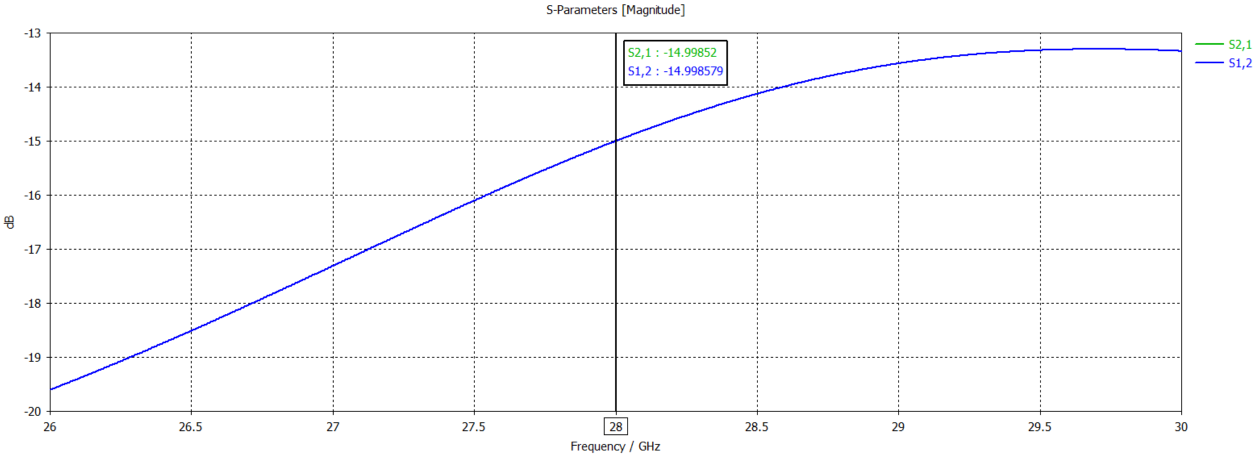

Figure 3.57: Two monopoles with decoupling: S_{ij}.

The value $S_{ij}(28\text{ GHz}) \approx -15$ dB indicates improved isolation with respect to the case without decoupling, which is also visible in the surface currents.

- Z_{ii}:

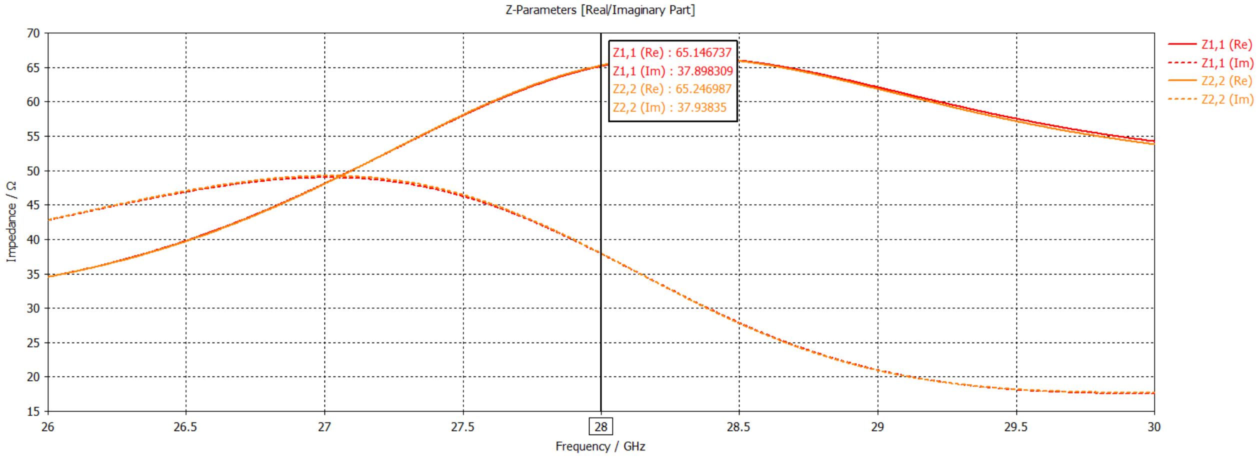

Figure 3.58: Two monopoles with decoupling: Z_{ii}.

The obtained $Z_{ii}(28\text{ GHz}) \approx 65 + j40\ \Omega$ is close to the desired value.

- **Surface currents:**

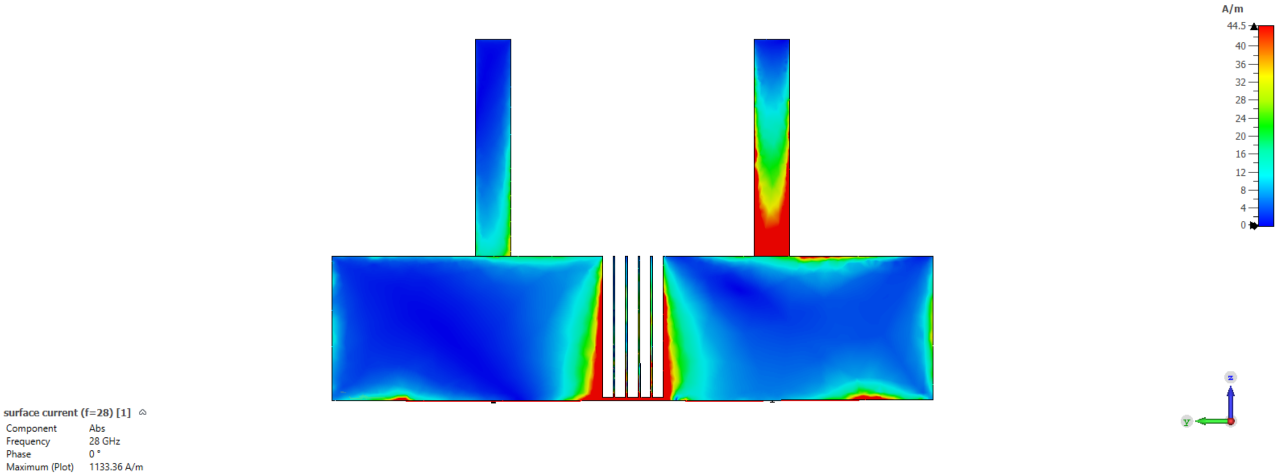

Figure 3.59: Two monopoles with decoupling: surface currents (port 1 excited).

Using the same scale as in the case without the decoupling network, the current is more confined around the slots, reducing leakage towards the adjacent element.

- **Radiation diagrams:**

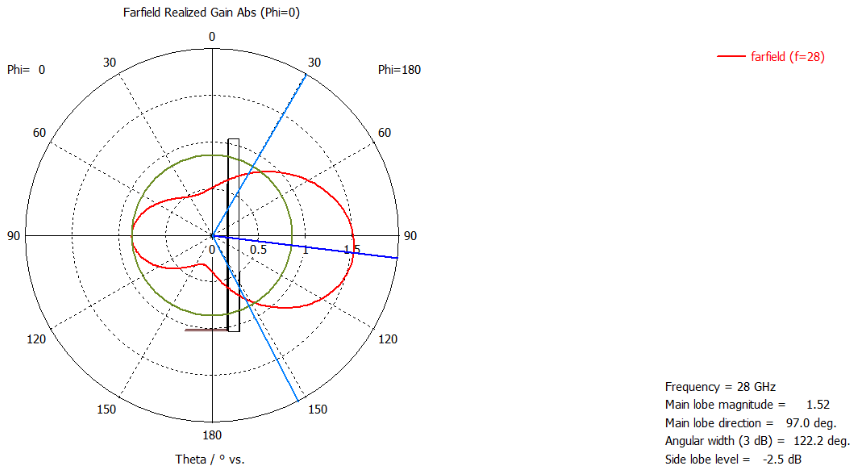

Figure 3.60: Two monopoles with decoupling: E-plane cut (port 1 excited).

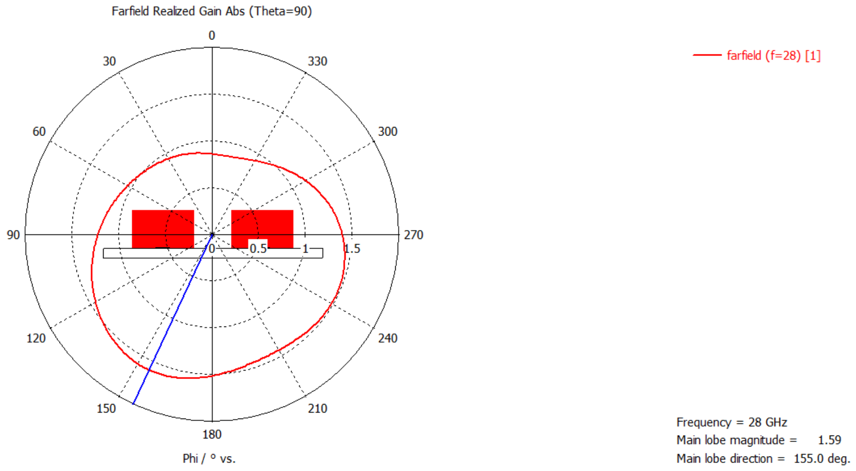

Figure 3.61: Two monopoles with decoupling: H-plane cut (port 1 excited).

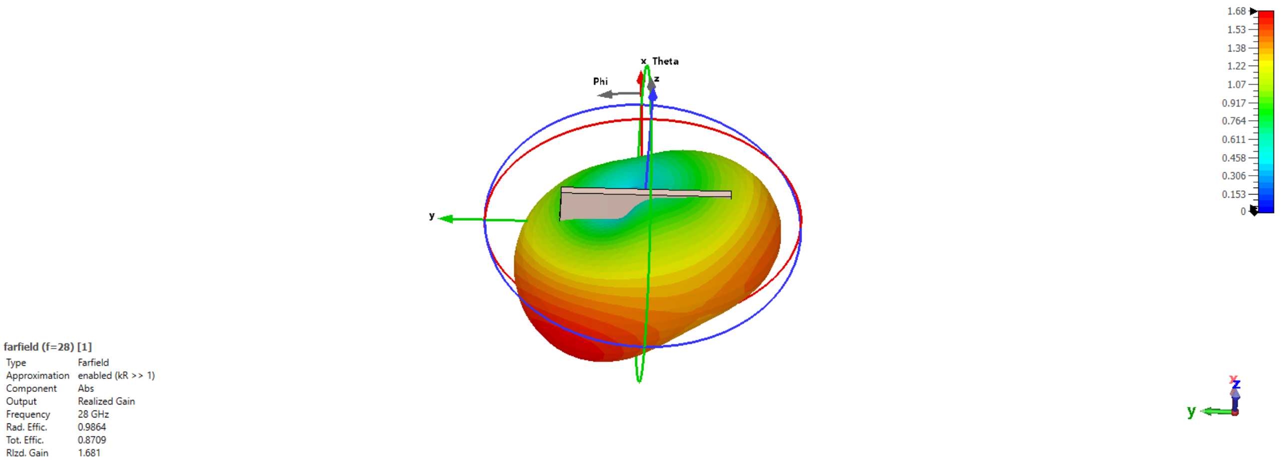

Figure 3.62: Two monopoles with decoupling: 3D pattern (port 1 excited).

As in the previous case, the radiation has a back maximum; however, the back maximum is attenuated, indicating that the decoupling network reduces the undesired current. The introduction of a decoupling network appears beneficial to isolate adjacent elements; By the way, the ground plane still plays an active role in radiation and remains a critical factor at 28 GHz.

3.6 The ground plane's effect in planar technology

In order to isolate the effect of the ground plane, a comparison between an ideal case with PEC dipoles of total length $\lambda_0/2$, and two planar monopoles with a realistic finite ground plane was performed. In both cases, the distance between the two elements is $\lambda_0/4$.

3.6.1 Layout

Ideal dipoles

The top and front views of the two dipoles are reported in Fig. 3.63–3.64.

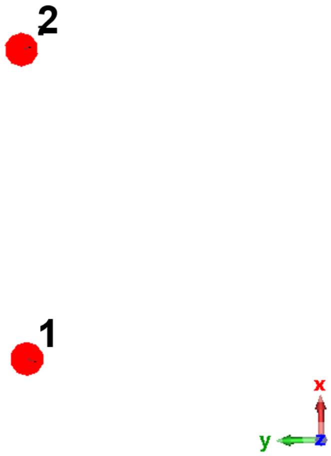

Figure 3.63: Ideal dipoles: top view.

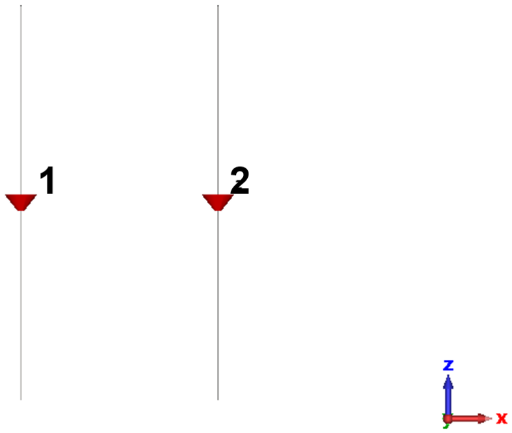

Figure 3.64: Ideal dipoles: front view.

Monopoles side by side

The two monopoles considered here are not the same as in the previous sections; they were obtained through a further optimization. The substrate dimensions are

$$L_{\text{sub}} = 4.5 \text{ mm}, \qquad W_{\text{sub}} = 3.09 \text{ mm}. \tag{3.26}$$

The arm, feed line and ground are

$$L_{\text{arm}} = 2.08 \text{ mm}, \qquad W_{\text{arm}} = 0.34 \text{ mm}, \tag{3.27}$$

$$L_{\text{feed}} = L_{\text{gnd}} = 1.38 \text{ mm}, \qquad W_{\text{feed}} = 0.28 \text{ mm}. \tag{3.28}$$

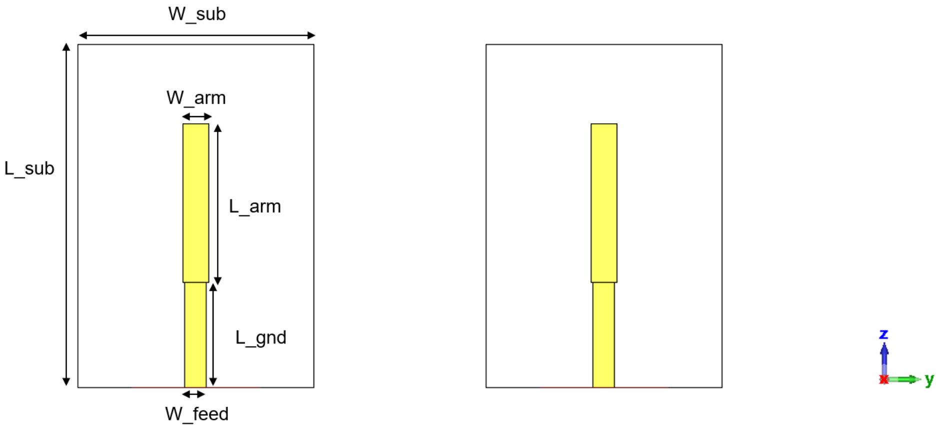

Figure 3.65: Planar monopoles: front view.

Figure 3.66: Planar monopoles: back view.

3.6.2 Radiation diagrams comparison

The comparison is performed on the H-plane, since no relevant differences were observed on the E-plane.

Ideal dipoles radiation diagrams

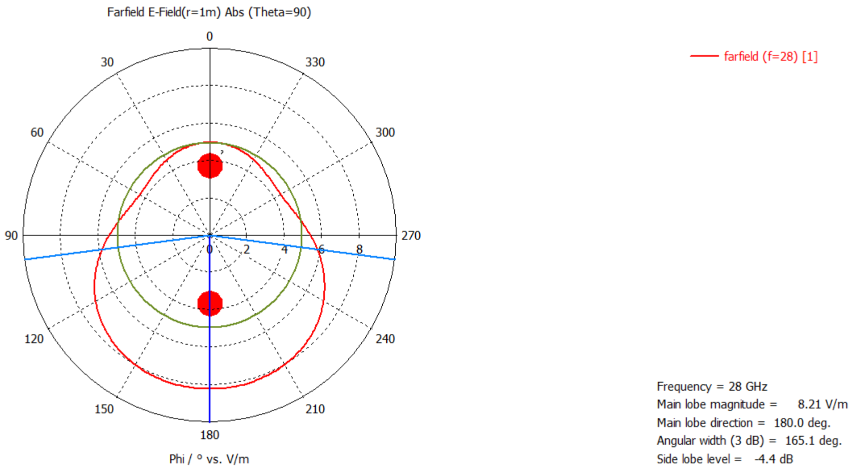

Figure 3.67: Ideal dipoles: H-plane, element 1 excited.

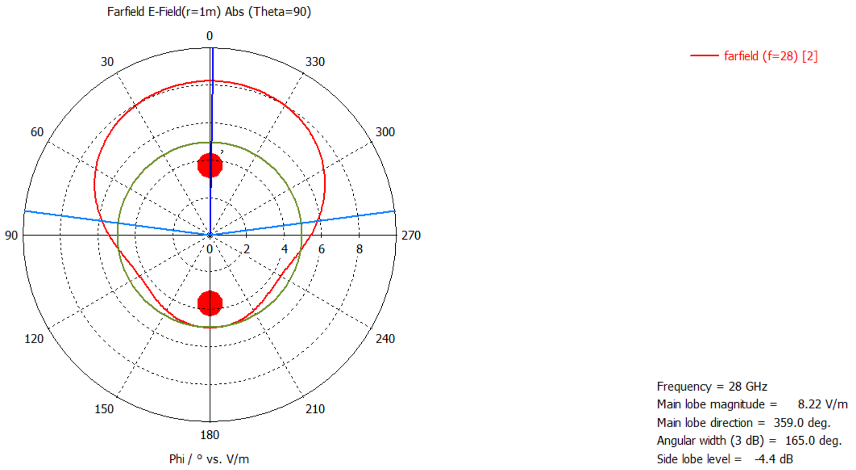

Figure 3.68: Ideal dipoles: H-plane, element 2 excited.

Planar monopoles radiation diagrams

The two planar monopoles are set side by side as the two ideal dipoles previously analyzed; so a similar radiation pattern should be expected. On the contrary, a totally different one can be observed.

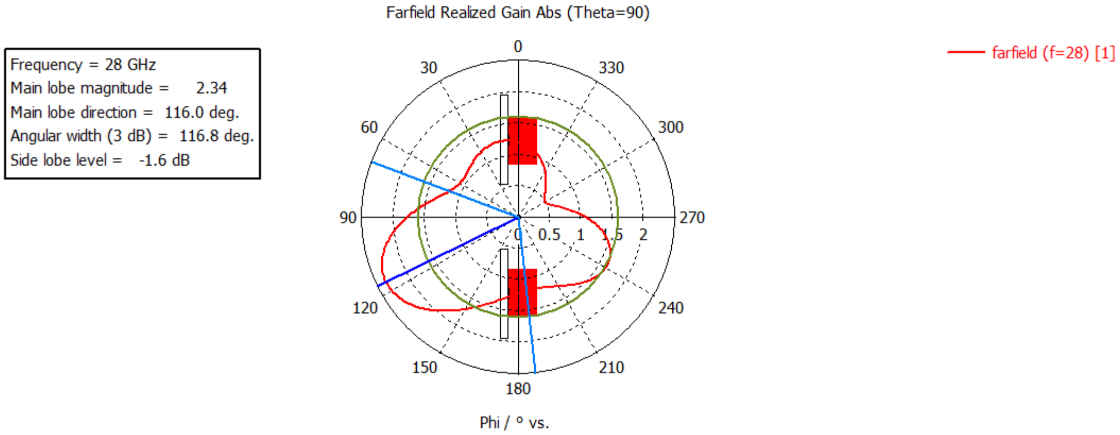

Figure 3.69: Planar monopoles: H-plane, element 1 excited.

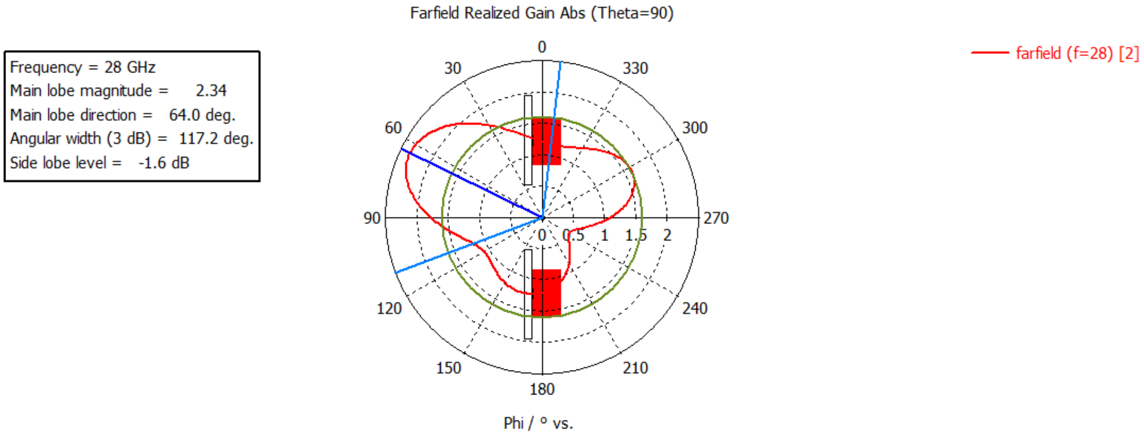

Figure 3.70: Planar monopoles: H-plane, element 2 excited.

This comparison shows the critical role of the finite ground plane in determining the azimuthal radiation properties at 28 GHz. When element 1 is excited, the ideal dipole case has a maximum close to 180°, whereas in the planar monopole the maximum is 116° and the sidelobe level goes from −4.4 dB to about −1.6 dB. Specular results are observed when port 2 is excited.

All these observations confirm that, for this project, the planar topology is not easily manageable: additional rings are expected to introduce more coupling and ground spurious radiation effects,leading to unpredictable array behavior. So, a different realistic topology is required for the final array implementation.

Chapter 4

Final Layout

In this chapter the final chosen layout is presented. The structure is a circular array of monopoles embedded in a dielectric substrate in order to have a compact and mechanically robust implementation at 28 GHz, realizing the monopoles as via-holes in the substrate. At millimeter-wave frequencies the overall structure becomes highly sensitive to any little variation: finite-ground effects, and the electromagnetic perturbation introduced by the feeding network has to be taken into account. For these reasons, the workflow adopted for this early design prioritizes the radiation pattern fidelity and controllability more than a specific real impedance matching target.

4.1 Design objective

For the first design phase, the simulations were done on a single monopole. The goals were: tuning the element resonance at 28 GHz and determine the impact of different feeding solutions (microstrip line, coplanar waveguide, and coaxial excitation) on matching and radiation characteristics. In all the considered configurations, the realized radiation pattern was observed to be distorted, with parasitic contributions given by the feeding structure.

For this reason, in the final model the elements are excited through ideal discrete ports. This choice allows to decouple the radiation properties of the radiating structure from the parasitic contributions of a specific feeding topology. The effects of a realistic feeding network will be the focus of future works. The monopole was first simulated without dielectric overlay and, in a second step, the dielectric overlay was introduced. After validating the single element behavior, the full $N = 127$ array was designed and simulated in order to reproduce, as closely as possible, the behavior of the ideal case.

4.2 The ground plane's effect

In realistic monopoles, the ground plane is necessarily finite; so, the image theoreme assumption (infinite PEC plane) does not hold. The radiation pattern is strongly influenced by edge diffraction and by the partial reflection of surface currents. A physical interpretation present in literature is that the monopole excites a surface current wave on the ground plane, which is partially diffracted and reflected by the perimeter of the gorund and so the total far field can be regarded as the sum of the field radiated by the driven monopole and an edge scattered contribution generated at the ground plane edges. This phenomenon produces additional side lobes and an elevation shift of the main beam, with a dependence on the electrical size of the ground plane (the larger the ground, the lower will be its effect on the radiation pattern). Many studies on how this this phenomenon is generated and how to counteract that are presented in literature. A study in [24] for a $\lambda_0/4$ monopole on circular and square PEC planes shows that the radiation pattern converges very slowly to the infinite-plane case as the ground size increases. In particular, for circular discs with radius a, the maximum directivity increases from about 2.5 dB at $a = 0.5\lambda_0$ to about 5.4 dB at $a = 5\lambda_0$, and the number of sidelobes below the horizontal plane increases with the disc radius according to the empirical rule $N \simeq 2\left(\frac{2a}{\lambda_0}\right)^2 - 1$.

On the other hands, mitigation techniques can be grouped into three main classes. First, rounding the edges reduces abrupt current termination and then edge diffraction; in [25] the residual gain ripple is reduced to within approximately ±0.5dBi for elevation angles above 30°. Second, reactive edge treatments reduce edge interaction by modifying the edge structure: a V-shape edge-groove added to a 1 m circular ground plane at 2 GHz reduces the elevation ripple from 26 dB to 4.5 dB, with optimal parameters approximately $h \simeq \lambda/4$ and $w \simeq \lambda/15$ (being h the "V" height and w its width), while producing only negligible changes in the input impedance [26]. A similar alternative is the use of structured grounds based on concentric rings: for a circular monopole array on a finite ground plane of radius 180 mm ($\approx 1.2\lambda$), a two-ring design (slot width 5 mm, ring width 20 mm) reduce back radiation up to 4 dB and increase the main beam gain by up to 0.5dB, with sidelobe reductions around 1 dB [27]. Third, adding a conducting sleeve effectively enlarges the ground surface without increasing the antenna horizontal extension; several works adopting this approach are reported in the literature as. [28]. Finally, the lossy edge loading gives a way to reduce the surface current before it reaches the perimeter: a resistive edge loading with sheet resistivity increasing up to above $1000\Omega/m^2$ at the outer edge reduce sidelobes below the ground plane level, but brings to an approximately 1 dB gain reduction due to dissipation [29].

In the end, the cited results indicate that finite ground effects are primarily driven by edge-induced secondary radiation.Because of this, in the design and measurement of monopoles, the ground plane must be treated as an integral part of the radiating system.

In this thesis work, a very large ground plane compared to the lenght of the monopole was used to approach the infinite plane reference case. The impact of the ground plane radius on the radiation pattern tilt was simulated for different values of lambdas.

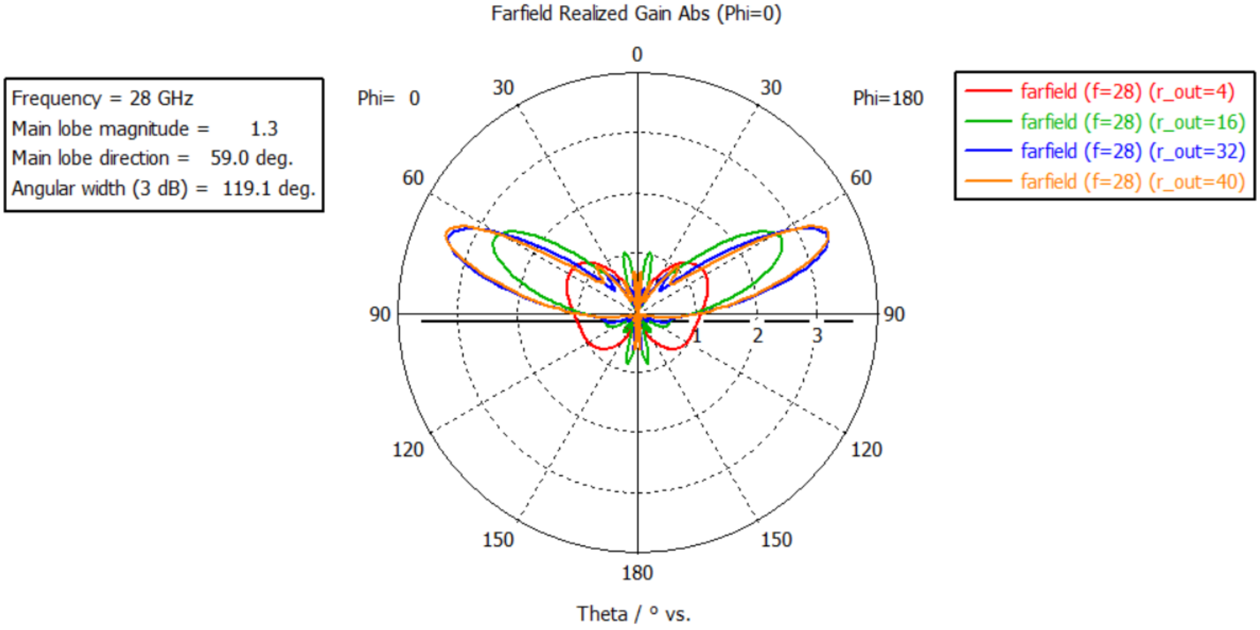

Figure 4.1: Ground-plane radius sweep: $r = 4\,\text{mm} \approx \frac{3}{8}\lambda_0$, $r = 16\,\text{mm} \approx \frac{3}{2}\lambda_0$, $r = 32\,\text{mm} \approx 3\lambda_0$, and $r = 40\,\text{mm} \approx 3.74\lambda_0$ ($\approx 4\lambda_0$) at 28 GHz.

From Fig. 4.1, the radiation-pattern tilt decreases as the radius increases and reaches a stable behavior for $r = 32mm \approx 3\lambda_0$. To have a sufficiently large ground plane for the 127 element array, a final radius of $r = 40\,\text{mm} \approx 4\lambda_0$ was selected.

4.3 Single monopole without substrate overlay

As first practical step, a single monopole without dielectric overlay was investigated at f_0 =28 GHz. As seen in the previous Chapter, the arm length is expected to be close to $\lambda_0/4$. The monopole is excited by a discrete port with characteristic impedance

$$Z_0 = 73\ \Omega. \tag{4.1}$$

After the issues observed in Chapter 3 (related to ground effects), the main focus at this stage was to obtain an efficient radiating structure exhibiting a radiation pattern as close as possible to the ideal monopole behavior. So, the complex input-impedance requirement

$$Z_{\text{in,ref}} = 73 + j\,42\ \Omega \qquad \text{at } 28\,\text{GHz}, \tag{4.2}$$

was not taken as goal in this phase.

4.3.1 Layout

Substrate and metallization choice

The selected substrate (here considered with negligible height) is characterized by relative permittivity $\varepsilon_r = 2$, relative permeability $\mu_r = 1$, loss tangent $\tan\delta = 0.001$, and thermal conductivity $k_{\text{th}} \approx 0.5\,\text{W/(Km)}$.

The stack-up consists of a dielectric layer having the same height as the discrete port

$$h_{\text{sub}} = 0.2\,\text{mm}, \tag{4.3}$$

and a bottom copper layer acting as ground plane of thickness:

$$h_{\text{met}} = 0.018\,\text{mm}. \tag{4.4}$$

Geometry

The substrate has the same dimensions of the ground plane and is considered square in a first step. Because of the ground plane effects observed in the previous section, the ground was selected to have a very large extension. In particular,

$$L_{\text{sub}} = W_{\text{sub}} = 80\,\text{mm.} \approx 8\lambda_0 \qquad \text{at } 28\,\text{GHz}. \tag{4.5}$$

The monopole is modeled as a hexahedral conductor with square cross-section and dimensions

$$h_{\text{arm}} = 3.1\,\text{mm}, \qquad W_{\text{arm}} = 0.5\,\text{mm}. \tag{4.6}$$

Sizing and tuning

The monopole height and width were selected via parameter sweeps starting from the free-space quarter-wavelength estimate $\lambda_0/4 \approx 2.67mm$, in order to place the resonance at 28 GHz.

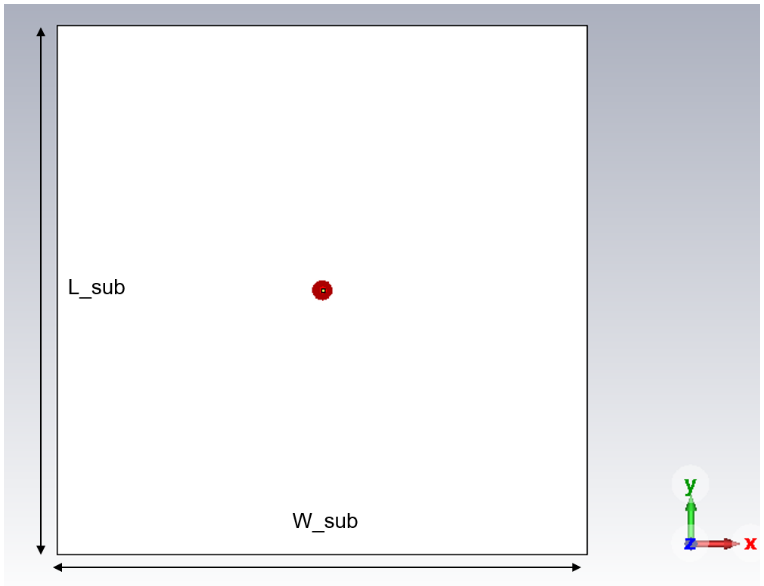

Figure 4.2: Single monopole with square ground plane and no substrate overlay: top view.

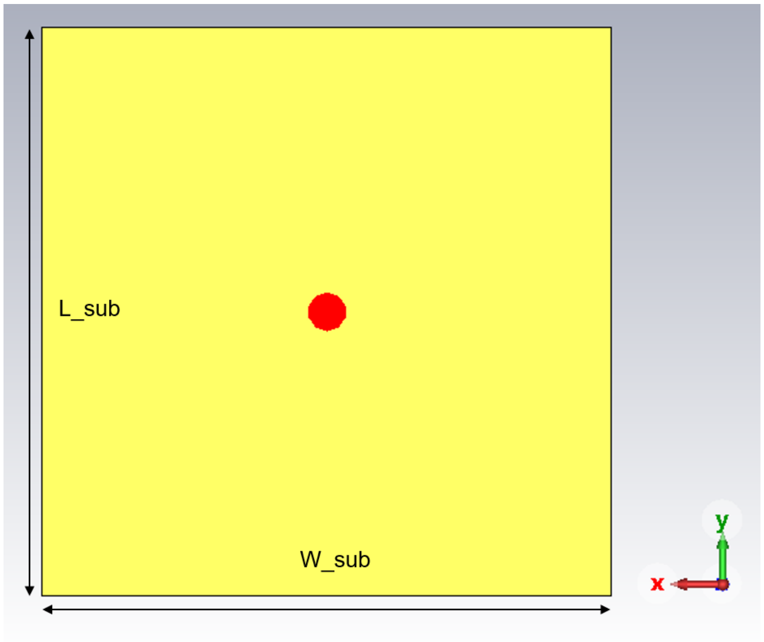

Figure 4.3: Single monopole with square ground plane and no substrate overlay: bottom view.

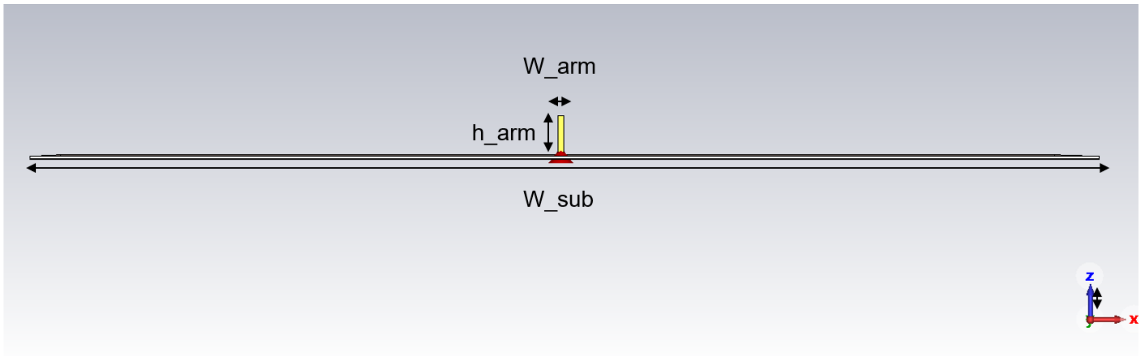

Figure 4.4: Single monopole with square ground plane and no substrate overlay: lateral view.

4.3.2 Results

S_{11}

The simulated reflection coefficient is well below $-10\,\mathrm{dB}$. In particular, at $28\,\mathrm{GHz}$

$$S_{11}(28\,\mathrm{GHz}) \approx -19\,\mathrm{dB}. \tag{4.7}$$

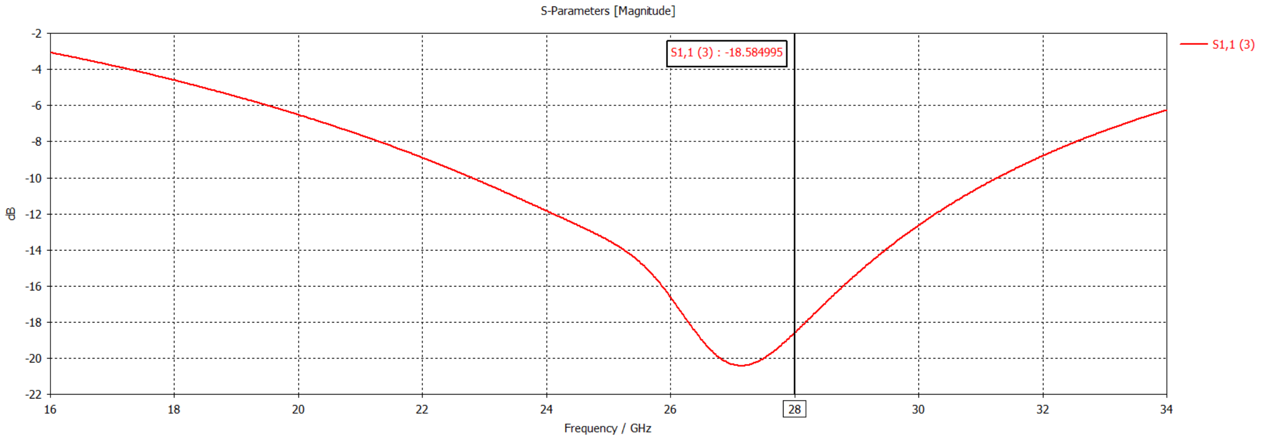

Figure 4.5: Single monopole on square ground plane: S_{11}.

Z_{in}

The input impedance extracted at the feed is

$$Z_{\text{in}} \approx 60 + j9\Omega, \tag{4.8}$$

which is close to the reference port impedance $Z_0 = 73\,\Omega$.

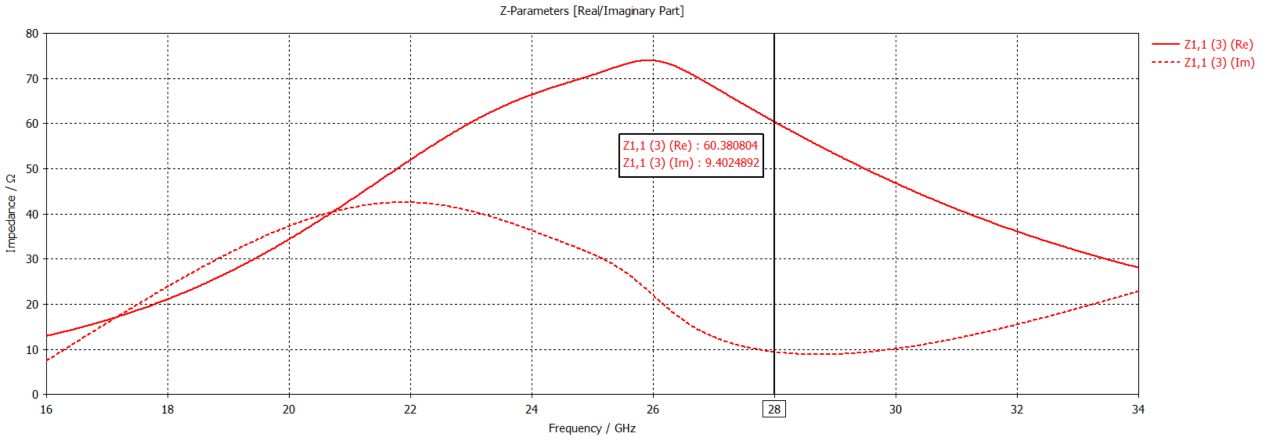

Figure 4.6: Single monopole on square ground plane: Z_{in}.

Radiation pattern and surface currents

The 3D radiation pattern shows directional lobes aligned with the square edges, whereas an ideal monopole is expected to be omnidirectional in the azimuthal plane.

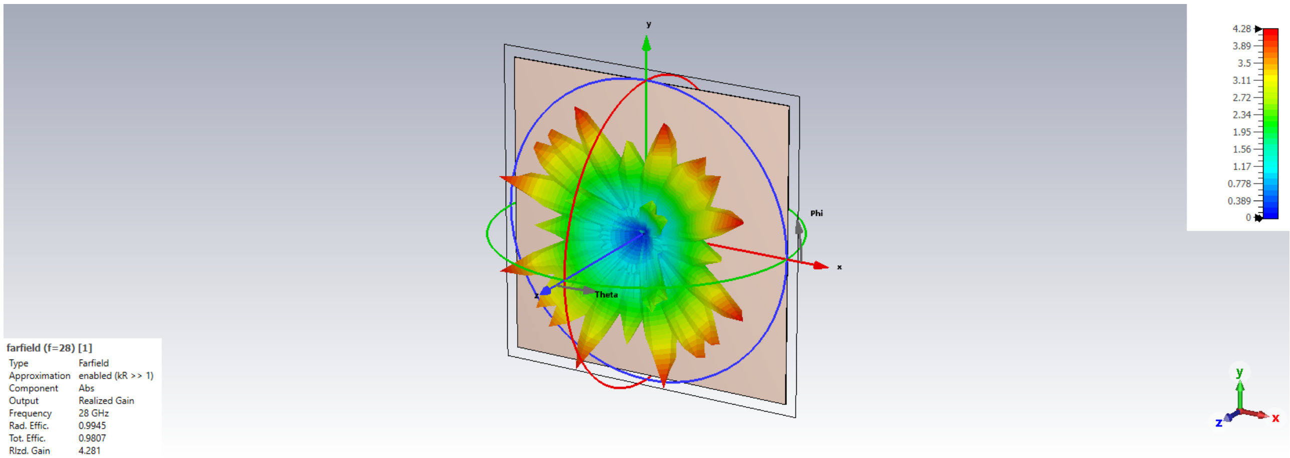

farfield (f=28) [1]

Type	Farfield
Approximation	enabled (kR >> 1)
Component	Abs
Output	Realized Gain
Frequency	28 GHz
Rad. Effic.	0.9945
Tot. Effic.	0.9807
Rlzd. Gain	4.281

Figure 4.7: Single monopole on square ground plane: 3D radiation pattern.

To clarify the origin of this behavior, the surface currents on the ground plane were analyzed.

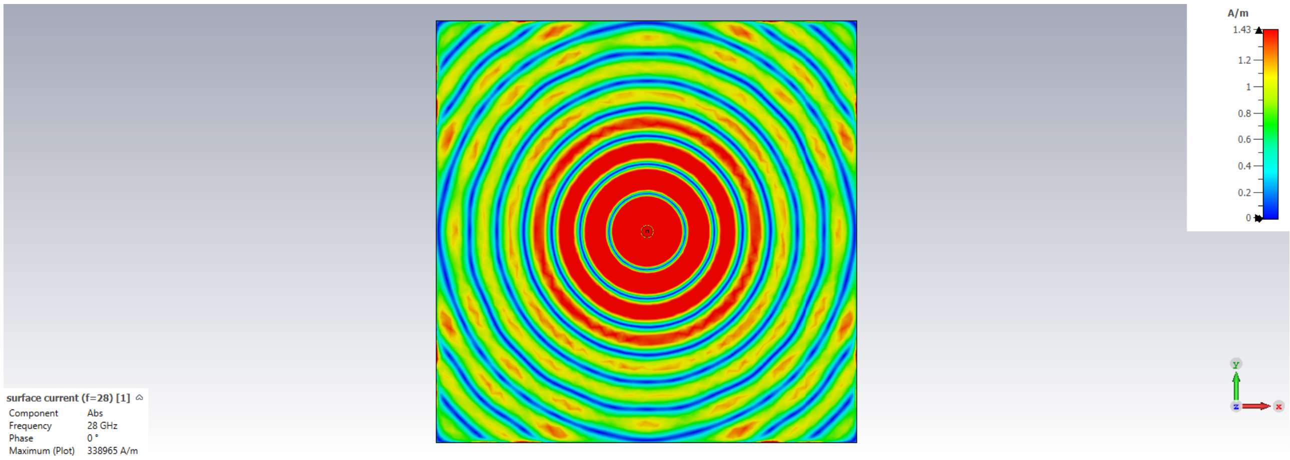

surface current (f=28) [1]

Component	Abs
Frequency	28 GHz
Phase	0 °
Maximum (Plot)	338965 A/m

Figure 4.8: Single monopole on square ground plane: surface-current distribution.

Fig. 4.8 shows current accumulation in correspondence of the ground corners. This non uniform current distribution brings to a radiation contribution of the corners, which produces the observed azimuthal directivity. To avoid this corner effect, a circular ground-plane layout was adopted.

4.3.3 Monopole on a circular ground plane

The new layout uses the same monopole as in Section4.3, while replacing the square ground plane with a circular one. In order to have the same extent of the square case

(4.5), the circular ground plane is set with radius

$$R_{\text{out}} = 40\,\text{mm}, \tag{4.9}$$

so that the diameter equals 80mm, equal to the square edge length.

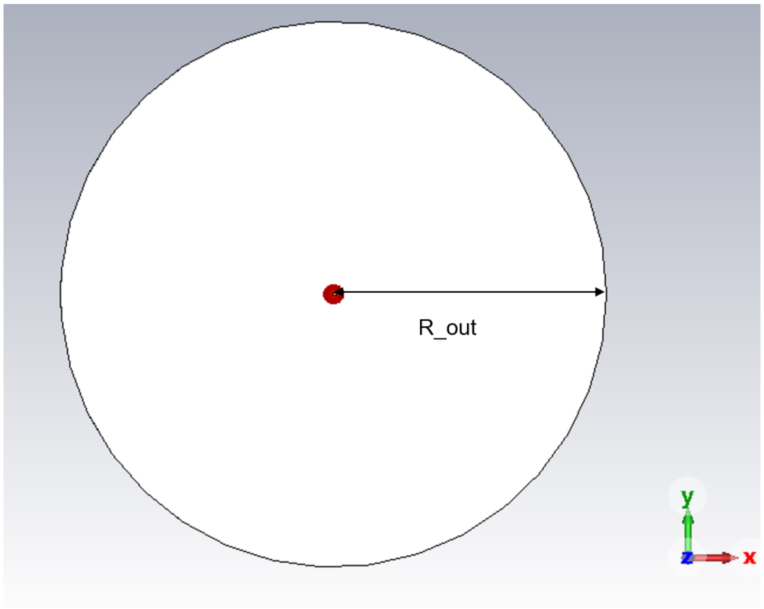

Figure 4.9: Single monopole on circular ground plane: top view.

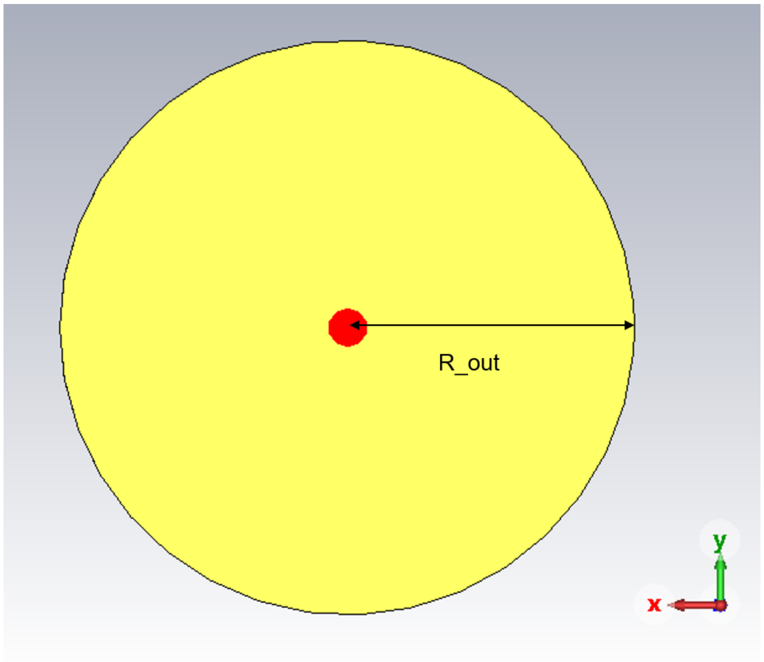

Figure 4.10: Single monopole on circular ground plane: bottom view.

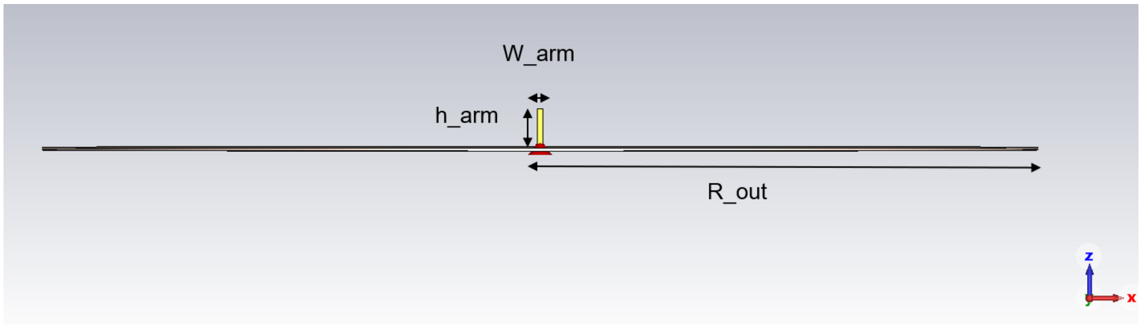

Figure 4.11: Single monopole on circular ground plane: lateral view.

4.3.4 Results

S_{11}

With respect to the square ground plane, a slight change in matching is observed. In particular,

$$S_{11}(28\,\text{GHz}) \approx -18.2\,\text{dB}. \tag{4.10}$$

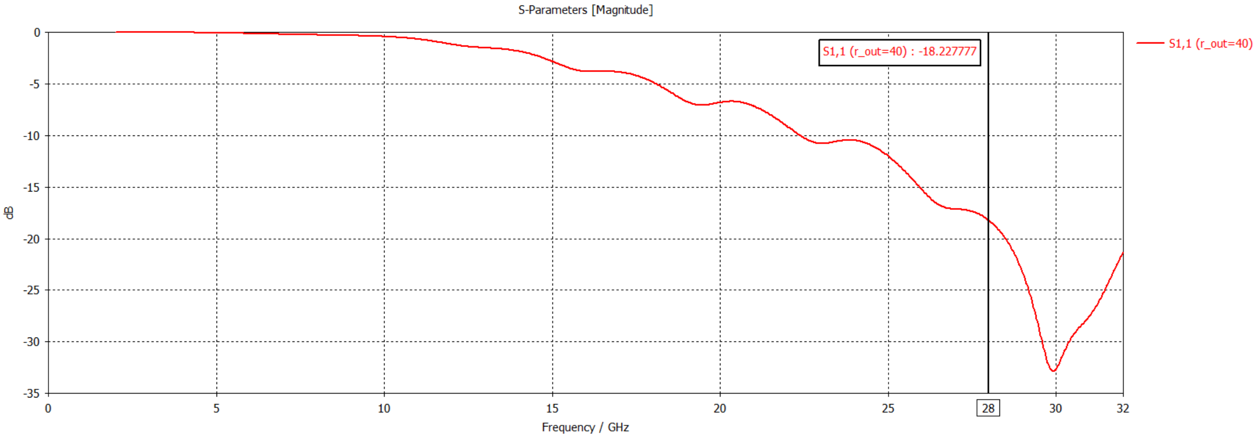

Figure 4.12: Single monopole on circular ground plane: S_{11}.

Z_{in}

The input impedance extracted at the feed is

$$Z_{\text{in}} \approx 87 + j13\ \Omega, \tag{4.11}$$

still close to the reference port impedance level.

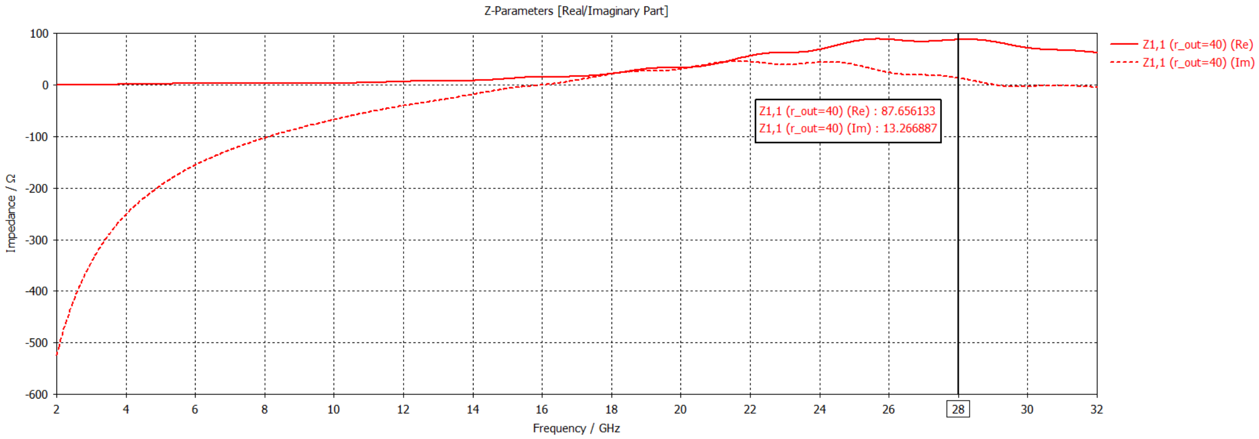

Figure 4.13: Single monopole on circular ground plane: Z_{in}.

Radiation pattern and surface currents

The 3D radiation pattern and the cuts show that azimuthal omnidirectionality is restored thanks to the circular ground plane. The realized gain obtained in this case is 3.529 in linear scale.

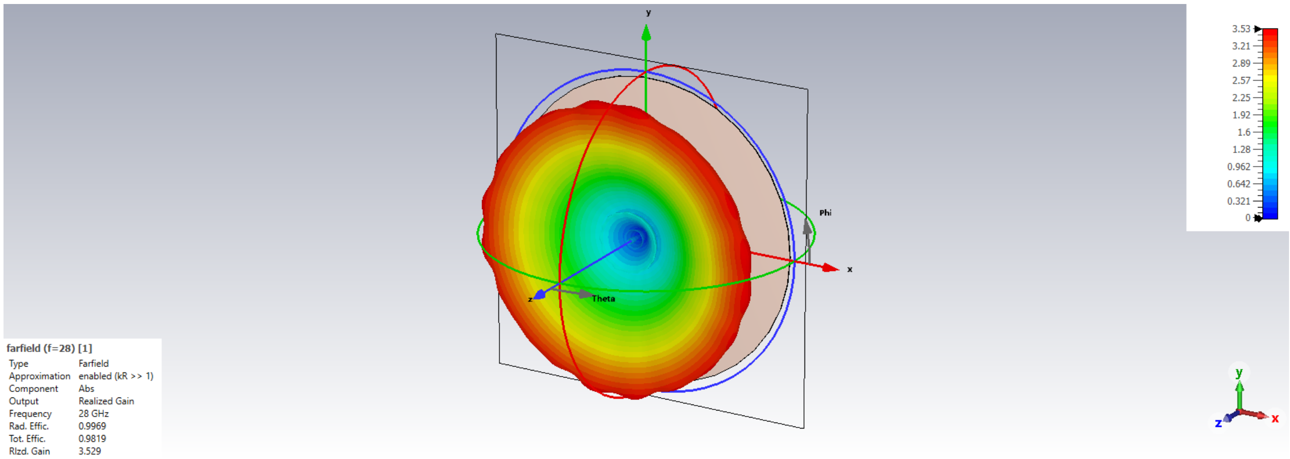

farfield (f=28) [1]

Type	Farfield
Approximation	enabled (kR >> 1)
Component	Abs
Output	Realized Gain
Frequency	28 GHz
Rad. Effic.	0.9969
Tot. Effic.	0.9819
Rlzd. Gain	3.529

Figure 4.14: Single monopole on circular ground plane: 3D radiation pattern.

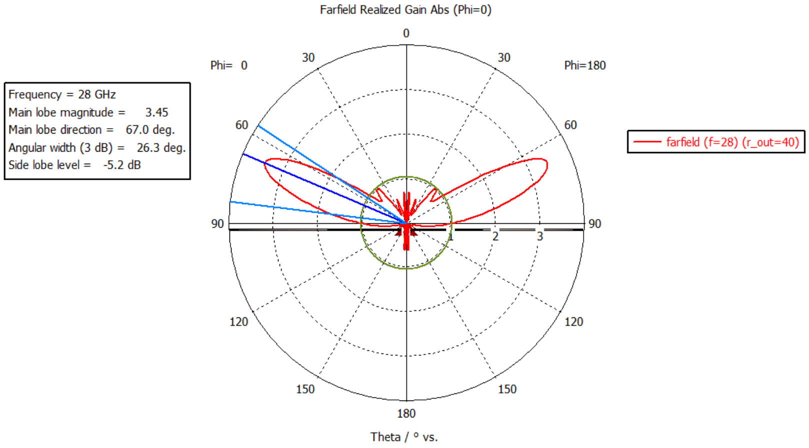

Figure 4.15: Single monopole on circular ground plane: E-plane cut.

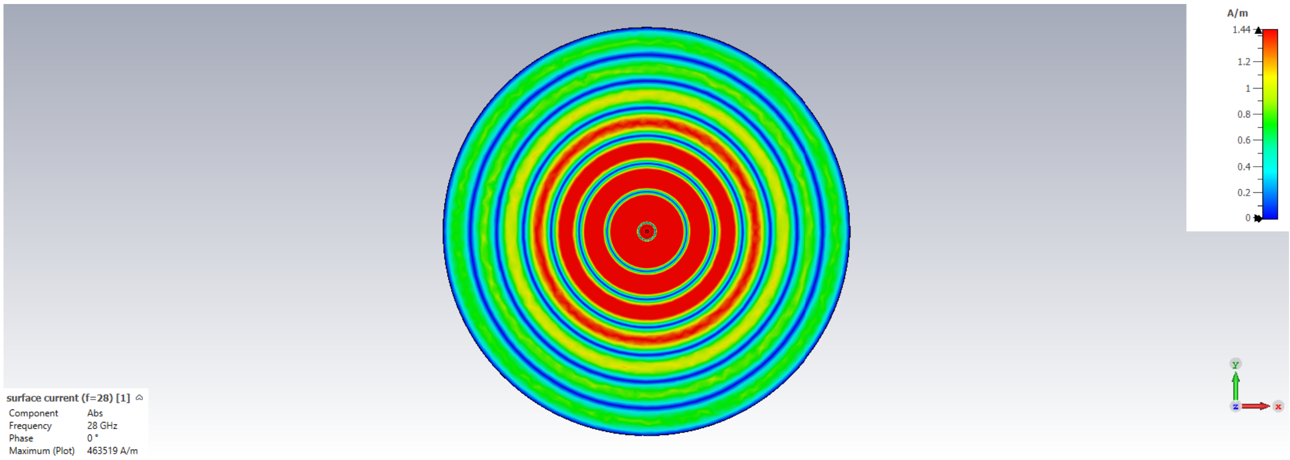

Figure 4.16: Single monopole on circular ground plane: surface-current distribution.

Compared to Fig.4.8, the current distribution in Fig.4.16 is more homogeneous due to the absence of corners. From this point onward, the circular-ground configuration is adopted.

4.4 Single monopole with substrate overlay

In this section, a single monopole above a circular ground plane is studied after introducing a dielectric overlay, with the final objective of realizing the monopoles as via-holes. As reported for similar topologies in [10, 12, 11], the monopole dimensions must be tuned again by considering the guided wavelength in the dielectric rather than the free-space one.

4.4.1 Layout

The metallization and substrate are the same as in previous sevtions. The overlay height is selected to be significantly larger than the monopole height, in order to create a sufficiently homogeneous dielectric environment around the monopole and to reduce diffraction phenomena at the dielectric-air interface.

Geometry

The substrate overlay has radius

$$R_{\text{out}} = 40\,\text{mm} \approx 4\lambda_0 \qquad \text{at } 28\,\text{GHz}, \tag{4.12}$$

and height

$$H_{\text{sub}} = 22.39\,\text{mm} \approx 3\lambda_g \qquad \text{at } 28\,\text{GHz}, \tag{4.13}$$

where λ_g is the wavelength in the substrate, defined as

$$\lambda_g = \frac{\lambda_0}{\sqrt{\varepsilon_r}}. \tag{4.14}$$

The monopole is modeled as a hexahedron with

$$h_{\text{arm}} = 2.14\,\text{mm}, \qquad W_{\text{arm}} = 0.50\,\text{mm}. \tag{4.15}$$

Sizing and tuning

The monopole dimensions were tuned via parameter sweeps starting from $\lambda_g/4 \approx 1.89 mm$.

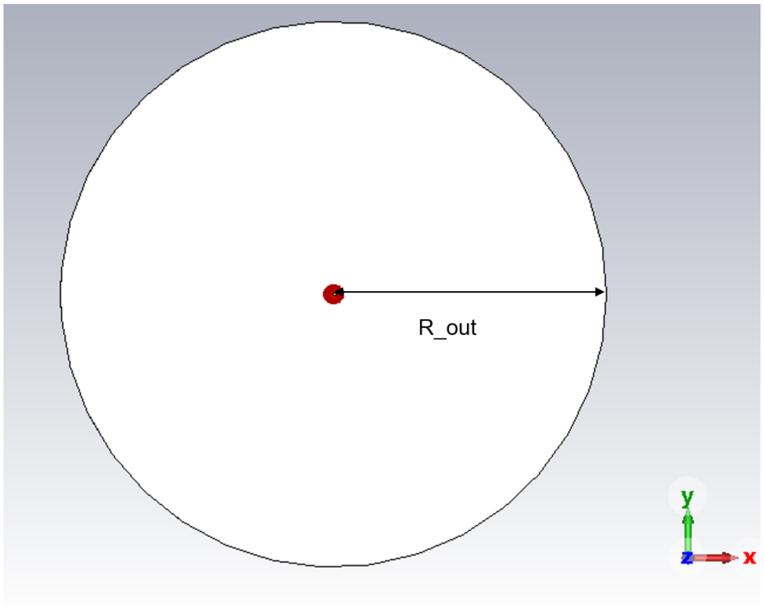

Figure 4.17: Single monopole embedded in the substrate: top view.

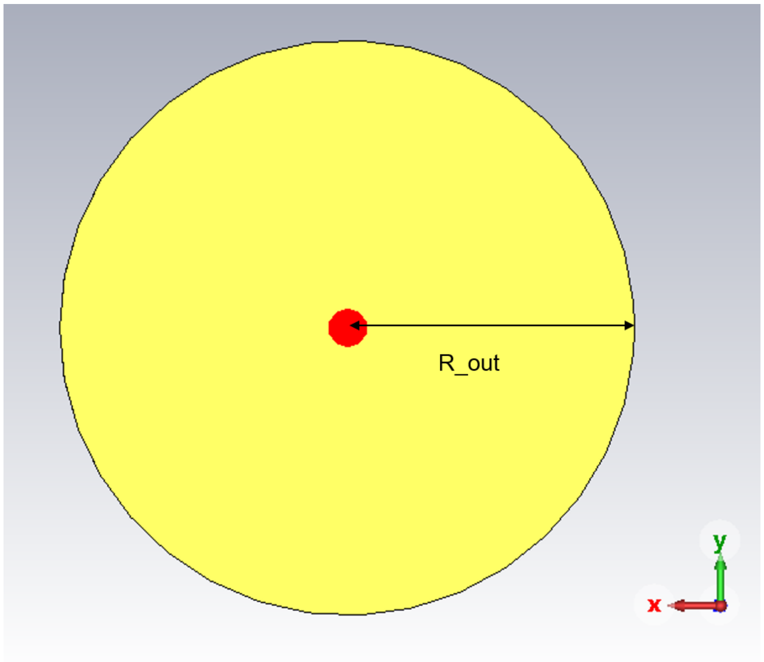

Figure 4.18: Single monopole embedded in the substrate: bottom view.

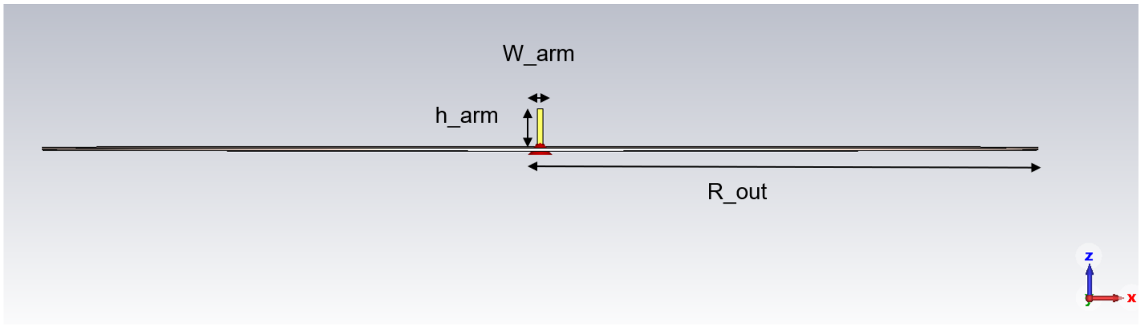

Figure 4.19: Single monopole embedded in the substrate: inside lateral view.

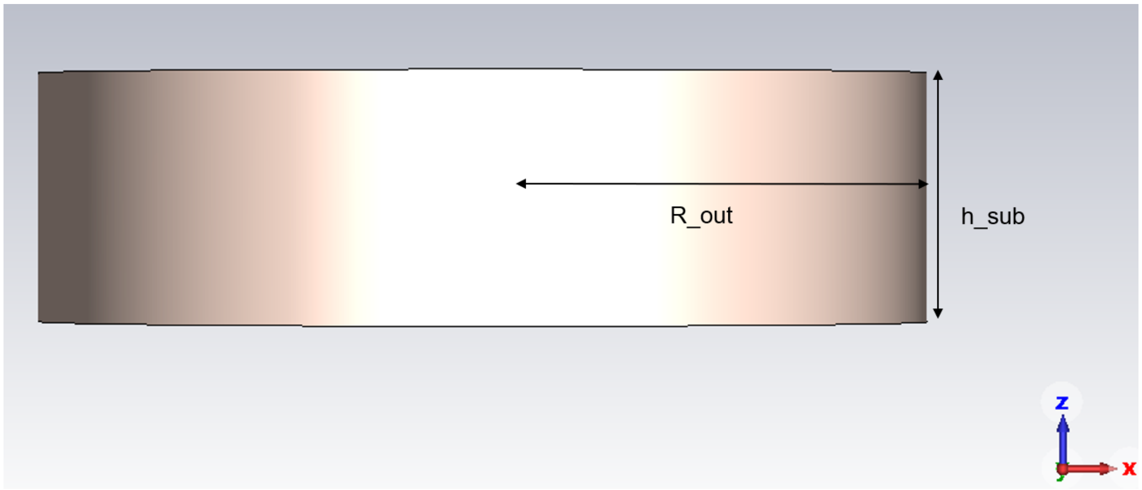

Figure 4.20: Single monopole embedded in the substrate: outside lateral view.

4.4.2 Results

S_{11}

The simulated reflection coefficient is close to -10dB. In particular,

$$S_{11}(28\,\text{GHz}) \approx -9.7\,\text{dB}. \tag{4.16}$$

N.B. In order to reduce simulation time, from this point onward the results are reported at a single frequency point (28GHz).

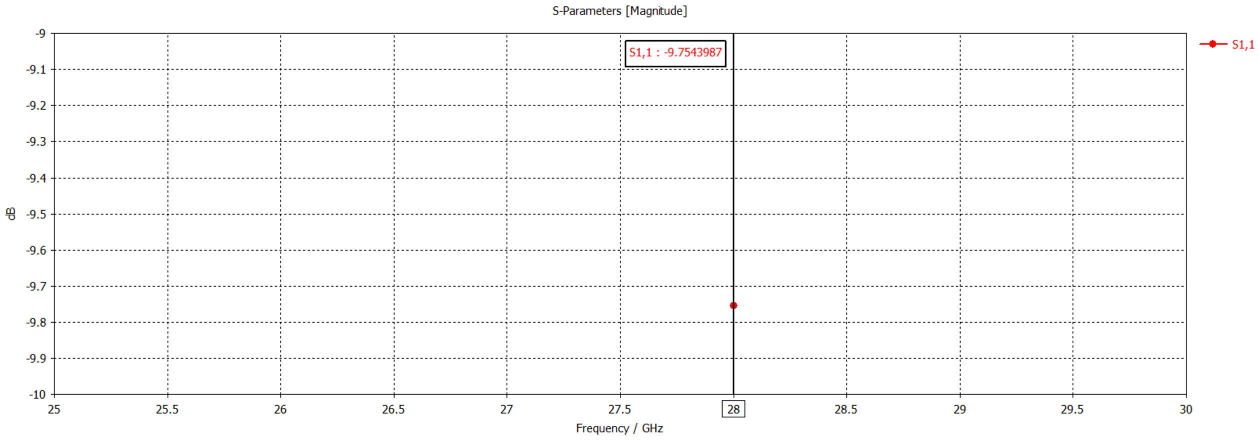

Figure 4.21: Single monopole embedded in dielectric: S_{11}.

Z_{in}

The input impedance extracted at the feed is

$$Z_{\text{in}} \approx 59 + j43\ \Omega, \tag{4.17}$$

different from the no-overlay case, showing that the dielectric environment shifts the resonance and modifies the reactive part.

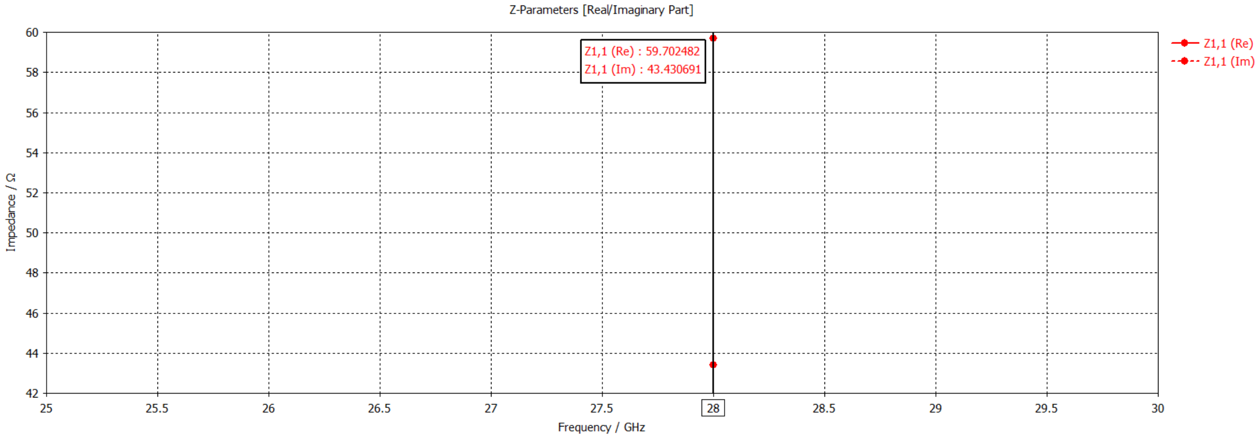

Figure 4.22: Single monopole embedded in dielectric: Z_{in}.

Radiation pattern

From the 3D pattern and the E-plane cut, the elevation of the main lobe is similar to the no-overlay case: here $\theta_M = 71°$, while in the case without substrate $\theta_M = 67°$. Moreover, the dielectric overlay increases the realized gain from 3.529 to 4.613 and reduces sidelobes.

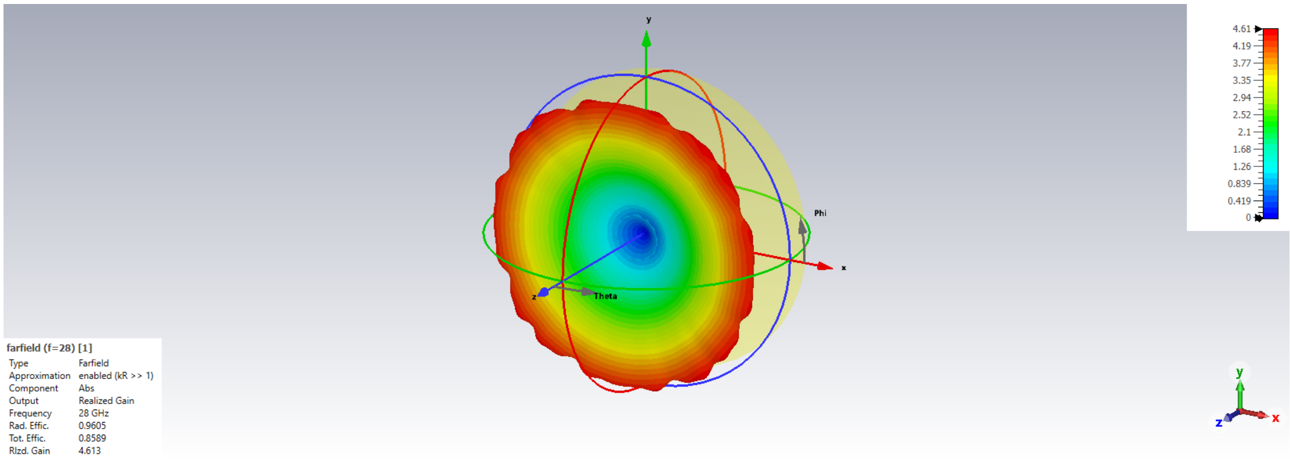

```
farfield (f=28) [1]
Type            Farfield
Approximation   enabled (kR >> 1)
Component       Abs
Output          Realized Gain
Frequency       28 GHz
Rad. Effic.     0.9605
Tot. Effic.     0.8589
Rlzd. Gain      4.613
```

Figure 4.23: Single monopole embedded in dielectric: 3D radiation pattern.

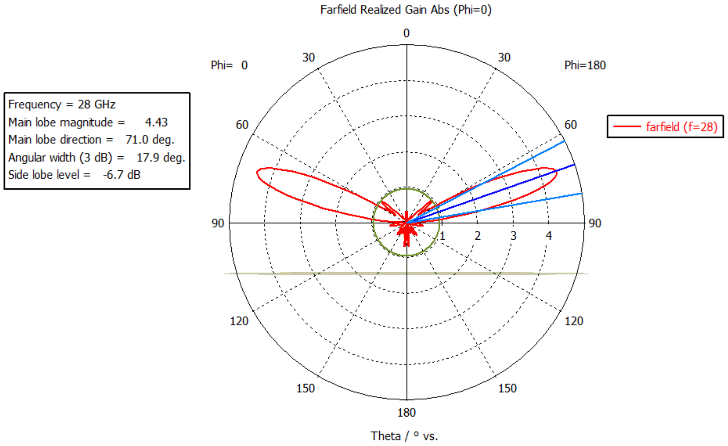

```
Frequency = 28 GHz
Main lobe magnitude =     4.43
Main lobe direction =   71.0 deg.
Angular width (3 dB) =   17.9 deg.
Side lobe level =   -6.7 dB
```

Figure 4.24: Single monopole embedded in dielectric: E-plane cut.

4.5 127-monopole array

In this section the final $N = 127$ array layout is presented and the corresponding simulation results are reported.

4.5.1 Layout

Starting from the single embedded monopole of Section 4.4, the array is constructed by one central element and six concentric rings containing, respectively, $6, 12, 18, 24, 30, 36$ elements. Each ring is spaced by $d = \lambda_0/4$ from the adjacent ring in order to enhance mutual coupling.

The substrate height and ground plane dimensions are the same as in the single element embedded case:

$$R_{\text{out}} = 40\,\text{mm} \approx 4\lambda_0 \qquad \text{at } 28\,\text{GHz}, \tag{4.18}$$

$$H_{\text{sub}} = 22.39\,\text{mm} \approx 3\lambda_g \qquad \text{at } 28\,\text{GHz}, \tag{4.19}$$

with λ_g defined by (4.14). The monopoles are modeled as hexahedra with

$$h_{\text{arm}} = 2.14\,\text{mm}, \qquad W_{\text{arm}} = 0.5\,\text{mm}. \tag{4.20}$$

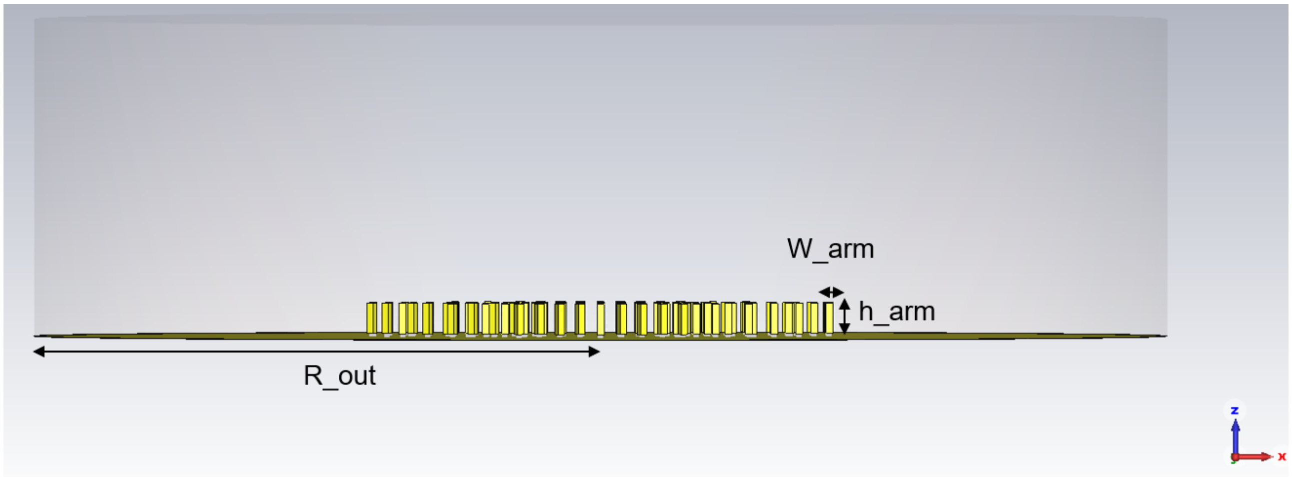

Figure 4.25: Array: inside-dielectric lateral view.

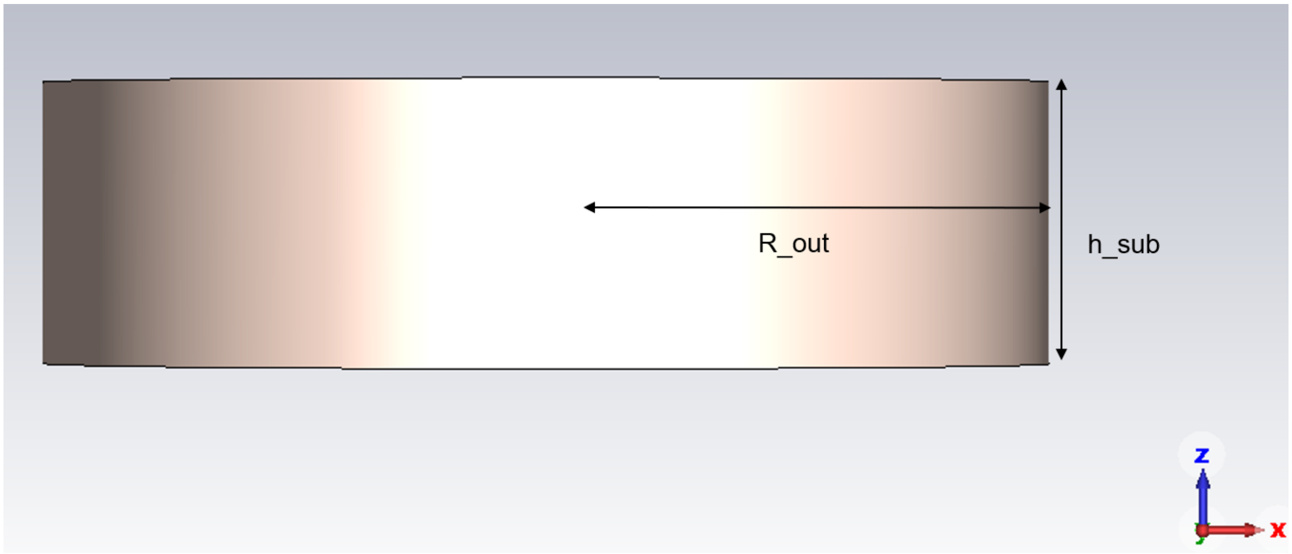

Figure 4.26: Array: outside-dielectric lateral view.

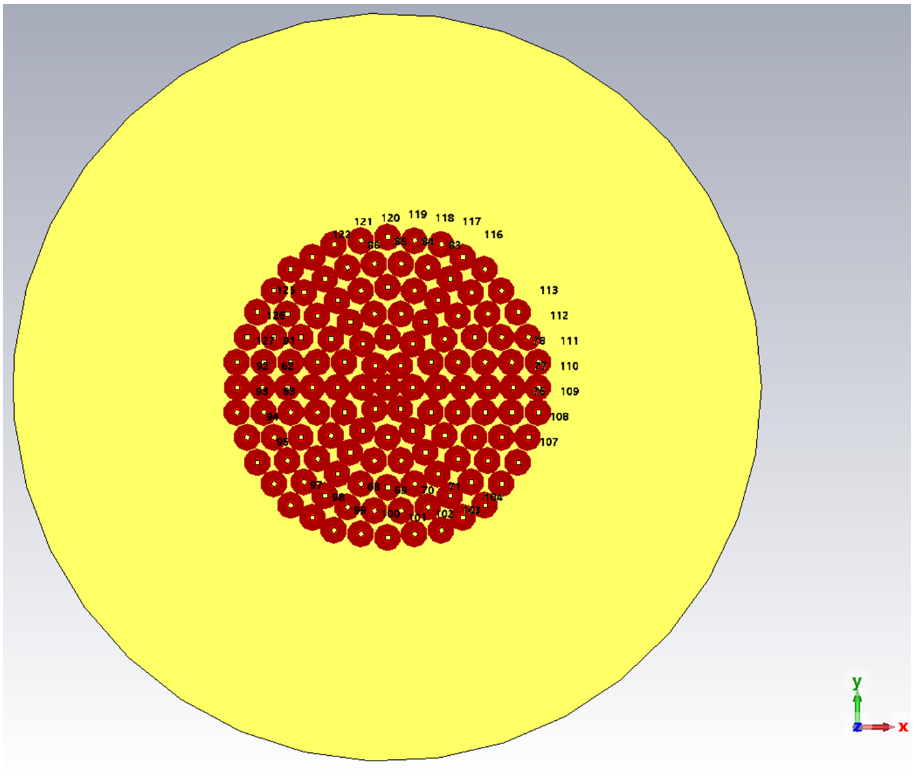

Figure 4.27: Array: top view inside the dielectric.

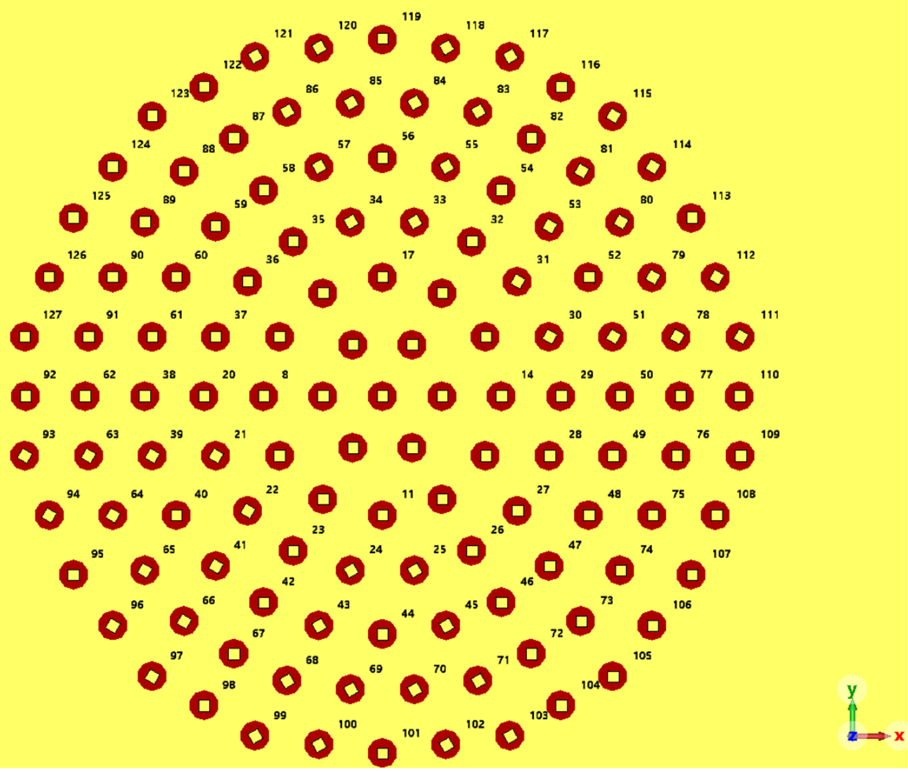

Figure 4.28: Array: top view (monopole detail).

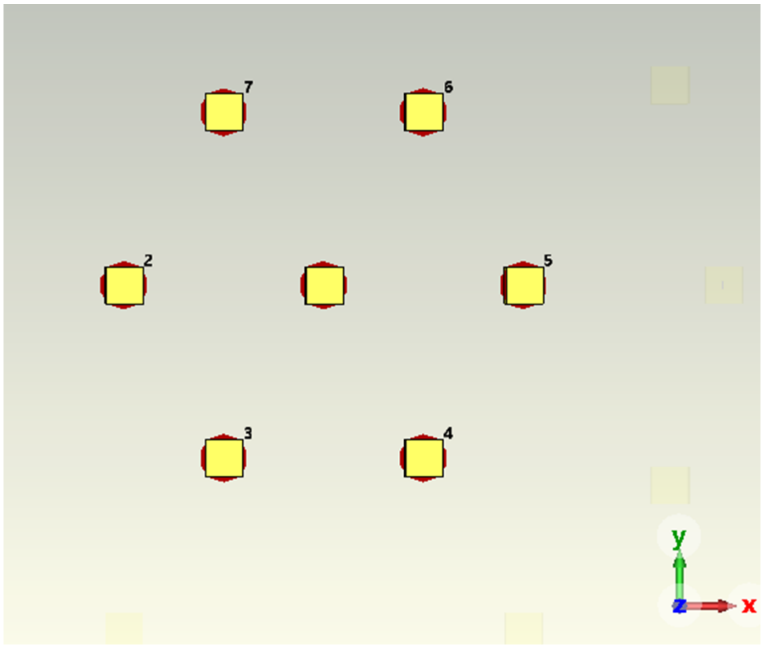

Figure 4.29: Array: first-ring detail.

4.5.2 Results

S_{11}

At $28GHz$ the reflection coefficient at the central element is

$$S_{11}(28\,\mathrm{GHz}) \approx -10.6\,\mathrm{dB}, \tag{4.21}$$

showig accettable matching at the reference port.

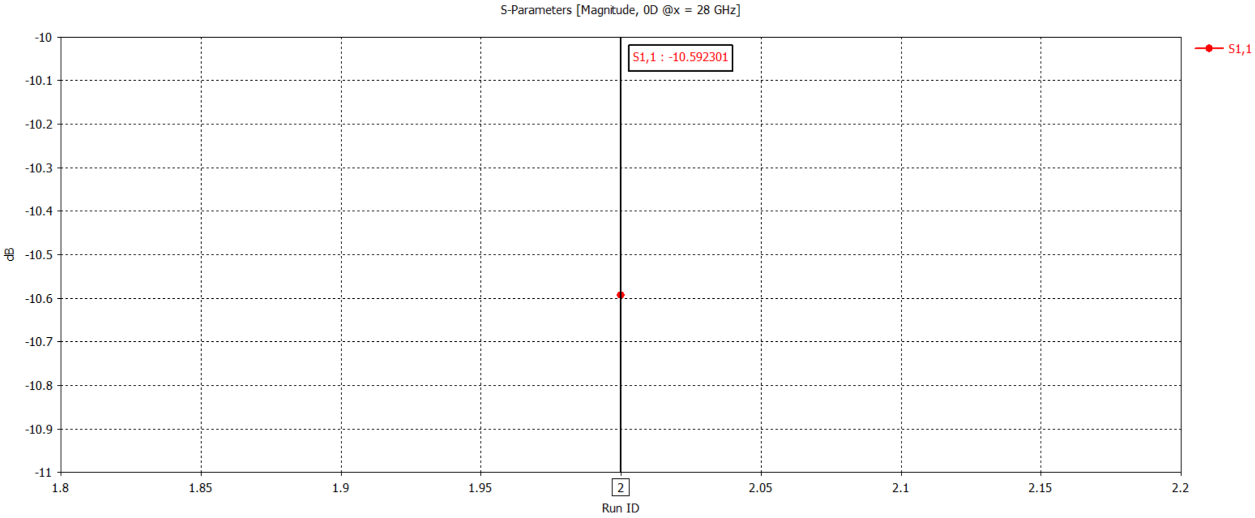

Figure 4.30: Array: S_{11} (central element).

S_{1j}

The dominant coupling coefficients between the central element and the first ring elements are on the order of

$$S_{1j}(28\,\mathrm{GHz}) \approx -10.6\,\mathrm{dB}, \tag{4.22}$$

indicating that mutual coupling is significant and is enhanced by the chosen spacing $d = \lambda_0/4$.

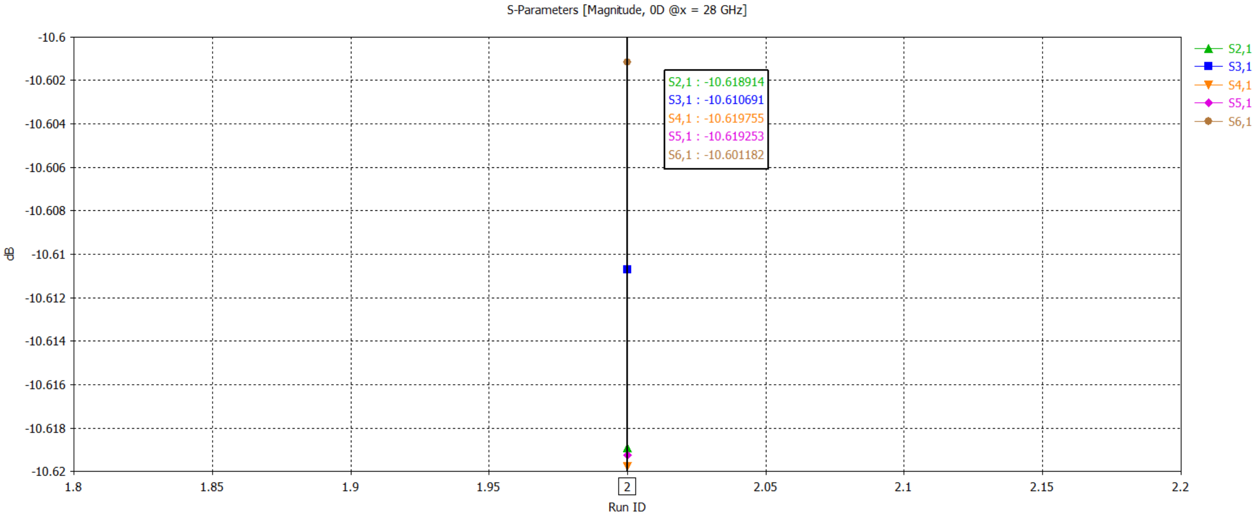

Figure 4.31: Array: S_{1j} (central-to-first-ring couplings).

Radiation pattern

From the radiation pattern of the central element, the elevation of the main lobe is still comparable to the single element embedded case, going from $\theta_M = 71°$ (single element) to $\theta_M = 78°$ (central element of the array). The presence of many parasitic elements seems to increase the number of sidelobes, according to the coupling in (4.22).

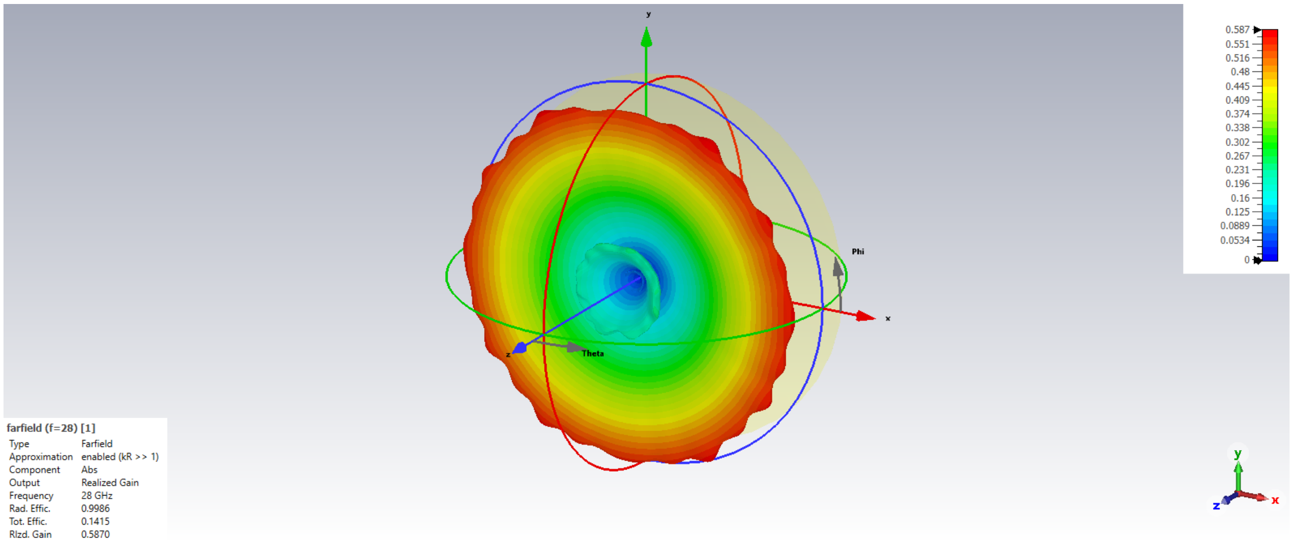

farfield (f=28) [1]

Type	Farfield
Approximation	enabled (kR >> 1)
Component	Abs
Output	Realized Gain
Frequency	28 GHz
Rad. Effic.	0.9986
Tot. Effic.	0.1415
Rlzd. Gain	0.5870

Figure 4.32: Array: central element 3D radiation pattern.

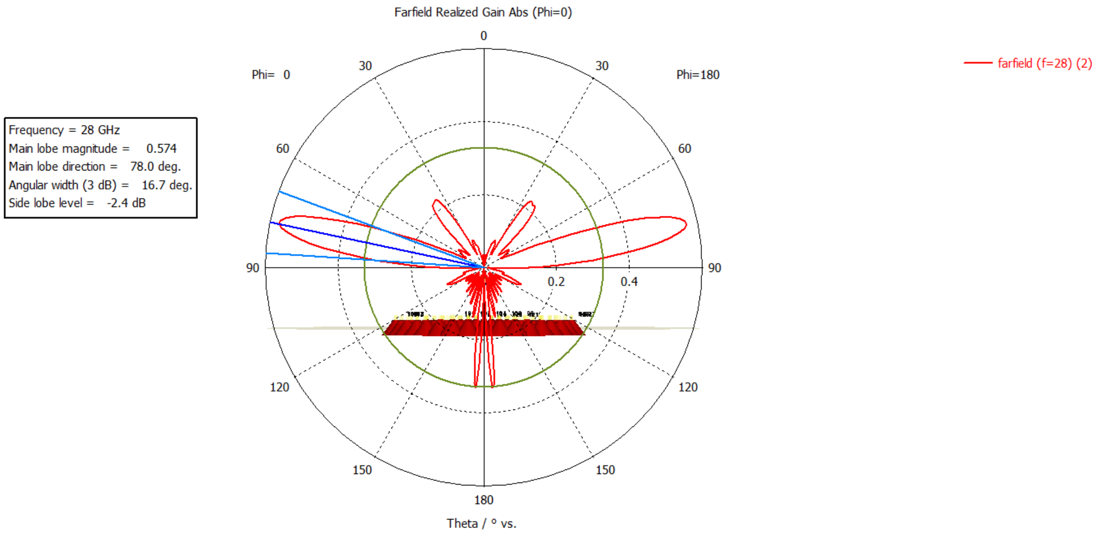

Frequency = 28 GHz
Main lobe magnitude = 0.574
Main lobe direction = 78.0 deg.
Angular width (3 dB) = 16.7 deg.
Side lobe level = -2.4 dB

Figure 4.33: Array: central element E-plane cut.

Considering the first ring layout in Fig.4.29, the directive behavior can be observed by exciting each element in the ring one by one (while the remaining ones are closed on their characteristic impedance), this brings to a main radiation direction associated with the excited port, as expected.

1. **Second element fed**:

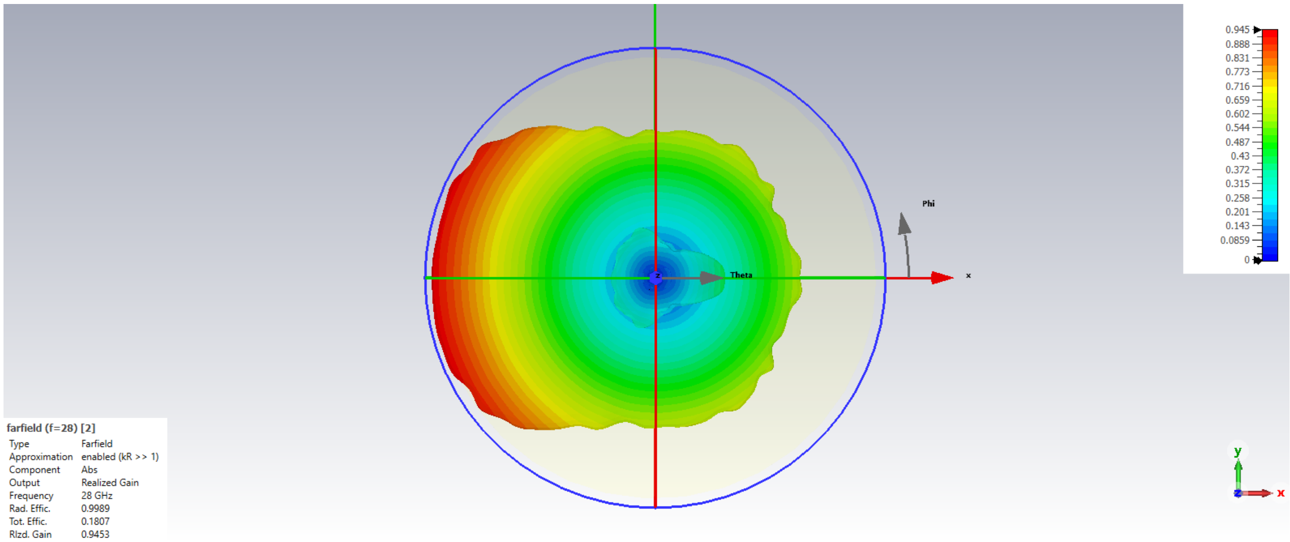

farfield (f=28) [2]
Type Farfield
Approximation enabled (kR >> 1)
Component Abs
Output Realized Gain
Frequency 28 GHz
Rad. Effic. 0.9989
Tot. Effic. 0.1807
Rlzd. Gain 0.9453

Figure 4.34: Second element fed: 3D top view.

2. **Third element fed**:

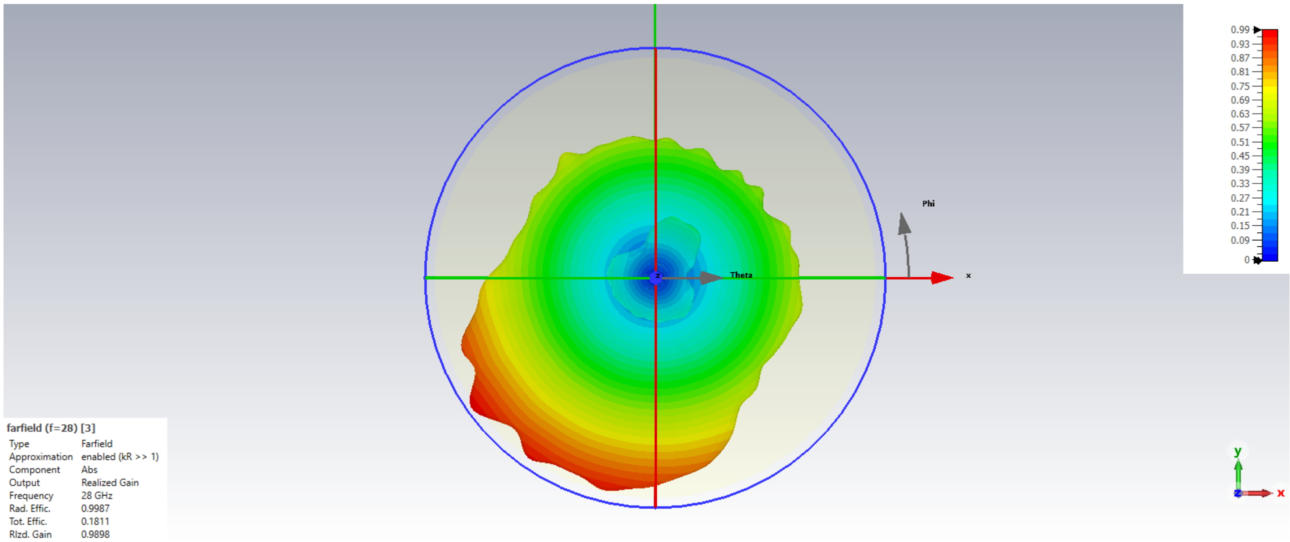

farfield (f=28) [3]
Type Farfield
Approximation enabled (kR >> 1)
Component Abs
Output Realized Gain
Frequency 28 GHz
Rad. Effic. 0.9987
Tot. Effic. 0.1811
Rlzd. Gain 0.9898

Figure 4.35: Third element fed: 3D top view.

3. **Fourth element fed**:

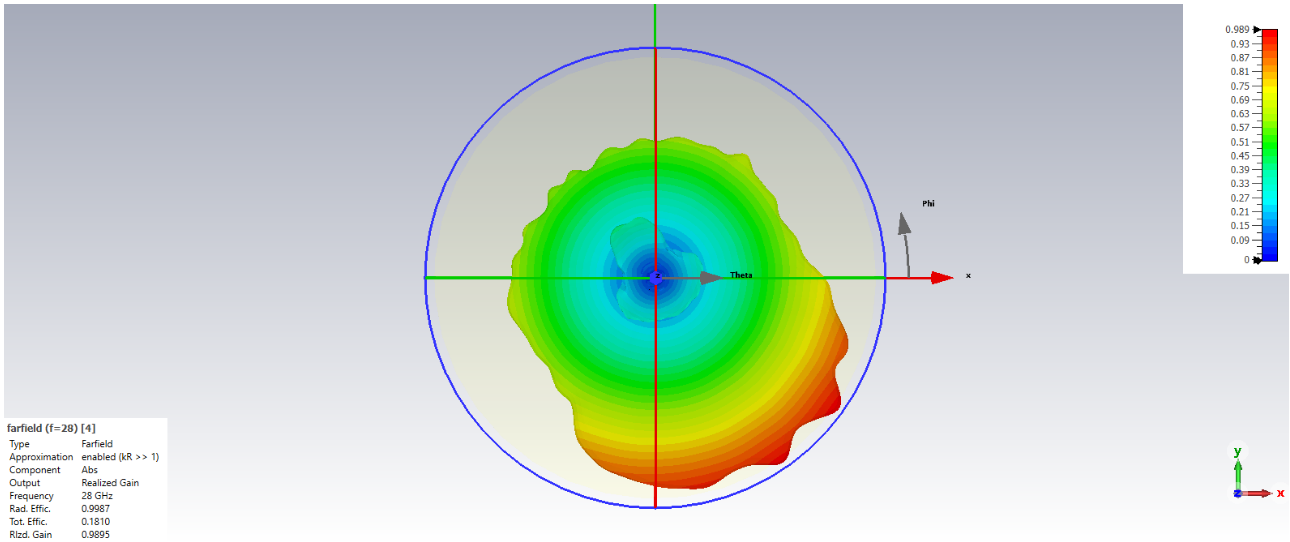

farfield (f=28) [4]
Type Farfield
Approximation enabled (kR >> 1)
Component Abs
Output Realized Gain
Frequency 28 GHz
Rad. Effic. 0.9987
Tot. Effic. 0.1810
Rlzd. Gain 0.9895

Figure 4.36: Fourth element fed: 3D top view.

4. **Fifth element fed**:

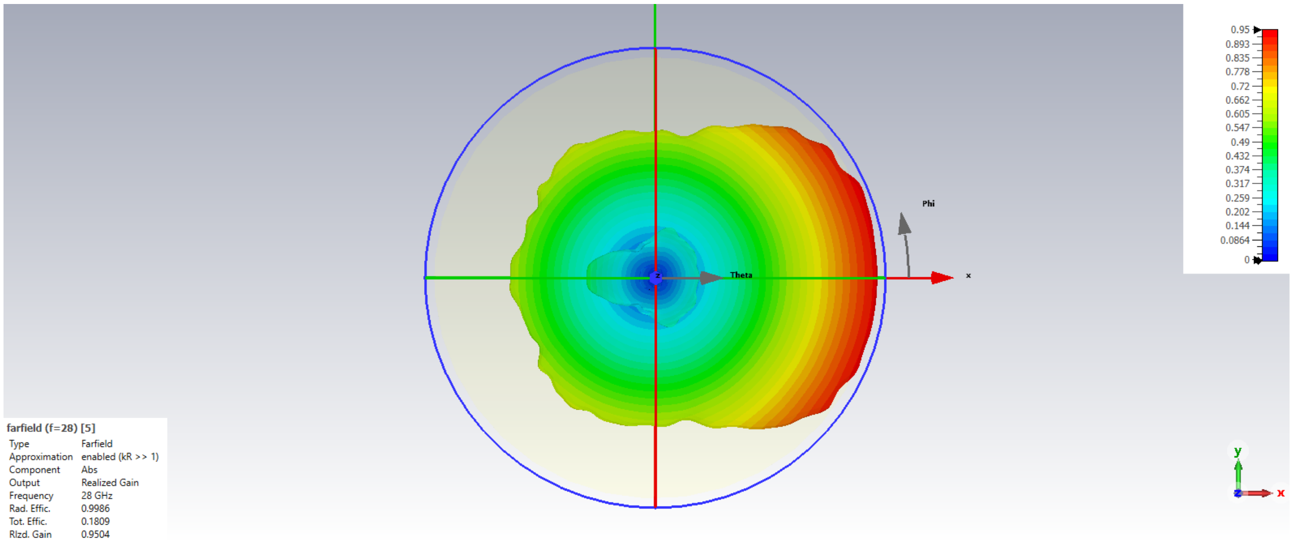

farfield (f=28) [5]
Type Farfield
Approximation enabled (kR >> 1)
Component Abs
Output Realized Gain
Frequency 28 GHz
Rad. Effic. 0.9986
Tot. Effic. 0.1809
Rlzd. Gain 0.9504

Figure 4.37: Fifth element fed: 3D top view.

5. **Sixth element fed**:

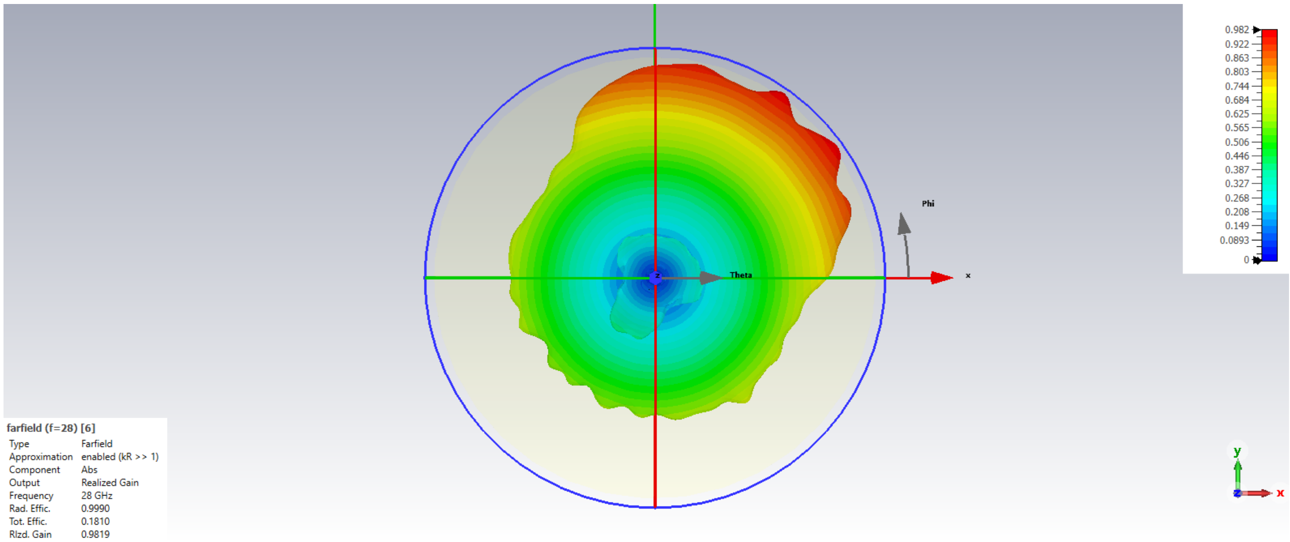

farfield (f=28) [6]

Type	Farfield
Approximation	enabled (kR >> 1)
Component	Abs
Output	Realized Gain
Frequency	28 GHz
Rad. Effic.	0.9990
Tot. Effic.	0.1810
Rlzd. Gain	0.9819

Figure 4.38: Sixth element fed: 3D top view.

6. **Seventh element fed**:

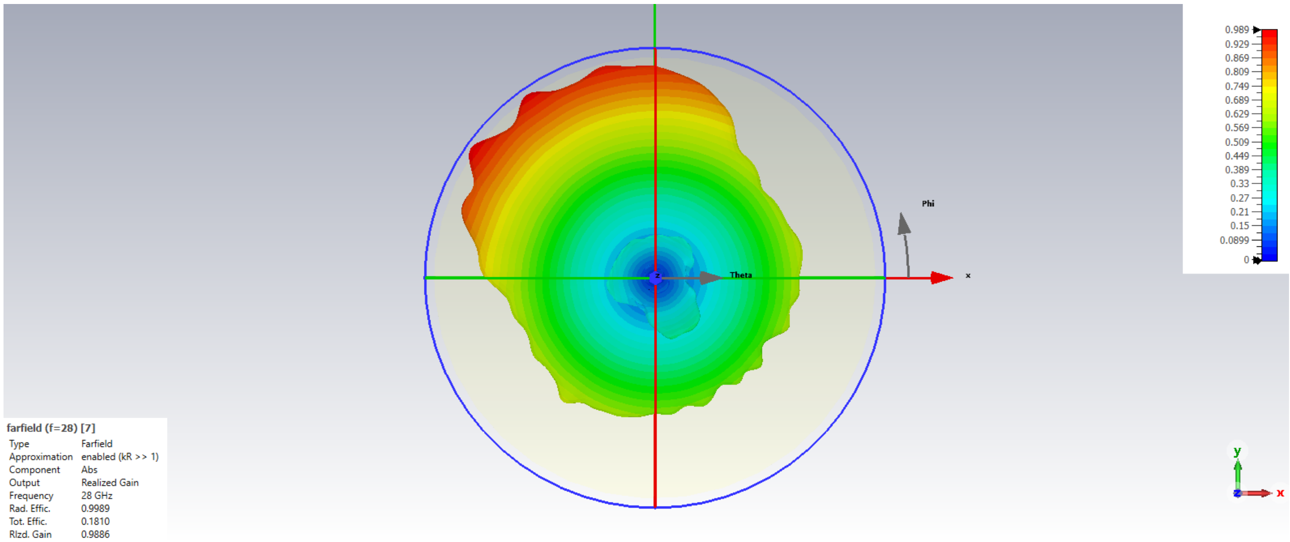

farfield (f=28) [7]

Type	Farfield
Approximation	enabled (kR >> 1)
Component	Abs
Output	Realized Gain
Frequency	28 GHz
Rad. Effic.	0.9989
Tot. Effic.	0.1810
Rlzd. Gain	0.9886

Figure 4.39: Seventh element fed: 3D top view.

4.6 Reactive loads synthesis

The objective of this section is to synthesize a physically implementable one-port load whose achievable reactance interval covers the set of required $\{X_{Li}\}$ for each passive element port. The adopted solution is based on the varactor diode MACOM MAVR-011020-1411, which has been used in previous works operating at comparable millimeter-wave frequencies [30, 31].

Diode model and CV reconstruction. The manufacturer gives a set of capacitance values (in pF) and corresponding bias voltages. In the circuit environment used (AWR), the varactor is modeled as a bias-dependent capacitor $C(V_{\text{bias}})$ in series with a small resistance R_s considiered for the diode losses.

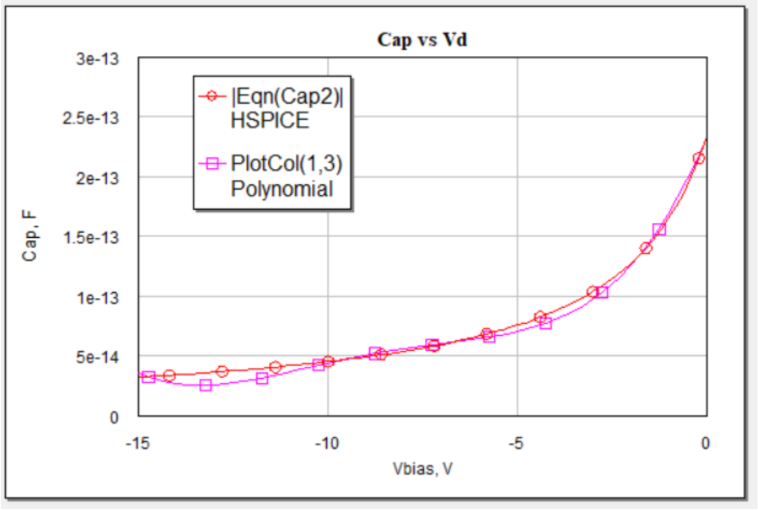

Figure 4.40: C–V curve from MACOM (datasheet reference).

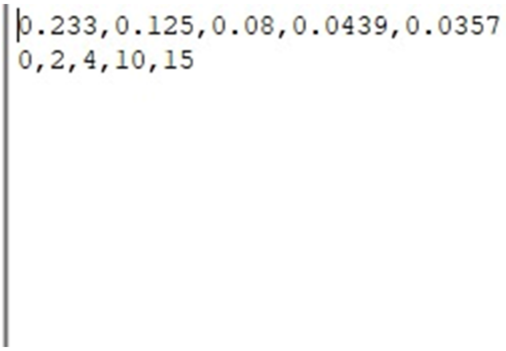

```
0.233,0.125,0.08,0.0439,0.0357
0,2,4,10,15
```

Figure 4.41: C–V samples file used in the circuit environment.

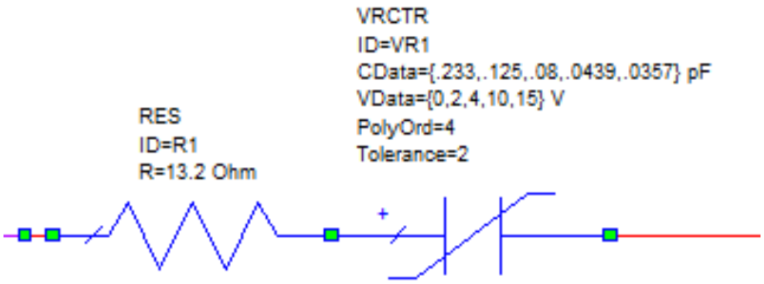

Figure 4.42: Varactor diode model provided by MACOM.

In order to reproduce the datasheet curve, the file in Fig.4.41 was imported into the schematic through a data file function. (Note that the physical bias is a reverse bias; in the simulator the values are set positive, but they should be interpreted with reversed polarity). A parametric sweep of V_{bias} confirms that the minimum and maximum capacitance values coincide with those reported in the datasheet, validating the CV curve reconstruction.

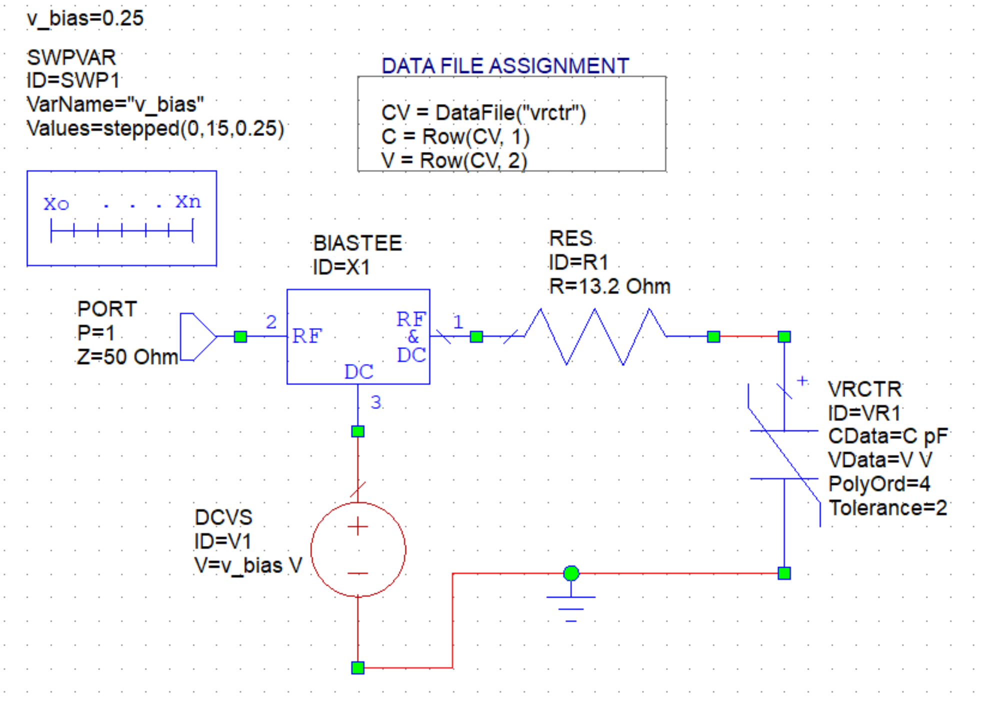

Figure 4.43: Biased varactor schematic.

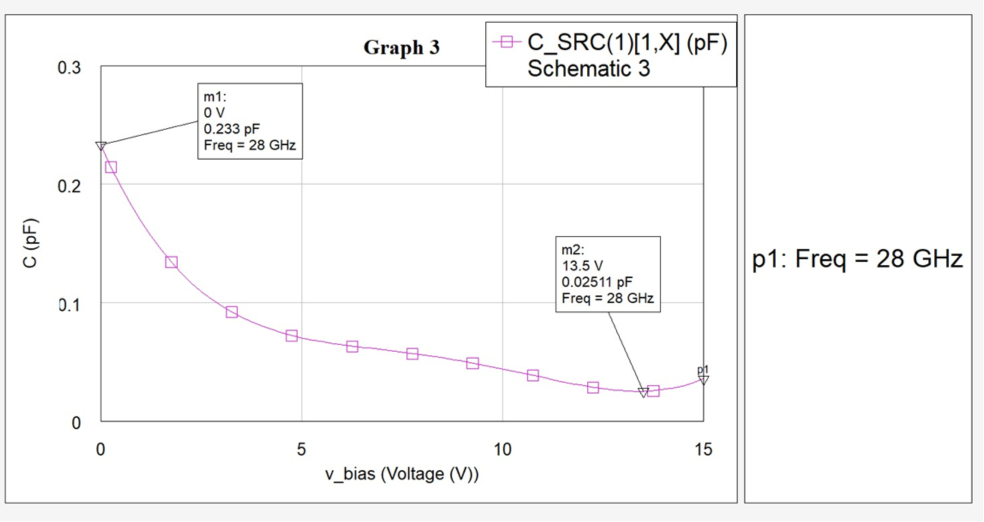

Figure 4.44: Simulated CV curve obtained from the imported samples.

Reactance range of the biased varactor. Once $C(V_{\mathrm{bias}})$ is available, an estimate of the tunable reactance is obtained by

$$X_C(V_{\mathrm{bias}}) = -\frac{1}{\omega_0\, C(V_{\mathrm{bias}})}, \qquad \omega_0 = 2\pi f_0. \tag{4.23}$$

This expression predicts a monotonic variation of X_C as the capacitance changes with bias. By plotting the reactance, it is possible to observe a behavior aligned with the simulated CV curve. Theoretically, a monotonically decreasing trend is expected; however, between 13,5V and 15V a positive slope is observed, coherently with the CV behavior in Fig.4.44.

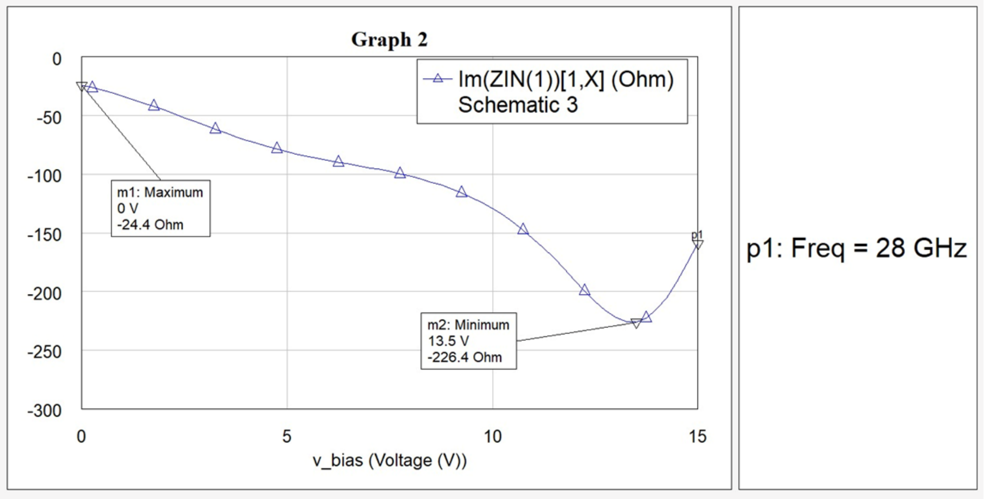

Figure 4.45: Simulated input reactance curve for the varactor model.

Inclusion of package parasitics. At millimeter-wave frequencies, package parasitics must be included due to their strong frequency dependence. The manufacturer provides a package model (Fig.4.47). The resulting input reactance remains bias dependent but shows regions with positive reactance (inductive behavior), this can be explained by a dominant series parasitic inductance L_s:

$$Z_{\mathrm{var}}(V_{\mathrm{bias}}) \approx R_s + j\omega_0 L_s + \frac{1}{j\omega_0 C(V_{\mathrm{bias}})}, \qquad X_{\mathrm{var}}(V_{\mathrm{bias}}) = \omega_0 L_s - \frac{1}{\omega_0 C(V_{\mathrm{bias}})}. \tag{4.24}$$

So, when $\omega_0 L_s > 1/(\omega_0 C)$ the net reactance becomes inductive.

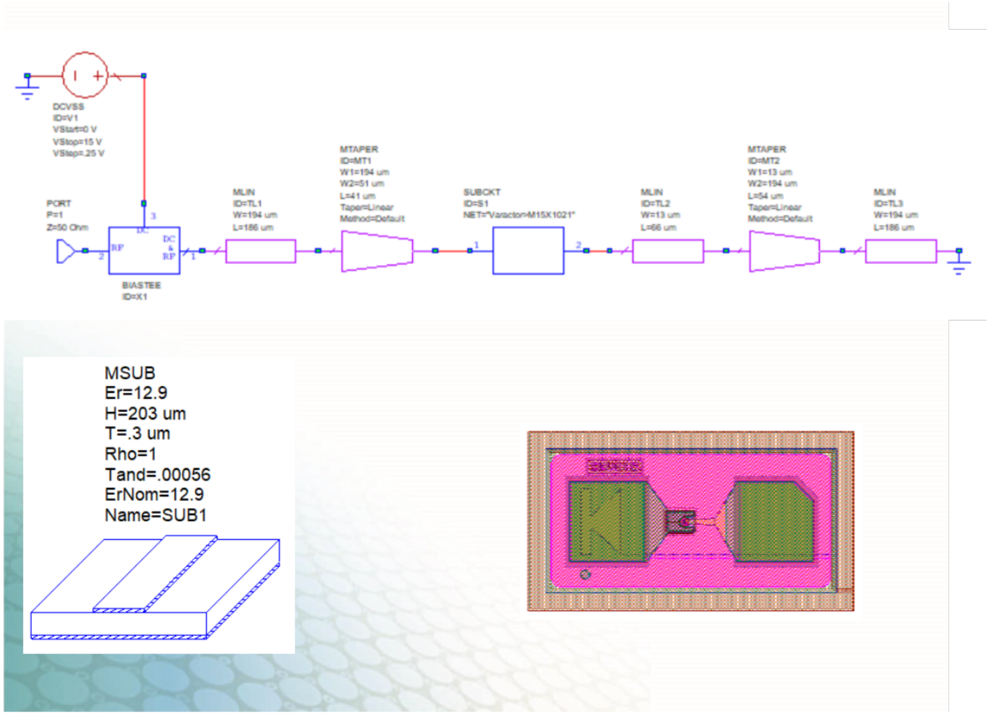

Figure 4.46: Package model provided by MACOM.

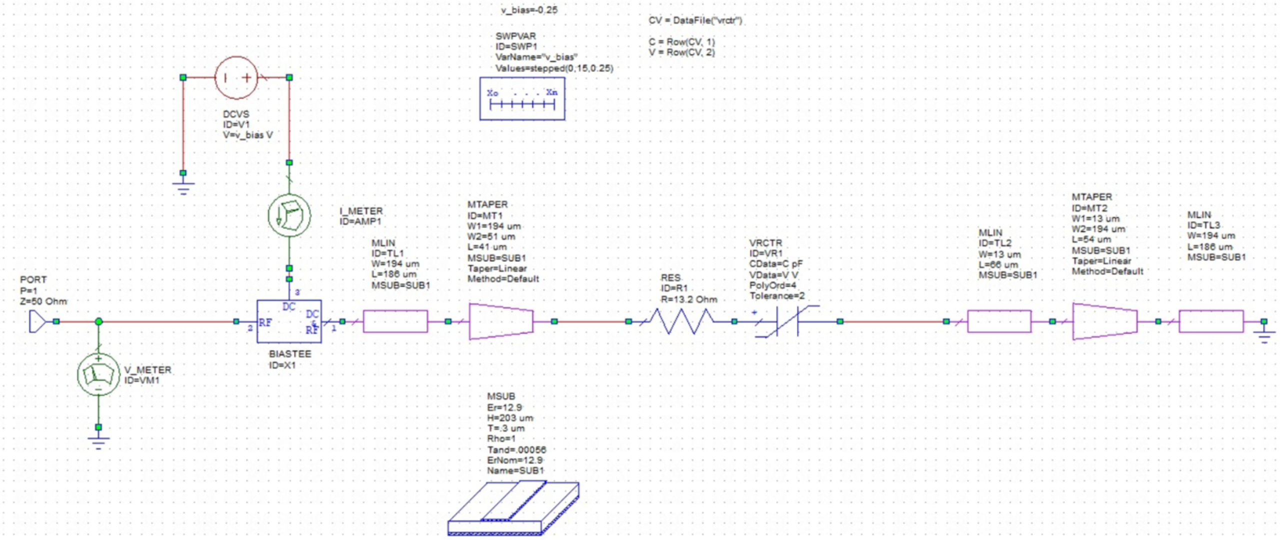

Figure 4.47: Biased varactor schematic including the package model.

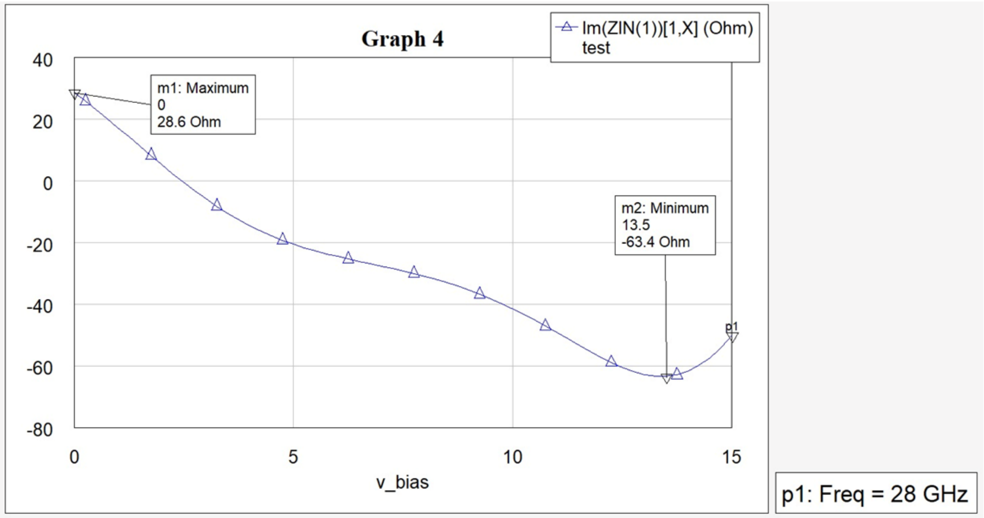

Figure 4.48: Input reactance of the varactor model including packaging.

The packaging provided by the manufacturer is not accurate enough for the working frequency of this project, an electromagnetic characterization should be done to better charcterize it. (See future works).

Analytical sizing of a varactor–stub tunable load. The reactance range to be achieved is taken from [1]:

$$X_{\text{in}} \in [-400,\ 180]\ \Omega. \tag{4.25}$$

The varactor capacitance range from the datasheet is

$$C \in [C_{\min}, C_{\max}] = [25\,\text{fF},\ 275\,\text{fF}], \qquad \omega_0 = 2\pi f_0, \quad f_0 = 28\,\text{GHz}. \tag{4.26}$$

To extend the reactance range to positive values, a shorted stub is introduced to provide an inductive contribution. In particular, A shorted stub of characteristic impedance Z_0 and electrical length βl has input impedance

$$Z_{\text{in,stub}}(l) = jZ_0 \tan(\beta l), \qquad \beta = \frac{2\pi}{\lambda_g}. \tag{4.27}$$

Therefore, its input admittance is

$$Y_{\text{stub}}(l) = \frac{1}{Z_{\text{in,stub}}(l)} = \frac{1}{jZ_0 \tan(\beta l)} = -j\frac{1}{Z_0 \tan(\beta l)}. \tag{4.28}$$

The varactor gives the capacitive admittance

$$Y_C(C) = j\omega_0 C. \tag{4.29}$$

Placing stub and varactor in parallel, the equivalent admittance is

$$Y_{\parallel}(C) = Y_C(C) + Y_{\text{stub}}(l) = j\omega_0 C + \frac{1}{jZ_0 \tan(\beta l)} = j\left(\omega_0 C - \frac{1}{Z_0 \tan(\beta l)}\right), \tag{4.30}$$

and the equivalent impedance at the parallel node is

$$Z_{\parallel}(C) = \frac{1}{Y_{\parallel}(C)}. \tag{4.31}$$

A quarterwave transformer is introduced to expand the range of possible values. With transformer characteristic impedance Z_t, the overall input impedance is

$$Z_{\text{in,tot}}(C) = \frac{Z_t^2}{Z_{\parallel}(C)}. \tag{4.32}$$

Since $Z_{\parallel}(C) = 1/Y_{\parallel}(C)$, (4.32) becomes

$$Z_{\text{in,tot}}(C) = Z_t^2 Y_{\parallel}(C) = jZ_t^2\left(\omega_0 C - \frac{1}{Z_0 \tan(\beta l)}\right). \tag{4.33}$$

Thus, the input reactance is

$$X_{\text{in,tot}}(C) = Z_t^2 \omega_0 C - \frac{Z_t^2}{Z_0 \tan(\beta l)}. \tag{4.34}$$

By defining the constants

$$A = Z_t^2 \omega_0, \qquad B = \frac{Z_t^2}{Z_0 \tan(\beta l)}, \tag{4.35}$$

so that

$$X_{\text{in,tot}}(C) = AC - B. \tag{4.36}$$

By imposing the required tuning range

$$X_{\text{in,tot}}(C_{\min}) = -400\ \Omega, \qquad X_{\text{in,tot}}(C_{\max}) = +180\ \Omega, \tag{4.37}$$

one obtains the system

$$\begin{cases} AC_{\text{min}} - B = -400, \\ AC_{\text{max}} - B = +180. \end{cases}$$

After subtracting one can obtain

$$A(C_{\text{max}} - C_{\text{min}}) = 580 \quad \Rightarrow \quad A = \frac{580}{C_{\text{max}} - C_{\text{min}}}, \tag{4.38}$$

and then

$$B = AC_{\text{min}} + 400. \tag{4.39}$$

By substituting the values, one gets

$$A \approx 2.32 \times 10^{15}, \qquad B \approx 458. \tag{4.40}$$

Therefore, the design equations become

$$\begin{cases} Z_t^2 \omega_0 = 2.32 \times 10^{15}, \\ \dfrac{Z_t^2}{Z_0 \tan(\beta l)} \approx 458. \end{cases}$$

From the first equation, the transformer's characteristic impedance is

$$Z_t = \sqrt{\frac{2.32 \times 10^{15}}{\omega_0}} = \sqrt{\frac{2.32 \times 10^{15}}{2\pi \cdot 28 \times 10^9}} \approx 115\ \Omega. \tag{4.41}$$

From the second equation, the reactance required from the shorted stub is

$$X_{\text{in,stub}} = Z_0 \tan(\beta l) \approx \frac{Z_t^2}{458} \approx 28.8\ \Omega. \tag{4.42}$$

Assuming a 50Ω microstrip line for the stub, the initial length estimate becomes

$$l = \frac{1}{\beta} \tan^{-1}\left(\frac{X_{\text{in,stub}}}{Z_0}\right) \approx 0.5\,\text{mm}. \tag{4.43}$$

The quarter wave transformer is dimensioned with $Z_t \approx 115\Omega$, width $W_t \approx$0.35 mm (calculated in AWR) and electrical length $\lambda_g/4$. The shorted stub is dimensioned with $Z_0 = 50\Omega$, width $W_s \approx$1.8 mm and length $l_s \approx$0.5 mm.

Since the stub would be wider than it is long, the form factor is not suitable. To avoid this problem, an open stub longer than $\lambda/4$ is adopted to still gurantee inductive behavior. The previous calculations are analytical, so the final design must be validated and tuned through circuit simulation including packaging parasitics.

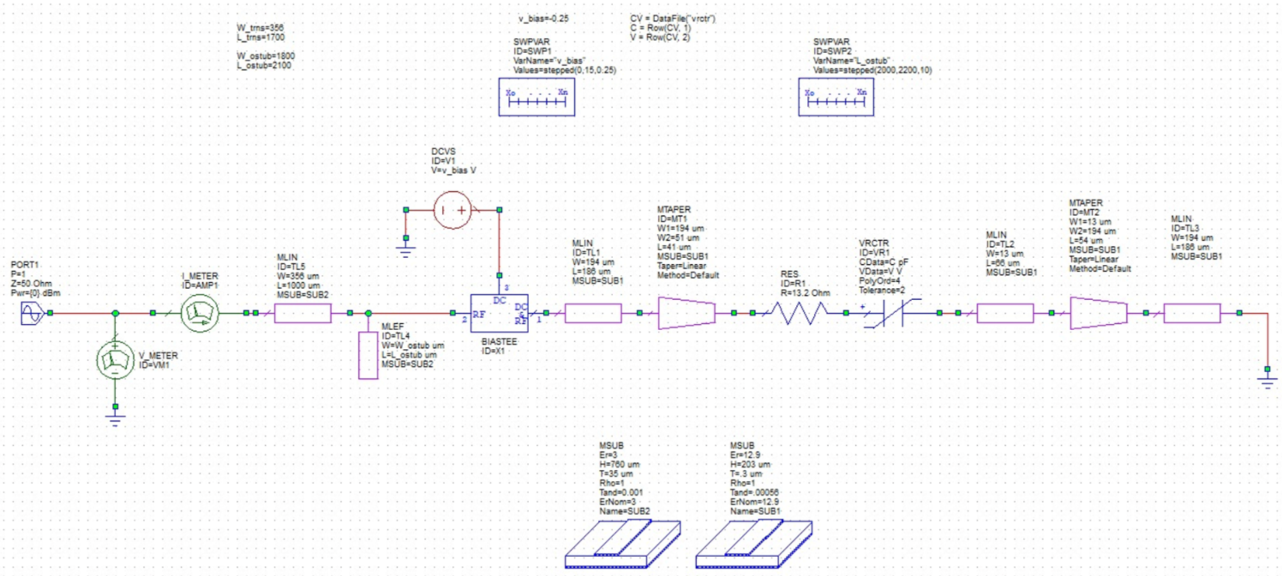

Figure 4.49: Final schematic including transformer, stub, and packaging.

The initial open-stub length is set to l=2 mm. By sweeping the open-stub length in the interval $l \in [2.0mm, 2.2mm]$, the input reactance of the complete circuit is obtained:

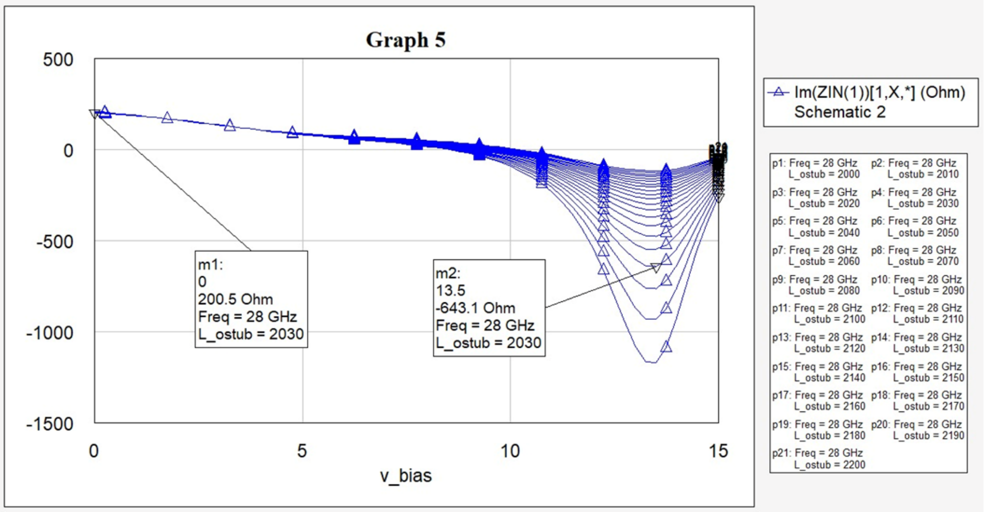

Figure 4.50: Input reactance of the final schematic (open-stub length sweep).

The sweep demonstrates that, after tuning, the proposed circuit is able to cover the target range and covers

$$X_{\text{in}} \in [-643,\ +200]\ \Omega \quad \text{at } 28\,\text{GHz}.$$

Moreover, by tuning the stub and transformer parameters, other reactance intervals can be synthesized if required.

4.7 Beam synthesis via optimized reactive loads

The final step shows the ability of the 127 element array to steer the far field in a precise direction by acting only on the reactive terminations of the passive ports tuning them to minimize the mismatch between a desired far field target and the reconstructed pattern.

4.7.1 Algorithm overview

The load optimization algorithm adopted was not part of this thesis work, by the way it has to be mentioned to understand the following results. Once the array layout is fixed (element topology, materials, and inter element spacing), a single full-wave EM simulation is performed by exciting each port with a unitary current source. This provides both the near-field mutual coupling among the elements and the embedded far-field contribution associated with each port excitation.

The full-wave results are then embedded into a circuit model, which is used to predict the far field pattern generated by the array for arbitrary excitations and port terminations. So, beam synthesis is done as an optimization over the port loads: for any desired configuration (including single beam steering or simultaneous multi beam operation with single or multi port excitations), the reactive terminations are iteratively tuned to minimize the mismatch between the wanted and the reconstructed far field.

The main advantage of this approach is that the full wave simulation is required only once, and it already includes coupling and embedded element behavior. So, different beams can be evaluated and optimized by playing on the circuit model load variables, instead of repeated full-wave runs unless the array geometry is modified (and so the mutual coupling and far-fields).

4.7.2 Dual beam target

A first test considers a dual beam scenario with two maxima at

$$(\theta_0, \phi_0) = (70^\circ, 30^\circ), \qquad (\theta_0, \phi_0) = (70^\circ, 180^\circ).$$

and $HPBW = 20°$ ($\theta_0 = 70$ in each of the following results, since the radiation diagram was tilted with respect to the ground plane, as seen in Chapter 4). The 3D comparison between desired and reconstructed patterns highlights that the optimization is able to reproduce the two lobes. In particular, the reconstructed maxima are approximately:

$$\max |\mathbf{E}_\theta| \simeq 0.894 \text{ at } (\theta, \phi) \approx (70°, 31°), \qquad \max |\mathbf{E}_\theta| \simeq 0.872 \text{ at } (\theta, \phi) \approx (69°, 180°).$$

The corresponding polar cuts on $\theta = 70°$ confirm the previous data.

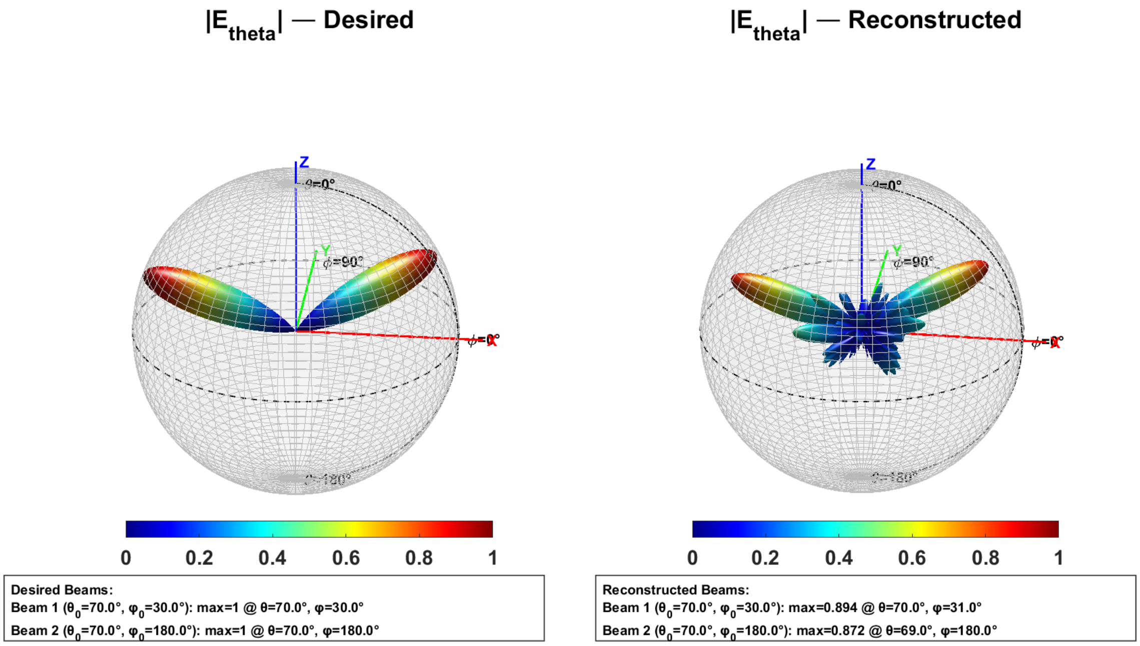

Figure 4.51: Dual-beam case: $|\mathbf{E}_\theta|$ in 3D, desired vs reconstructed.

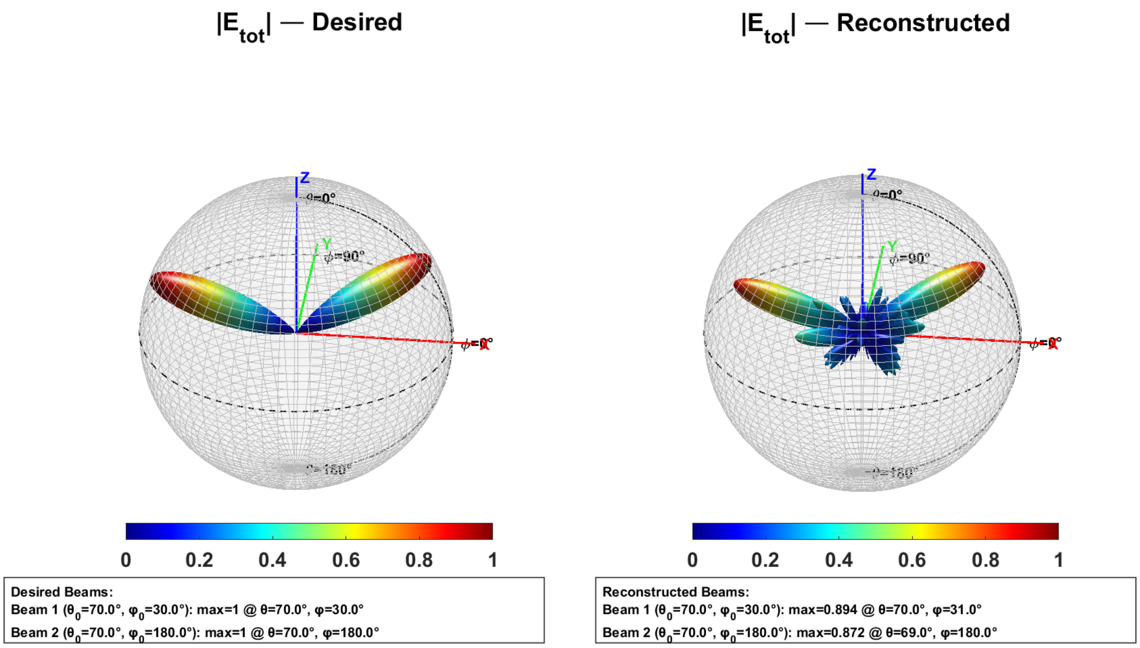

Figure 4.52: Dual-beam case: $|\mathbf{E}_{\text{tot}}|$ in 3D, desired vs reconstructed.

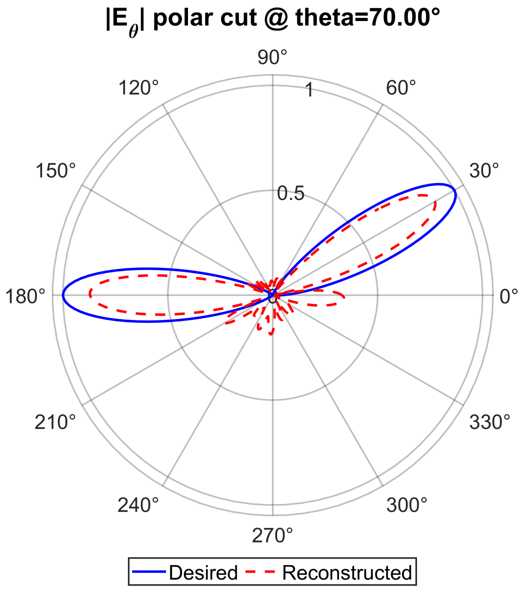

Figure 4.53: Dual-beam case: polar cut of $|\mathbf{E}_\theta|$ at $\theta = 70°$, desired vs reconstructed.

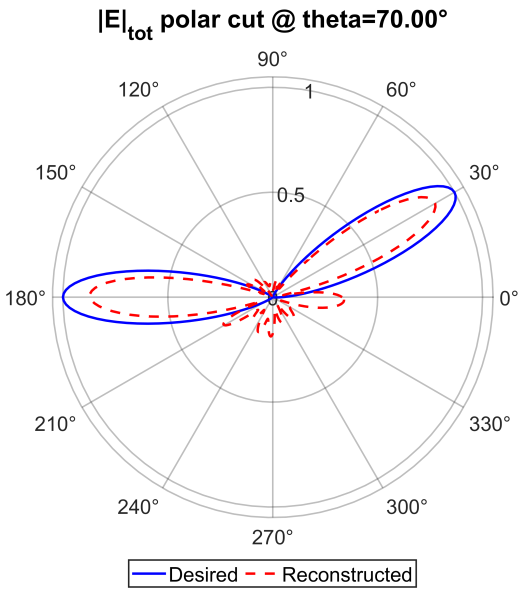

Figure 4.54: Dual-beam case: polar cut of $|\mathbf{E}_{\text{tot}}|$ at $\theta = 70°$, desired vs reconstructed.

In this case, as in the single-beam one, the electric field is linearly polarized along θ and so the total field $|E_{tot}|$ coincides with the field along theta $|E_\theta|$

4.7.3 Single beam targets

The optimization was then repeated for two single-beam targets, keeping the same elevation angle and steering the azimuth direction. As for the multi-beam case: $HPBW = 20°$

Beam at $(\theta_0, \phi_0) = (70°, 30°)$

For the beam steered at $\phi_0 = 30°$, the reconstructed maximum is

$$\max|\mathbf{E}_\theta| \simeq 0.956 \text{ at } (\theta, \phi) \approx (71°, 30°),$$

corresponding to a peak reduction of $20\log_{10}(0.956) \approx -0.39$ dB and a pointing error of about 1° in elevation with respect to the ideal case. The polar cut at $\theta = 70°$ shows clearly how the beam is reconstructed well.

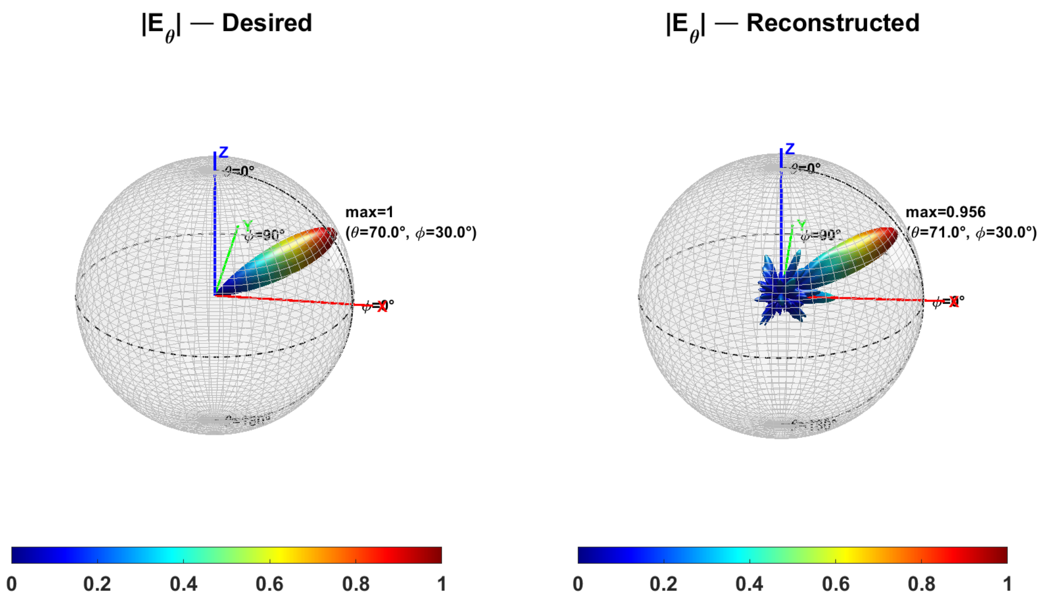

|E$_\theta$| — Desired

|E$_\theta$| — Reconstructed

Figure 4.55: Single-beam case ($\phi_0 = 30°$): $|\mathbf{E}_\theta|$ in 3D, desired vs reconstructed.

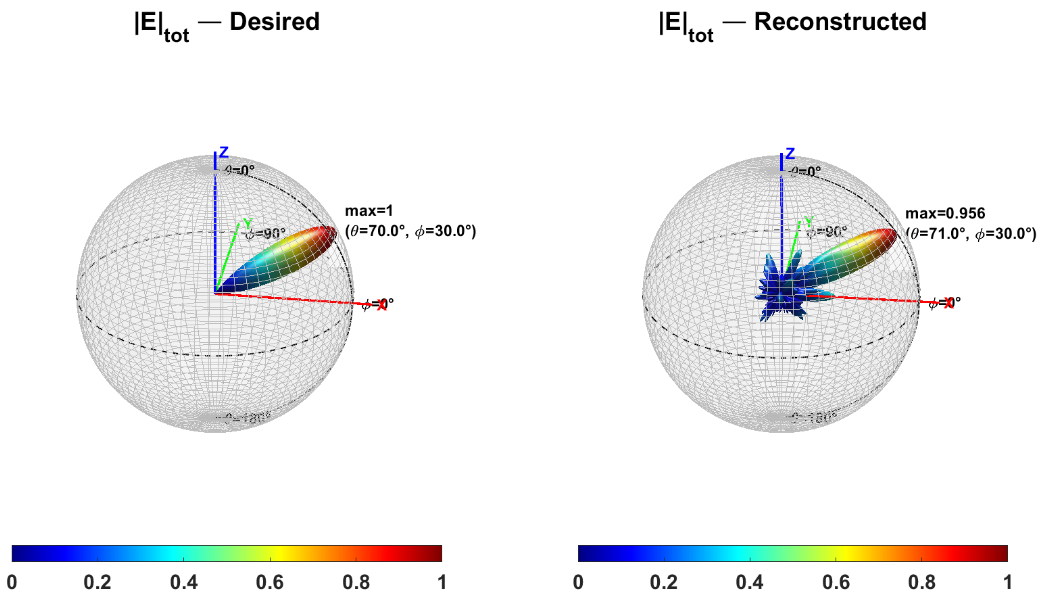

|E|$_{\text{tot}}$ — Desired

|E|$_{\text{tot}}$ — Reconstructed

Figure 4.56: Single-beam case ($\phi_0 = 30°$): $|\mathbf{E}_{\text{tot}}|$ in 3D, desired vs reconstructed.

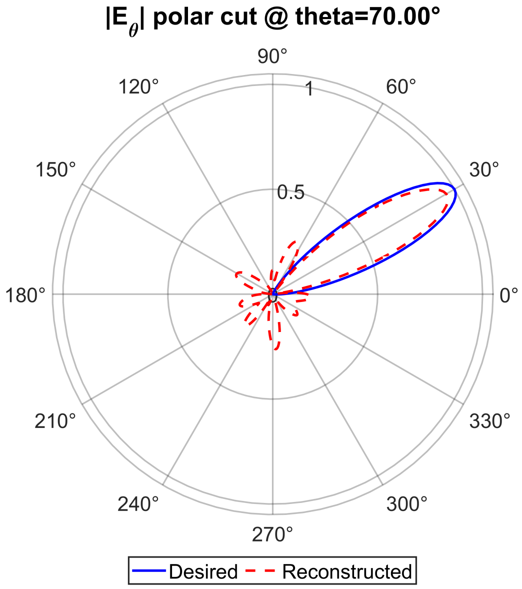

Figure 4.57: Single-beam case ($\phi_0 = 30°$): polar cut of $|\mathbf{E}_\theta|$ at $\theta = 70°$, desired vs reconstructed.

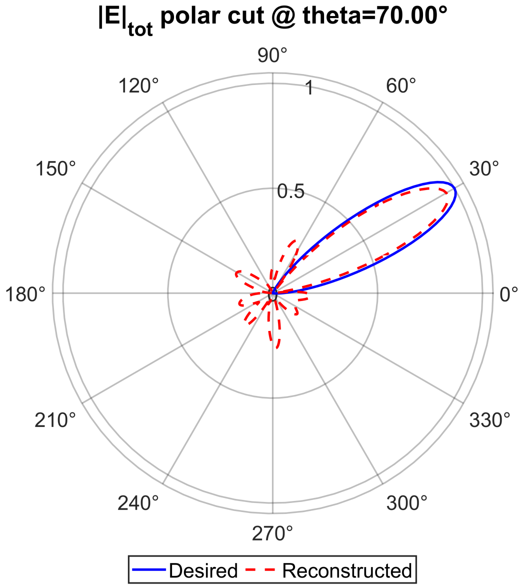

Figure 4.58: Single-beam case ($\phi_0 = 30°$): polar cut of $|\mathbf{E}_{\text{tot}}|$ at $\theta = 70°$, desired vs reconstructed.

Beam at $(\theta_0, \phi_0) = (70^\circ, 180^\circ)$

For the beam steered toward $\phi_0 = 180^\circ$, the reconstructed maximum is

$$\max|\mathbf{E}_\theta| \simeq 0.966 \text{ at } (\theta, \phi) \approx (71^\circ, 180^\circ),$$

corresponding to about -0.30 dB peak reduction and a similar $\approx 1^\circ$ elevation shift. Also in this case, the agreement is strongest on the main lobe, with residual discrepancies mainly in sidelobe regions.

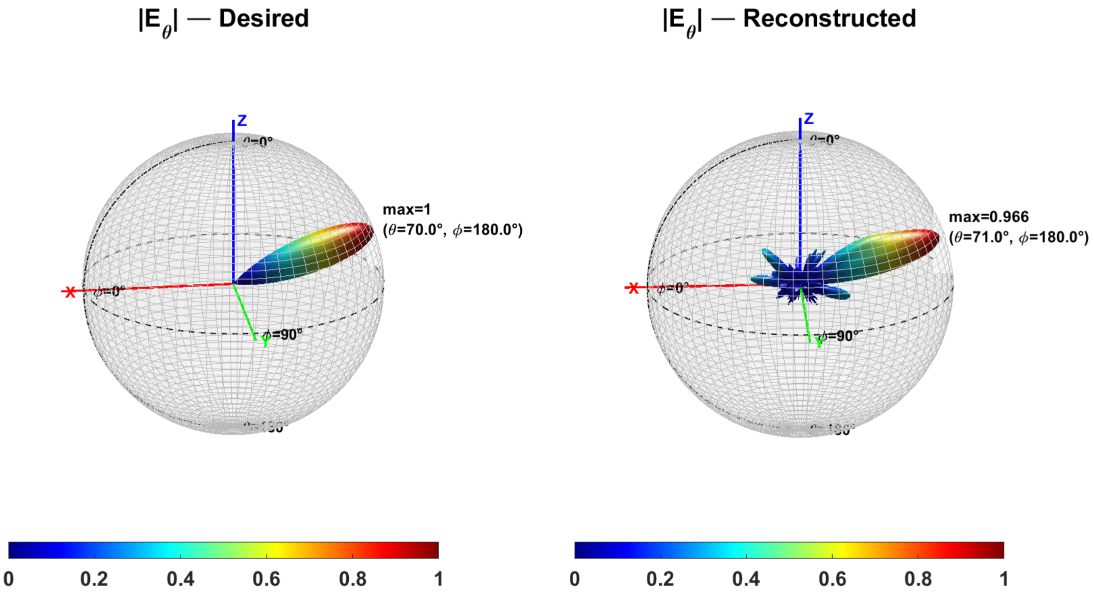

Figure 4.59: Single-beam case ($\phi_0 = 180^\circ$): $|\mathbf{E}_\theta|$ in 3D, desired vs reconstructed.

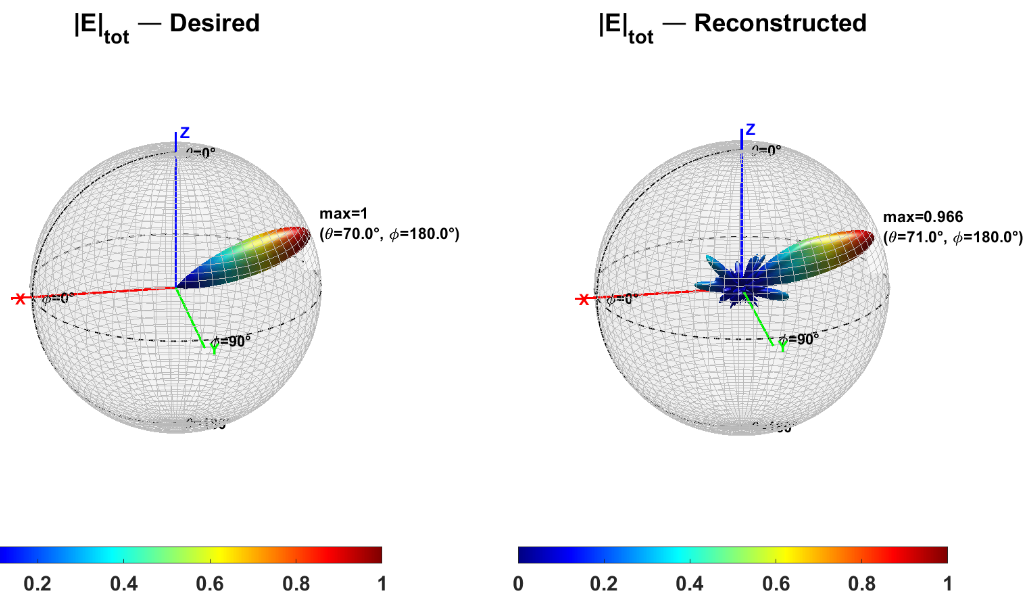
|E|$_{tot}$ — Desired

|E|$_{tot}$ — Reconstructed

Figure 4.60: Single-beam case ($\phi_0 = 180°$): $|\mathbf{E}_{\text{tot}}|$ in 3D, desired vs reconstructed.

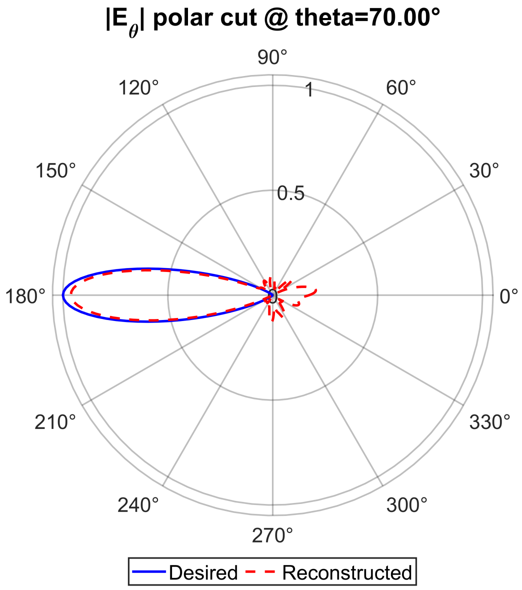
|E$_\theta$| polar cut @ theta=70.00°

Figure 4.61: Single-beam case ($\phi_0 = 180°$): polar cut of $|\mathbf{E}_\theta|$ at $\theta = 70°$, desired vs reconstructed.

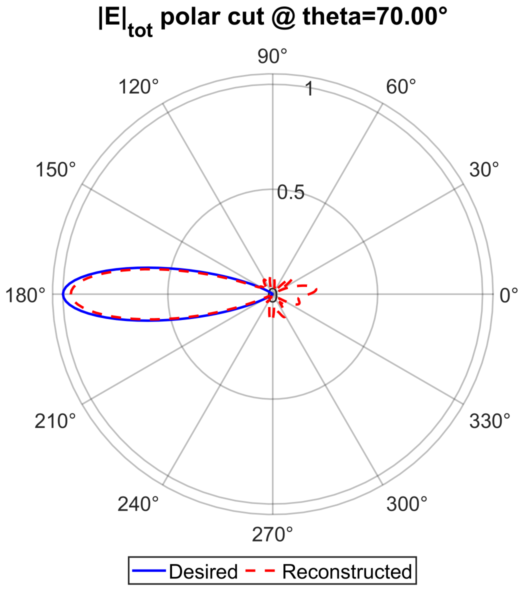

Figure 4.62: Single-beam case ($\phi_0 = 180°$): polar cut of $|\mathbf{E}_{\text{tot}}|$ at $\theta = 70°$, desired vs reconstructed.

4.7.4 Optimized reactive load distributions

For completeness, Fig. 4.63, Fig. 4.64 and Fig. 4.65 show the optimized reactive loads for the two single beam and the double beam runs. The obtained values span approximately the interval $[-400, +200]$ Ω.

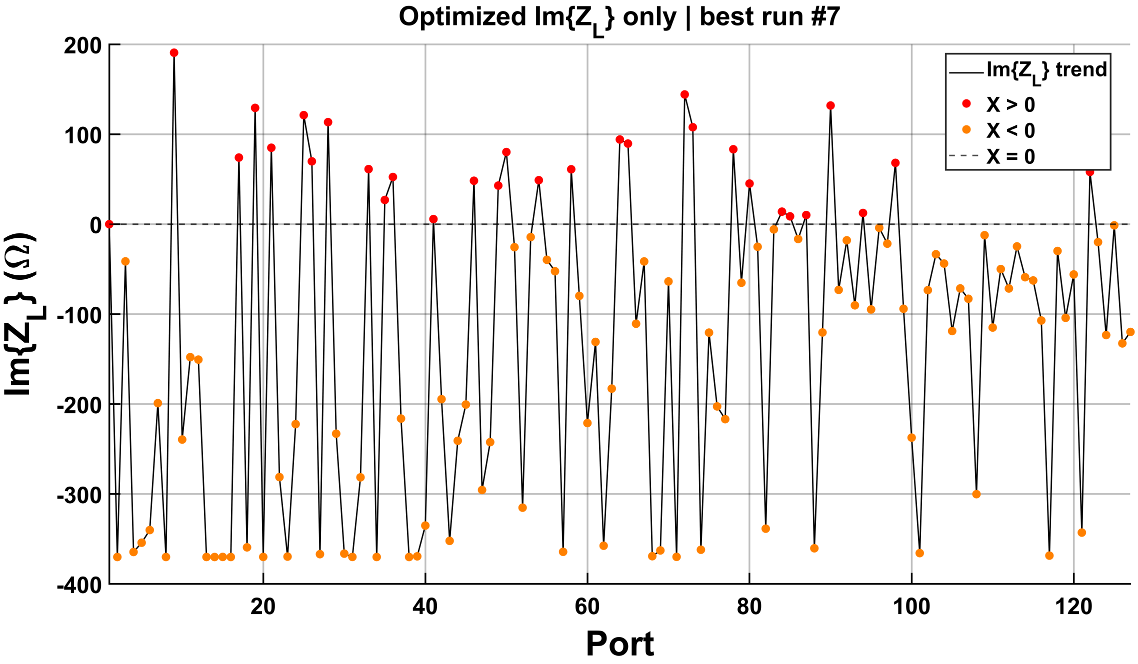

Figure 4.63: Single-beam case ($\phi_0 = 30°$): optimized reactive loads $\Im\{Z_L\}$ across the ports.

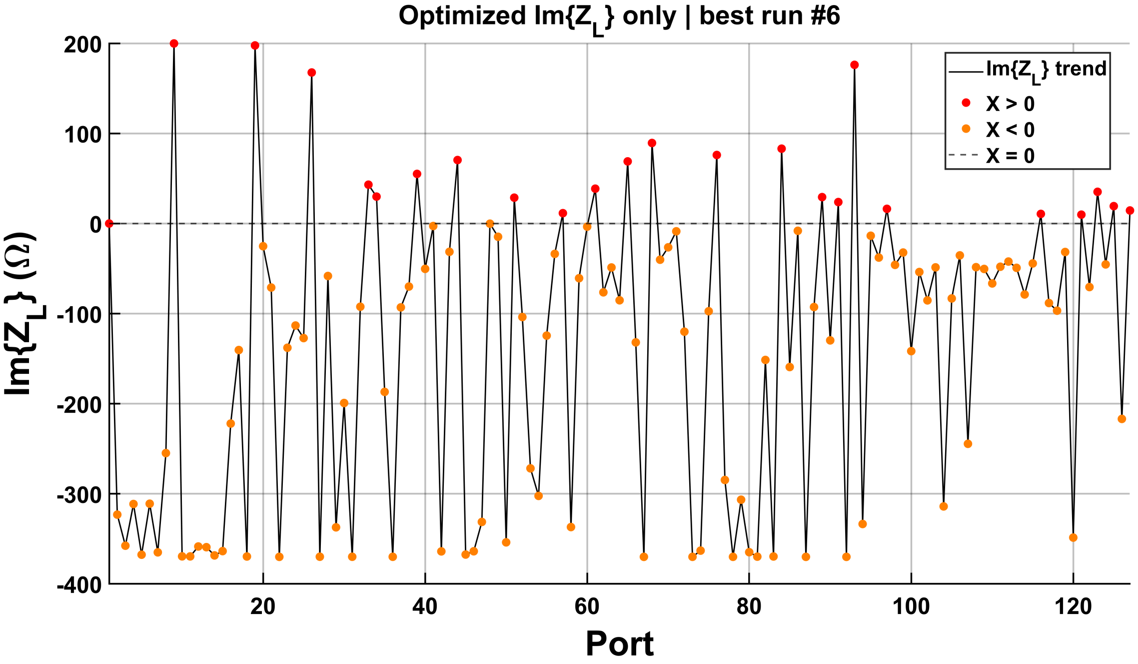

Figure 4.64: Single-beam case ($\phi_0 = 180°$): optimized reactive loads $\Im\{Z_L\}$ across the ports.

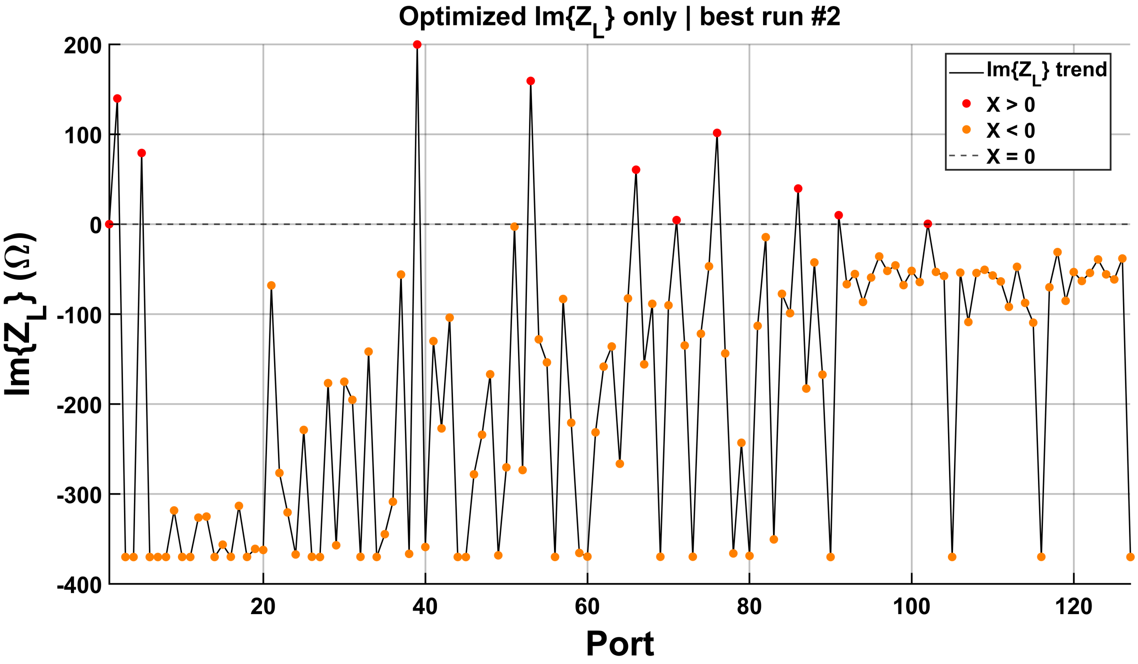

Figure 4.65: Multi-beam case: optimized reactive loads $\Im\{Z_L\}$ across the ports.

Chapter 5

Conclusions and Future Works

5.1 Conclusions

This thesis presented the practical implementation of a 127 element DSA operating at 28 GHz, starting from the ideal reference scenario (PEC dipoles in vacuum) and implementing it as an array of monopoles embedded in dielectric substrate.

A first implementation was done in planar technology (Chapter 3), since it could provide a compact layout with easily integrable feeding lines. The single printed monopole was tuned at 28 GHz to obtain the target complex input impedance ($Z_{\text{in,ref}} = 73+j42\ \Omega$), and it showed the expected far field behavior of a monopole. However, when moving to a first array prototypes (1 central element and the first ring of 6 elements around), the performance was worst. In particular, the finite ground plane introduced strong parasitic currents and edge re radiation. In order to understand if the pattern degradation was due to the coupling between the elements or just to the ground plane, a decoupling network based on slotting the ground plane was tested and showed an improvement in isolation (reduced $|S_{ij}|$) and mitigated leakage currents. However the radiation pattern was still too much distorted with respect to the ideal one and so the main cause of that was attributed to the finite ground plane.

To overcome these limitations, the final architecture (Chapter 4) was thought as a circular ground plane with hexahedron monopoles realized as pseudo via-holes in a dielectric overlay, to ease the realization of such miniaturized radiating elements at 28 GHz. The circular ground geometry was selected to suppress current concentration in the corners and so to restore azimuthal omnidirectionality, while a large ground plane's radius was chosen to reduce elevation ripples and beam tilting associated with finite ground's edge diffraction. The embedded monopole configuration was then tuned to resonate at 28 GHz in the presence of a dielectric having electrical permittivity $\varepsilon_r = 2$. Then, the full 127 element array was finally implemented as a central element surrounded by six concentric rings, with inter-ring spacing set to approximately $\lambda_0/4$. An important experimental result shows that the dielectric overlay increases the gain more than being used just as a mechanical support for the monopoles.

A varactor based one port load was designed by combining: a biased varactor diode model, a transmission line stub to extend the achievable reactance to positive values, and an impedance transformer to scale the effective tuning range. The final topology demonstrated, after tuning, a reactance coverage compatible with the ranges required by the reconfigurable array.

Finally, the thesis presented the final results of far-field beam synthesis thanks to optimized reactive loads obtained through an optimization algorithm (here only summarized, as it was developed by a collegue). The results show that the reconstructed patterns reproduce the desired main beam direction with an accuracy of 90% for the gain.

5.2 Future work

The activity carried out in this thesis highlighted many critical aspects which will have to be better analyzed in future developments

Realistic feeding network implementation Discrete ports were intentionally used to separate the radiation properties of the array from parasitic contributions given by a feeding topology. By the way, this choice does not consider the losses, and spurious radiation generated by a realistic feeding network. Future work will focus on the design of a physically realizable feeding network and on its integration in the model.

Dielectric overlay study The final configuration embeds the monopoles in a dielectric overlay to obtain a compact architecture, realizing monopoles as via holes. However, a dielectric volume at 28GHz may support surface wave or modes proper of the dielectric structure altering the coupling and the radiation pattern. In the present work the overlay height was selected to obtain a radiation pattern as clean as possible, to obtain this its height is way grater than the monopole's height ($H_{sub} \approx 3\lambda_g \quad vs \quad H_{monopole} \approx \lambda_g/4$)

with λ_g being the lambda in the substrate. Future work will analyze this phenomenon through eigenmode analyses, in order to reduce the substrate height as much as possible to be conformal with the substrate's standard height, still maintaining a clean radiation pattern.

Accuracy of varactor modeling at mm wave frequencies. The reconfigurability of the DSA is given by the synthesis of reactive loads able to cover the required reactance interval. At 28GHz, the varactor behavior is strongly affected by package parasitics. The provided packaging model gives a starting point for analytical sizing, but it is modelized in a circuit simulator using transmission lines and an ideal bias tee. Future work will include an electromagnetic simulation of the varactor packaging to extract an accurate frequency dependent model and the design of a realistic bias-tee using bypass capacitors. The EM extracted model will then be simulated with the tuning network (stub and transformer) to verify that the synthesized reactance interval remains compatible with the array beam synthesis.

Bibliography

[1] R. Harrington, “Reactively controlled directive arrays,” *IEEE Transactions on Antennas and Propagation*, vol. 26, no. 3, pp. 390–395, 1978.

[2] R. Milne, “A small adaptive array antenna for mobile communications,” in *1985 Antennas and Propagation Society International Symposium*, vol. 23, pp. 797–800, 1985.

[3] C. Sun, A. Hirata, T. Ohira, and N. Karmakar, “Fast beamforming of electronically steerable parasitic array radiator antennas: theory and experiment,” *IEEE Transactions on Antennas and Propagation*, vol. 52, no. 7, pp. 1819–1832, 2004.

[4] J. Shu, G. Xu, H. Peng, and J. Mao, “An electrically steerable parasitic array radiator in package based on liquid crystal,” *IEEE Antennas and Wireless Propagation Letters*, vol. 18, no. 11, pp. 2365–2369, 2019.

[5] D. v. B. M. Trindade, C. Müller, M. C. F. De Castro, and F. C. C. De Castro, “Metamaterials applied to espar antenna for mutual coupling reduction,” *IEEE Antennas and Wireless Propagation Letters*, vol. 14, pp. 430–433, 2015.

[6] M. R. Nikkhah, P. Loghmannia, J. Rashed-Mohassel, and A. A. Kishk, “Theory of espar design with their implementation in large arrays,” *IEEE Transactions on Antennas and Propagation*, vol. 62, no. 6, pp. 3359–3364, 2014.

[7] M. Rzymowski, K. Nyka, and L. Kulas, “Direction of arrival estimation based on received signal strength using two-row electronically steerable parasitic array radiator antenna,” *Sensors*, vol. 22, no. 5, 2022.

[8] M. Ohira, A. Miura, M. Taromaru, and M. Ueba, “Efficient gain optimization techniques for azimuth beam/null steering of inverted-f multiport parasitic ar-

ray radiator (mupar) antenna," *IEEE Transactions on Antennas and Propagation*, vol. 60, no. 3, pp. 1352–1361, 2012.

[9] S. Zhang, I. Syrytsin, and G. F. Pedersen, "Compact beam-steerable antenna array with two passive parasitic elements for 5g mobile terminals at 28 ghz," *IEEE Transactions on Antennas and Propagation*, vol. 66, no. 10, pp. 5193–5203, 2018.

[10] J. Lu, D. Ireland, and R. Schlub, "Dielectric embedded espar (de-espar) antenna array for wireless communications," *IEEE Transactions on Antennas and Propagation*, vol. 53, no. 8, pp. 2437–2443, 2005.

[11] M. Czelen, M. Rzymowski, K. Nyka, and L. Kulas, "Influence of dielectric overlay permittivity on size and performance of miniaturized espar antenna," in *2020 23rd International Microwave and Radar Conference (MIKON)*, pp. 289–292, 2020.

[12] M. Czelen, M. Rzymowski, K. Nyka, and L. Kulas, "Influence of dielectric overlay dimensions on performance of miniaturized espar antenna," in *2020 IEEE International Symposium on Antennas and Propagation and North American Radio Science Meeting*, pp. 387–388, 2020.

[13] D. Dardari, "Over-the-air multifunctional wideband electromagnetic signal processing using dynamic scattering arrays," *IEEE Transactions on Wireless Communications*, vol. 25, pp. 5016–5028, 2026.

[14] D. Dardari, "Dynamic scattering arrays for simultaneous electromagnetic processing and radiation in holographic mimo systems," *ArXiv*, vol. abs/2405.16174, 2024.

[15] M. Inomata, W. Yamada, N. Kuno, M. Sasaki, M. Nakamura, K. Kitao, T. Tomie, and S. Suyama, "Path-loss characteristics and modeling for 2-300-ghz bands in urban microcell environment," in *2023 17th European Conference on Antennas and Propagation (EuCAP)*, pp. 1–5, 2023.

[16] M. A. Soliman, K. H. Moussa, H. Tolba, and A. R. Sebak, "Pushing the limits of mimo beamforming: Innovations, challenges, and the path to 6g," in *2025 International Telecommunications Conference (ITC-Egypt)*, pp. 941–946, 2025.

[17] S. Payami, K. Nikitopoulos, M. Khalily, and R. Tafazolli, "A signal processing framework for agile rf beamforming: From rf-chain-free to hybrid beamformers," *IEEE Transactions on Communications*, vol. 69, no. 6, pp. 4038–4053, 2021.

[18] R. Harrington and J. Mautz, "Theory of characteristic modes for conducting bodies," *IEEE Transactions on Antennas and Propagation*, vol. 19, no. 5, pp. 622–628, 1971.

[19] J. R. M. Roger F. Harrington, *Modal analysis of loaded N-port scatterers.* Syracuse, New York: Department of Electrical and Computer Engineering, Syracuse University, 1972.

[20] M. ˇCapek, "Theory of characteristic modes," May 1, 2021.

[21] R. F. Harrington, *Optimization*, pp. 189–212. 1993.

[22] M. T. Ivrlač and J. A. Nossek, "Toward a circuit theory of communication," *IEEE Transactions on Circuits and Systems I: Regular Papers*, vol. 57, no. 7, pp. 1663–1683, 2010.

[23] C. A. Balanis, *Antenna theory analysis and design*, vol. 2. John Wiley & Sons google schola, 2005.

[24] Z. Živković, D. Senić, C. Bodendorf, J. Skrzypczynski, and A. Šarolić, "Radiation pattern and impedance of a quarter wavelength monopole antenna above a finite ground plane," in *SoftCOM 2012, 20th International Conference on Software, Telecommunications and Computer Networks*, pp. 1–5, 2012.

[25] M. Daginnus, R. Kronberger, and A. Stephan, "Ground plane effects on the performance of sdars antennas," in *IEEE Antennas and Propagation Society International Symposium (IEEE Cat. No.02CH37313)*, vol. 4, pp. 748–751 vol.4, 2002.

[26] H.-F. Chen, M.-Y. Lin, and K.-H. Lin, "A v-shape edge-groove design for a finite ground plane to reduce pattern ripples of a monopole," *IEEE Antennas and Wireless Propagation Letters*, vol. 7, pp. 561–564, 2008.

[27] J. Janapsatya and M. Bialkowski, "Implementation of a structured ground plane to improve radiation pattern of a circular array of monopoles," in *IEEE Antennas and Propagation Society International Symposium. Digest. Held in conjunction with: USNC/CNC/URSI North American Radio Sci. Meeting (Cat. No.03CH37450)*, vol. 1, pp. 864–867 vol.1, 2003.

[28] R. Schlub and D. Thiel, "Switched parasitic antenna on a finite ground plane with conductive sleeve," *IEEE Transactions on Antennas and Propagation*, vol. 52, no. 5, pp. 1343–1347, 2004.

[29] R. Wang and V. Liepa, "Reduction of the edge diffraction of a circular ground plane by using resistive edge loading," in *1985 Antennas and Propagation Society International Symposium*, vol. 23, pp. 769–771, 1985.

[30] Q. Chen, J. Ala-Laurinaho, A. Khripkov, J. Ilvonen, R. M. Moreno, and V. Viikari, "Varactor-based frequency-reconfigurable dual-polarized mm-wave antenna array for mobile devices," *IEEE Transactions on Antennas and Propagation*, vol. 71, no. 8, pp. 6628–6638, 2023.

[31] H. A. Kayani and C. Craeye, "A high directivity beam-steering parasitic antenna array," in *2019 49th European Microwave Conference (EuMC)*, pp. 29–32, 2019.